

國立交通大學

電子物理研究所

博士論文

二六族化合物半導體及奈米結構的
光學性質

Optical Properties of II-VI Compound
Semiconductors and Nanocrystals



研究生：林彥丞

指導教授：周武清 教授

中華民國九十八年一月

二六族化合物半導體及奈米結構的光學性質

Optical Properties of II-VI Compound

Semiconductors and Nanocrystals

研究生：林彥丞

Student：Yan-Cheng Lin

指導教授：周武清 教授

Advisor：Prof. Wu-Ching Chou

國立交通大學

電子物理研究所



A Dissertation

Submitted to Institute of Electrophysics

College of Science

National Chiao Tung University

in Partial Fulfillment of the Requirements

for the Degree of

Doctor of Philosophy

in

Electrophysics

January 2009

Hsinchu, Taiwan, Republic of China

中華民國九十八年一月

二六族化合物半導體及奈米結構的光學性質

研究生：林彥丞

指導教授：周武清 教授

國立交通大學電子物理研究所

中文摘要

本論文的第一部份使用鑽石高壓及半導體光頻譜技術，探討二六族化合物硒化鎘鋅(鎘含量佔 0 至 32 莫耳百分比)和碲化錳鋅(錳含量佔 0 至 26 莫耳百分比)半導體薄膜的光學聲子模態和晶體結構特性。藉由觀察拉曼散射光譜可以確定硒化鎘鋅以及碲化錳鋅的光學聲子模都屬於中間態。我們以二次多項式去擬合縱向光學聲子頻率隨壓力變化的關係，求得格留乃森 (Grüneisen) 參數。在鎘濃度較高的硒化鎘鋅樣品中發現由外加壓力引起的共振拉曼散射增強效應，這個共振效應也被用來研究在常溫常壓時拉曼訊號相當微弱之碲化錳鋅半導體。高壓拉曼實驗結果顯示，半導體轉變為金屬相的開始壓力會隨著鎘和錳元素的參雜濃度增加而下降。當鎘(錳)濃度從 0 增加到 32 莫耳百分比(0 增加到 26 莫耳百分比)時，相轉變壓力從 13.6 降至 9.4 (15.7 至 10.3) GPa。此外，實驗結果顯示在常壓時，錳離子的參雜會增加碲化鋅半導體的離子性質，然而外加壓力卻會降低碲化錳鋅的離子性。

利用拉曼光頻譜來觀察以氯摻雜之 n 型硒化鋅薄膜半導體 (電子濃度範圍從 $8.2 \times 10^{15} \text{ cm}^{-3}$ 到 $1.8 \times 10^{18} \text{ cm}^{-3}$) 的聲子振動、電子濃度以及晶體結構的特性。實驗發現，氯摻雜之 n 型硒化鋅半導體的拉曼光譜會受到縱向光學聲子以及自由電子耦合效應的影響。因此藉由拉曼散射效率方程式以及介電方程式來擬合譜線，可以求得樣品的電子濃度和載子遷移率。實驗發現半導體轉變為金屬相的開始壓力會隨著電子濃度的增加而下降，這個現象指出樣品參雜電子也會造成晶體的不穩定。此外，我們發現外加壓力會使

得縱向光學聲子和自由電子的耦合效率變低，可能是因為加壓造成另一個深層施子能態的產生，使得樣品的電子濃度降低所造成。

本論文第二部份我們發現由Kohlrausch提出的指數延伸定律與等電性碲硒化鋅半導體螢光的衰減頻譜有極高的關聯性。當碲原子的濃度增加時，延伸參數 (β) 會先降低而後增加，這個結果可以用跳躍遷移 (hopping-transport) 以及能量轉移的模型來解釋。當等電性碲原子捕捉態 (trap states) 的數量增加時，碲硒化鋅半導體光激發光的衰減速率會變慢、光頻譜的半寬會變寬；然而，當碲原子局域性能態與共價帶的邊緣能態開始混成之後，碲硒化鋅半導體光激發光的生命期和光頻譜的半寬都會產生下降的趨勢。

最後，我們用時間解析光頻譜技術來討論碲化鎘膠質量子點之間能量轉移的現象。量子點間的能量轉移的效率不但會與小尺寸量子點的放射譜和大尺寸量子點的吸收譜的重疊程度有關，還會與量子點之間的距離有關。在混合的量子點溶液和固態薄膜中，發現小尺寸的量子點的光激發光強度和生命期會變低，然而大尺寸的量子點的光激發光強度和生命期會變高，這些實驗結果是鄰近量子點極性耦合產生的共振能量轉移的直接證據。在混合的量子點固態薄膜中，隨著量測能量的降低，延伸參數 (β) 會隨之增加，並且趨向一，這個現象直接反映了有效率的能量轉移從小的量子點至大的量子點。

Optical Properties of II-VI Compound Semiconductors and Nanocrystals

Student: Yan-Cheng Lin

Advisor: Dr. Wu-Ching Chou

**Institute of Electrophysics
National Chiao Tung University**

Abstract

The first part of this thesis explores the optical phonon modes and crystal characteristics of $\text{Zn}_{1-x}\text{Cd}_x\text{Se}$ ($0 \leq x \leq 0.32$) and $\text{Zn}_{1-x}\text{Mn}_x\text{Te}$ ($0 \leq x \leq 0.26$) thin films using high-pressure techniques and optical spectroscopy. The phonon Raman spectra of ZnCdSe and ZnMnTe all exhibit intermediate phonon modes. The pressure-dependent longitudinal optical phonon frequencies and the Grüneisen parameter were obtained by quadratic polynomial fitting. The pressure-driven resonant Raman scattering effect was observed in $\text{Zn}_{1-x}\text{Cd}_x\text{Se}$ with a high Cd concentration, and it was exploited to analyze the crystal characteristics of ZnMnTe, which has weak Raman signals under ambient conditions. The pressure at the onset of metallic phase transition (Pt) declines as the Cd and Mn contents increase. As the Cd (Mn) concentration increases from 0 to 0.32 (0 to 0.26), the Pt falls from 13.6 to 9.4 (15.7 to 10.3) GPa.

The vibrational, electronic, and crystalline characteristics of n-type chlorine-doped ZnSe (ZnSe:Cl) layers with a carrier concentration from 8.2×10^{15} to $1.8 \times 10^{18} \text{ cm}^{-3}$ were also studied by Raman spectroscopy. The spectral lineshapes of the longitudinal-optical-phonon and plasmon coupling (LOPC) modes are analyzed using the Raman scattering efficiency and

the dielectric function to determine the electron densities and mobility. The metallic phase transition pressure of ZnSe:Cl layers decreases as the carrier concentration increases, indicating that n-type doping reduces crystal stability. Additionally, the pressure-induced weakening of the LOPC efficiency suggests that pressure tends to degrade the n-type characteristic of ZnSe:Cl because of the emergence of a new deep donor-like state.

In the second part of this thesis we found that the Kohlrausch's stretched exponential law is correlated well with the PL decay profiles of $\text{ZnSe}_{1-x}\text{Te}_x$. As the Te concentration increases, the stretching exponent β initially declines and then monotonically increases. This result can be understood using the hopping-transport and energy transfer model. An increase in the number of isoelectronic Te localized traps reduces the PL decay rate and increases the linewidth, whereas the hybridization of the Te localized states with the valence-band edge states reduces both the lifetime and the linewidth.

Finally, the transfer of electronic energy between CdTe colloidal quantum dots (QDs) was studied using time-resolved photoluminescence (PL) spectroscopy. The efficiency of energy transfer in QDs depends not only on the spectral overlap of small dots emission and large dots absorption, but also on the inter-dot distances. The quenching of the PL intensity (lifetime) of small dots, as well as an enhancement of large dots in mixed solution and a solid film are evidence of a resonant transfer of energy due to dipolar coupling between proximal QDs. In a solid with mixed QDs, the stretching exponent β increases as the probe-energy declines, and approaches one, implying efficient energy transfer from smaller to larger QDs.

Acknowledgements

時光飛逝，我的求學生涯，隨著這本論文的完成即將畫下句點，回想在交大做研究的日子，有歡笑也有淚水。從一開始實驗室搬遷、空間規畫和儀器架設、參加人生最後一次期末考、第一篇論文接受發表、通過資格考直到最後論文口試，一路走來遭遇許多困難與挫折，但也因為有你們的陪伴與提攜，總是在我最失落時，給我建議、鼓勵與支持，成為我繼續往前邁進的最大動力，讓我能夠再次實現自我、提升自己，並完成博士學位。

在這段日子裡，最感謝的是我的指導教授－周武清博士，帶領我進入光電半導體的研究領域。七年來，在周老師的耐心指導下，使我從一個懵懂專題生，逐漸對物理研究產生興趣，最後完成博士論文。從老師身上，我感受到學術研究家的專注與深思，以及待人處事的細心與氣度，老師的身教及言教，一直以來都是我最尊崇的榜樣。謝謝老師多年來對我的栽培，您總是不厭其煩地教導我每一件事情，不斷提醒我做事應該更細心與仔細；與人相處應該和善與尊重；從事學術研究應走出去多看、多學、多討論，您的教導與提醒，我會銘記在心。

感謝褚德三教授將珍貴的實驗儀器留給我們，讓我能順利完成這本論文。雖然與您討論的次數不多，但是您淵博的學問與豐富人生經驗卻一直是我尊敬與學習的目標。我也要感謝楊賜麟教授、中原物理系邱寬城教授與沈志霖教授對我論文的建議，以及對我多年來的照顧，讓我能順利完成學業。感謝成大地科系余樹楨教授在高壓技術、觀念及論文寫作上給予我非常多寶貴的建議，讓我的知識更為正確且深入，也謝謝您一直以鼓勵的方式激勵我，讓我不至於一直否定自己。感謝光電所謝文峰教授、中央電機系綦振瀛教授對我論文內容的建議和指教，讓我獲益良多。感謝實驗室所有成員及過去曾經與我一起熬夜打拼的學弟妹們，謝謝你們的加油、鼓勵與歡笑聲，一切點滴也同時記錄於這本論文中，也只有我們感受的到。

最要感謝的還有我的女友Michelle，謝謝妳多年的照顧、陪伴、體諒與包容，沒有妳一路上的支持與鼓勵，我無法順利完成學業，並進入人生下一個階段。你總在我最失

落時，鼓勵我、替我難過，是妳給我信心，要我相信自己，也讓我更加堅定。每當我小有收穫時，妳陪著我慶祝，並告訴我不可驕傲放縱，要再接再厲、自我突破。最要感謝的還有我的父母、大姊與二姊，你們對我的養育、栽培、關愛、包容與支持，並給予我所有的一切，讓我能無後顧之憂地專注於研究工作，並在求學之路上持續邁進。感謝爸媽，對你們的感恩之意溢於言表，已超乎筆墨所能形容！

最後僅將這本論文獻給我最敬愛與最疼愛我的父母親，所有成就與榮耀都屬於你們！

林彥丞 于新竹交大

January 11, 2009



Contents

Abstract in Chinese	<i>i</i>
Abstract in English	<i>iii</i>
Acknowledgements	<i>v</i>
Contents	<i>vii</i>
List of Figures	<i>ix</i>
List of Tables	<i>xiv</i>
Chapter 1 Introduction	<i>1</i>
1.1 Physical Properties of Semiconductors under High Pressure	<i>2</i>
1.2 Optical Properties of Isoelectronic Semiconductors	<i>6</i>
1.3 Electronic Energy Transfer in Semiconductor Nanocrystals	<i>8</i>
Chapter 2 Experimental Details	<i>15</i>
2.1 High-Pressure Techniques	<i>15</i>
2.2 Optical Spectroscopy	<i>29</i>
Chapter 3 Pressure-Dependent Raman Scattering and Photoluminescence of	
$\text{Zn}_{1-x}\text{Cd}_x\text{Se}$	<i>34</i>
Chapter 4 Pressure-Induced Metallization and Resonant Raman Scattering in	
$\text{Zn}_{1-x}\text{Mn}_x\text{Te}$	<i>55</i>
Chapter 5 Raman Scattering of Longitudinal Optical Phonon-Plasmon Coupling in	

	Cl-Doped ZnSe under High Pressure	70
Chapter 6	Time-Resolved Photoluminescence of Isoelectronic Traps in ZnSe_{1-x}Te_x Semiconductor Alloys	92
Chapter 7	Electronic Energy Transfer in CdTe Colloidal Quantum Dots	104
Chapter 8	Conclusions	116
Publication Lists		118



List of Figures

- FIG. 2.1. (a) Schematic depiction of diamond anvil cell (DAC). **24**
- FIG. 2.1. (b) Diamond anvil cell as used in this thesis. **24**
- FIG. 2.2. Section of gasket indentation area and the sample chamber. **25**
- FIG. 2.3. Energy levels of Cr^{3+} in Al_2O_3 . The transitions $E_{1/2} \rightarrow A$ and $E_{3/2} \rightarrow A$ yield R1 and R2 lines, respectively. **26**
- FIG. 2.4. Wavelength of ruby fluorescence against pressure. [Ref. 19] **27**
- FIG. 2.5. Pressure-dependent ruby fluorescence spectra at room temperature. **28**
- FIG. 2.6. Schematic scattering of light. **31**
- FIG. 2.7. Experimental setup of micro-Raman (PL) system. **32**
- FIG. 2.8. Experimental setup of time-resolved PL system. **33**
- FIG. 3.1. Raman spectra of $\text{Zn}_{1-x}\text{Cd}_x\text{Se}$ epilayers ($0 \leq x \leq 0.32$) at 300 K and ambient pressure. **47**
- FIG. 3.2. Dependence of LO phonon frequencies (open circle) and FWHM (solid triangle) on Cd concentration (x). **48**
- FIG. 3.3. Raman spectra of $\text{Zn}_{1-x}\text{Cd}_x\text{Se}$ epilayers ($0 \leq x \leq 0.32$) at 100 K and ambient pressure. The impurity (I) modes, indicated by black arrows, appear at low temperature. The LO and TO phonons of the GaAs substrate are also labeled. **49**
- FIG. 3.4. Up-stroke pressure-dependent Raman spectra of $\text{Zn}_{1-x}\text{Cd}_x\text{Se}$ ($x = 0.06$) at room temperature. The LO phonon disappears at around 13.0 GPa, revealing a structural

change from semiconductor to metal. **50**

FIG. 3.5. Down-stroke pressure-dependent Raman spectra of $\text{Zn}_{1-x}\text{Cd}_x\text{Se}$ ($x = 0.06$) at room temperature. The splitting of the TO phonon, labeled by black arrows, was observed clearly as the pressure was released. **51**

FIG. 3.6. Up-stroke pressure-dependent Raman spectra of $\text{Zn}_{1-x}\text{Cd}_x\text{Se}$ ($x = 0.25$) at room temperature. The pressure-driven resonant Raman scattering effect occurred as the pressure was increased. The LO phonon was found to disappear at about 11.0 GPa. **52**

FIG. 3.7. Pressure-dependent photoluminescence spectra of $\text{Zn}_{1-x}\text{Cd}_x\text{Se}$ ($x = 0.25$) at 300 K. The 514.5 nm (2.41 eV) Ar^+ laser was fixed as an excitation source. The black dashed arrow at 2.41 eV labels the energy of the excitation laser, whereas the Stokes and anti-Stokes Raman spectra occur at the lower and higher energy sides of the laser, respectively. The inset plots the pressure dependence of PL energies, and the dashed line indicates the energy of the excitation laser. **53**

FIG. 3.8. Cd concentration (x)-dependent phase transition (semiconductor-to-metal) pressure of $\text{Zn}_{1-x}\text{Cd}_x\text{Se}$ epilayers. The solid curve represents a quadratic polynomial fit. **54**

FIG. 4.1. Raman spectra of $\text{Zn}_{1-x}\text{Mn}_x\text{Te}$ ($0 \leq x \leq 0.26$) at 300 K under ambient pressure. The excitation source is a 514.5 nm line from an Ar^+ laser. **65**

FIG. 4.2. Dependence of LO phonon frequencies (open circle) and PL energy (solid square) on Mn concentration (x) at room temperature. The solid curve is a quadratic polynomial fit for the LO phonon. **66**

FIG. 4.3. Up-stroke pressure-dependent Raman spectra of ZnTe at 300 K. Black arrows

indicate the LO and the TO phonons. The excitation source is a 488.0 nm line from an Ar⁺ laser. The pressure-induced RRS enhancement occurs as the external pressure is increased. **67**

FIG. 4.4. Up-stroke pressure-dependent Raman spectra of Zn_{0.91}Mn_{0.09}Te at 300 K. LO, TO, LO + TA, and impurity (*I*) modes are labeled. **68**

FIG. 4.5. Mn concentration (*x*)-dependent semiconductor-to-metal phase transition pressure of Zn_{1-x}Mn_xTe. The solid curve is a quadratic polynomial fit, given by $P_t(x) = 15.7 - 25.4x + 19.0x^2$ (GPa). **69**

FIG. 5.1. Raman spectra (open circles) with calculated lineshape analysis (solid lines) of n-type ZnSe:Cl layers for various carrier densities at 300 K and ambient pressure, including Lorentzian fit for the TO phonon. **84**

FIG. 5.2. Carrier concentration obtained at 300 K from Hall measurement n_H (full squares), compared with those obtained from optical Raman measurement n_R (open circles), as function of ZnCl₂ source temperature. The dashed line is merely a guide for the eye. **85**

FIG. 5.3. Mobility obtained at 300 K from Hall measurement μ_H versus those obtained from optical Raman measurement μ_R . The solid, dashed, and dotted lines, respectively, represent the ratio, $\mu_H/\mu_R = 1, 2,$ and 3 . **86**

FIG. 5.4. (a) Up-stroke pressure-dependent Raman spectra of the ZnSe:Cl layer ($n_H = 8.2 \times 10^{15} \text{ cm}^{-3}$) at 300 K. The behavior of mode *I* and the TO phonon are indicated by solid and dashed arrows, respectively. (b) Pressure dependence of Raman shifts for LO, TO, TO split, and mode *I* of ZnSe:Cl layer ($n_H = 8.2 \times 10^{15} \text{ cm}^{-3}$). The solid curves are quadratic polynomial fits. **87**

FIG. 5.5. (a) Up-stroke pressure-dependent Raman spectra of the ZnSe:Cl layer ($n_H = 1.8 \times 10^{18} \text{ cm}^{-3}$) at 300 K. The LO phonon disappears at about 12.5 GPa. (b) Pressure-dependent Raman shifts of ZnSe:Cl layer ($n_H = 1.8 \times 10^{18} \text{ cm}^{-3}$). The solid curves represent quadratic polynomial fits. **88**

FIG. 5.6. Carrier concentration (n_H)-dependent semiconductor-to-metal phase transition pressure of n-type ZnSe:Cl layers. The dashed curve represents a quadratic polynomial fit. The inset displays the PL spectra of undoped ZnSe and the n-type ZnSe:Cl layers at 300 K, excited by an He-Cd 325 nm laser. **89**

FIG. 5.7. Pressure-dependent LO phonon of undoped ZnSe (full squares) and LOPC mode of n-type ZnSe:Cl for $n_H = 8.2 \times 10^{15} \text{ cm}^{-3}$ (open triangles) and $n_H = 1.8 \times 10^{18} \text{ cm}^{-3}$ (full circles). The solid curve is a quadratic polynomial fit of an undoped ZnSe LO phonon, and the dashed curve is the same curve but shifted downward to capture the presumed behavior of the LOPC mode of ZnSe:Cl ($n_H = 1.8 \times 10^{18} \text{ cm}^{-3}$). The inset plots the pressure-dependent FWHM of the undoped ZnSe LO phonon and the ZnSe:Cl LOPC mode ($n_H = 1.8 \times 10^{18} \text{ cm}^{-3}$). **90**

FIG. 5.8. Schematic band structure of n-type ZnSe:Cl. (a) At ambient pressure, the energy difference between the D state and the conduction band minimum, $\Delta E (E_D - E_C)$, is positive. (b) With compression, $\Delta E (E_D - E_C)$ declines and eventually becomes negative. **91**

FIG. 6.1. Normalized PL spectra of $\text{ZnSe}_{1-x}\text{Te}_x$ ($0 \leq x \leq 1$) at 13 K. **100**

FIG. 6.2. TRPL spectra of $\text{ZnSe}_{1-x}\text{Te}_x$ at 13 K. The inset plots the data on a double logarithmic scale; the stretched-exponential function is then a straight line. **101**

FIG. 6.3. (a) PL lifetime, (b) PL linewidth, and (c) stretching exponent β of $\text{ZnSe}_{1-x}\text{Te}_x$ as functions of Te concentration. **102**

FIG. 6.4. (a) Dependence of TRPL measurements on probing energies of $\text{ZnSe}_{0.90}\text{Te}_{0.10}$. (b) TRPL image of $\text{ZnSe}_{0.90}\text{Te}_{0.10}$. **103**

FIG. 7.1. (a) PL spectra of 3.3 nm CdTe QDs in water at various concentrations - $1 \text{ mol} \cdot \text{L}^{-1}$ (solid), $5.0 \times 10^{-2} \text{ mol} \cdot \text{L}^{-1}$ (dashed), and $1.0 \times 10^{-4} \text{ mol} \cdot \text{L}^{-1}$ (dotted). (b) PL peak intensity versus concentration of QDs. (c) Temporal evolution of PL spectra of QDs ($1.0 \times 10^{-1} \text{ mol} \cdot \text{L}^{-1}$). **111**

FIG. 7.2. (a) Absorption spectra of pure small (donor) and pure large (acceptor) CdTe QDs in water. PL spectra of pure donors (D), pure acceptors (A), and mixed (M) CdTe QDs (b) in water, and (c) solid. **112**

FIG. 7.3. TRPL spectra of (a) donors in pure and mixed solution probed at 537 nm, and (b) acceptors in pure and mixed solution probed at 618 nm. **113**

FIG. 7.4. (a) Dependence of TRPL measurements on probing energies of mixed CdTe QDs solid. (b) Time-resolved PL image of mixed CdTe QDs solid. Inset plots the TRPL data obtained at 2.27 eV (open squares) and 1.95 eV (open circles) on a double logarithmic scale. **114**

FIG. 7.5. True-color images of pure small, pure large and mixed QDs in solution and solid. **115**

List of Tables

Table 3.1 LO and TO phonon frequencies and FWHM of LO phonon for $\text{Zn}_{1-x}\text{Cd}_x\text{Se}$ epilayers.

45

Table 3.2 Pressure-dependent LO phonon frequencies (ω_{LO}), $d\omega_{\text{LO}}/dp$, calculated mode Grüneisen parameters (γ_{LO}) and phase transition pressures for $\text{Zn}_{1-x}\text{Cd}_x\text{Se}$ epilayers. **46**

Table 4.1 Pressure-dependent LO, TO, and I phonon frequencies (ω_i), $d\omega_i/dp$, calculated mode Grüneisen parameters (γ_i), and phase transition pressures of $\text{Zn}_{1-x}\text{Mn}_x\text{Te}$.

64

Table 5.1 Hall carrier concentration (n_H) and mobility (μ_H), LOPC mode frequencies, linewidth (FWHM) and peak intensity ratio ($I_{\text{LOPC}} / I_{\text{TO}}$) of all studied ZnSe samples with various ZnCl_2 doping temperatures (T_{Cl}). **82**

Table 5.2 Carrier concentration (n_R), mobility (μ_R), and mobility ratios (μ_H / μ_R) obtained by optical Raman measurements. Plasmon frequency (ω_p), plasmon damping constant (γ), and phonon damping constant (Γ) are derived by the calculated lineshape analysis. **83**

Chapter 1 Introduction

The main focus of this thesis is to study the optical properties of II-VI compound semiconductors and nanocrystals (NCs). This dissertation comprises three parts: (1) physical properties of semiconductors under high pressure, (2) optical properties of isoelectronic semiconductors, and (3) electronic energy transfer in semiconductor NCs.

This thesis is organized as follows. This chapter introduces the history of high-pressure research and the physical properties of semiconductors under high pressure (Section 1.1), the unique optical characteristics of isoelectronic semiconductors (Section 1.2), and the electronic energy transfer in semiconductor NCs (Section 1.3); it also presents the latest relevant scientific findings. Chapter 2 describes the high-pressure techniques used and the optical measurements made in this study. Chapters 3, 4, and 5 present the experimental results and discussion of the first part of this thesis. Chapter 3 discusses the physical properties of $\text{Zn}_{1-x}\text{Cd}_x\text{Se}$ at high pressure using photoluminescence (PL) and Raman scattering. Chapter 4 studies the metallic phase transition of $\text{Zn}_{1-x}\text{Mn}_x\text{Te}$ using the pressure-induced resonance Raman scattering approach. Chapter 5 discusses LO-phonon-plasmon coupling, structural stability, and carrier concentration as functions of applied hydrostatic pressure in n-type chlorine-doped ZnSe ($\text{ZnSe}:\text{Cl}$) using Raman spectroscopy. Chapter 6, the second part of the thesis, explores the decay dynamics of isoelectronic traps in $\text{ZnSe}_{1-x}\text{Te}_x$ semiconductors using time-resolved PL. Chapter 7, the third part of the thesis, compares in detail the electronic energy transfer behavior of mixed CdTe quantum dots solution with that of the solid, using time-resolved and spectrally-resolved PL. Finally, Chapter 8 summarizes this thesis.

1.1 Physical Properties of Semiconductors under High Pressure

I. History of High-Pressure Research

Materials under high pressure exhibit interesting physical properties. High pressure conditions exist at the center of the earth and in both natural and man-made explosions. Furthermore, hydrostatic pressure can be continuously tuned from ambient pressure to ultra-high pressure in a laboratory using a diamond anvil cell (DAC), which is a device that is sufficiently small that it can fit in the palm of a hand. The transparency of diamond over a wide range of frequencies from the near ultraviolet (~ 5.5 eV) to the infrared is the most important and useful characteristic for optical measurements.

The DAC can generate high pressures because of the exceptional hardness of diamond, but even high-quality diamonds will shatter under sufficiently high loads. The hydrostatic pressure applied by the DAC can be adopted to study the pressure-dependent physical properties of condensed matter, including insulators, semiconductors and metals. Studies of the pressure-dependent physical properties of condensed matters have in the past been limited by experimental techniques, which could not generate high enough pressures to cause significant changes in the physical properties. Recently, however, this limitation has been overcome and ultra-high pressures of several mega-bars can now be generated. (One mega-bar is approximately one million atmospheres of pressure or 100 giga-pascals (GPa) in SI units.) Therefore, high-pressure techniques have become powerful tools in studying the physical properties of condensed matter.

Hydrostatic pressure, as an external thermodynamic parameter, is a convenient probe of crystalline stability. Accordingly, one of the interesting phenomena that occur under applied pressure is a sudden rearrangement of atoms, in structural phase transitions. The applied pressure reduces the lattice constant and the crystalline volume, markedly changing the inter-atomic bonding. Research into such phenomena logically begins with hydrogen, the

simplest element, which is the first in the Periodic Table, and the most abundant in the gravitationally compressed interiors of Jupiter, Saturn and some of the newly discovered extrasolar planets. Many solids that are electrical insulators at atmospheric pressure become metallic at high pressure at 300 K in the DAC; they include BaSe [1], xenon [2,3], sulphur [4], and oxygen [5]. During the past two decades, much effort has been made to realize metallic hydrogen at ultrahigh pressures [6-10]. However, the robust evidence for the metallic hydrogen in the form of either optical or conductivity measurements remains. Although the quest to observe metallic hydrogen in the laboratory is ongoing, high-pressure methods have advanced significantly and a variety of surprising new phenomena have been observed. The developments are crucial to deepening our understanding of condensed matter.

II. Semiconductor Thin Films under High Pressure

As hydrostatic pressure can be utilized to tune electronic energy bands and change the crystal phases of semiconductors, the high-pressure method has been established as an important tool for understanding the optical and crystal characteristics of semiconductors. Rapid advances in epitaxial growth and high-pressure techniques, as well as the development of sophisticated data analysis methods, have facilitated investigations of the physical properties of II–VI and III–V semiconductors under high pressure.

Notably, ZnSe is an important semiconductor in II–VI compounds. Tuchman *et al.* [11] studied pressure-dependent exciton recombination in bulk ZnSe and in strained and strain-relaxed ZnSe epilayers grown on GaAs substrates. They found that the energy difference between heavy- and light-hole excitons in strained ZnSe film initially decreases as applied pressure increases. When the pressure is increased to around 2.9 GPa, the crossover of heavy- and light-hole excitons energy is observed, revealing that strain in the ZnSe film transforms from a compressive to tensile strain. Smith and Martin [12] demonstrated that

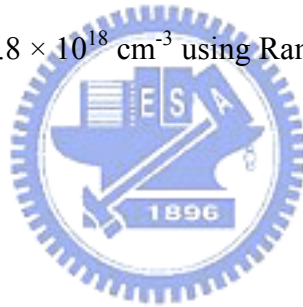
ZnSe undergoes a crystallographic phase transition from a four-fold coordinated zincblend (ZB) structure into a six-fold coordinated rocksalt (RS) structure at about 13.5 GPa, as determined by x-ray diffraction. Itkin *et al.* [13] examined the marked decline in resistance from 10^{21} to $10^4 \Omega$ in ZnSe at 13.5 GPa, which indicates that pressure-induced metallization of ZnSe occurs when the crystalline structure is transformed from ZB into RS. High-pressure optical studies by Cardona's group [14] showed that the direct energy gap of ZnSe monotonically increases as the pressure is increased. At 13.5 GPa the sample becomes opaque, indicating the metallic phase transition. Moreover, Arora *et al.* [15,16] demonstrated that Raman scattering is another approach to exam high-pressure phases of semiconductors. The disappearance of Raman signals at high pressure is evidence of semiconductor-to-metal phase transition due to changes in the Raman selection rule or extremely poor scattering efficiency in the metallic phase.

In the recent decade, high-pressure investigations by Chou's group have analyzed the physical properties of epitaxial-grown II–VI semiconductors, such as undoped ZnSe [17] and ZnSe-based ternary compounds ZnMnSe [18], ZnFeSe [17], ZnCdSe [19] and ZnSeTe [20]. Energy-dispersive X-ray diffraction (EDXD), Raman scattering and photoluminescence (PL) have been extensively applied to elucidate the structural stability, vibrational modes, and electronic transitions of these semiconductors. The authors observed that phase-transition pressure in ternary compound semiconductors decreases as the substituted element content increases. The reduction behavior in phase-transition pressure of the ZnSe-based ternary semiconductors depends on the fractional volume change ($\Delta V/V_0$), not the kinds of impurity ions doped. Furthermore, the authors suggest that the disappearance of longitudinal optical phonons at which the phase becomes metal is due to the extremely thin penetration depth (skin depth) for incident light.

In 2003, Mujica *et al.* [21] reviewed the high-pressure structures of group-IV elements,

and III–V, and II–VI compound semiconductors. Although this investigation presents sufficient experimental and theoretical results for binary II–VI and III–V semiconductors, the physical properties of n-type and p-type semiconductors and ternary compounds under pressure when one element is replaced by a third element remain unclear.

Chapter 3 discusses in detail the PL and Raman scattering of $\text{Zn}_{1-x}\text{Cd}_x\text{Se}$ under high pressure because the semiconductor-to-metal phase transition and crystalline stability of $\text{Zn}_{1-x}\text{Cd}_x\text{Se}$ at hydrostatic pressure remain controversial. Chapter 4 describes the effect of applied pressure on physical properties of $\text{Zn}_{1-x}\text{Mn}_x\text{Te}$ using the resonance Raman Scattering approach. Analytical results are useful when investigating the magnetic properties of p-doped $\text{Zn}_{1-x}\text{Mn}_x\text{Te}$ under high pressure. Chapter 5 discusses comprehensively LO-phonon-plasmon coupling as a function of applied hydrostatic pressure in n-type ZnSe:Cl with a carrier concentration of 8.2×10^{15} to $1.8 \times 10^{18} \text{ cm}^{-3}$ using Raman spectroscopy.



1.2 Optical Properties of Isoelectronic Semiconductors

In addition to donors, acceptors, and electrically inactive impurities in semiconductors, there exists a fascinating subset designated as *isoelectronic* [22]: an impurity that replaces a host atom with the same valence orbital is labeled isoelectronic. Localized states in the forbidden band generally exist because of the excitons that are bound to such centers. Nitrogen that replaces phosphorus in GaP is an example of such a trap [23]. The bonding scheme of substitutional donors or acceptors in the tetrahedrally coordinated semiconductors is based on the sp^3 hybridized covalent bond. For example, consider GaP that is doped with Zn and S. Zn that replaces Ga is an acceptor and S that replaces P is a donor. As well as acceptor-bound holes and donor-bound electrons, such crystals contain donor-bound and acceptor-bound excitons [24], which are bound to the neutral donors and acceptors by a van der Waals interaction. However, N and Bi, replacing P in GaP, have the same number of valence electrons as P, but they can trap a charge carrier by a non-Coulombic, short-range impurity potential, which arises from the substantial difference between the electronegativity of N and that of P (or Bi and P). The impurity, originally neutral, then acquires a charge relative to the lattice. The impurity N (Bi) is called an isoelectronic acceptor (donor), based on the type of the charge carrier (electron or hole) that is bound to it [25]. Bound excitons arise when the Coulomb field of this charge binds a second charge carrier of the opposite sign. The exciton binding energy of isoelectronic impurities ranges from tens to hundreds of meV, depending on the impurity and the host. Isoelectronic impurities have been fascinating subjects of investigation with photoluminescence, absorption, PL excitation, and localized vibrational modes; they play an important role in optoelectronic device applications.

The number of investigations of isoelectronic $\text{ZnSe}_{1-x}\text{Te}_x$ ternary compound semiconductors has increased remarkably. The surge in activity has been a response to their unique and interesting physical properties. These properties include, for example, the unusual

spontaneous formation of a superlattice [26], large band-gap bowing [27], and a broad emission linewidth [27,28]. The band anticrossing (BAC) model [29,30] based on the Green's function calculation [31,32] has been proposed to elucidate the large band-gap bowing and the broadening of the emission linewidth. Additionally, the transfer of excitons among the Te localized sites in $\text{ZnSe}_{1-x}\text{Te}_x$ with a low Te concentration has been studied [28]. The self-trapped excitons that are bound to various isoelectronic centers (ICs) dominate the optical properties of ZnSeTe . Akimova *et al.* utilized cathodoluminescence to obtain direct experimental evidence of Te-bound emissions [33].

Of all of the fascinating optical properties, however, little attention has been paid to the decay dynamics of isoelectronic ZnSeTe semiconductors. Chapter 6 will discuss in detail the decay dynamics of isoelectronic traps in $\text{ZnSe}_{1-x}\text{Te}_x$ semiconductor alloys.



1.3 Electronic Energy Transfer in Semiconductor Nanocrystals

In addition to semiconductor heterostructures, highly luminescent colloidal quantum dots (QDs) or semiconductor nanocrystals (NCs) are attracting increasing interest in science, with potential for use in diverse fields, including light-emitting diodes [34], photodetectors [35], biosensing [36], and biolabeling [37]. Very recently, increasing research effort has been devoted to the new generation of solar cells which contain NCs as active materials [38-40]. Colloidal QDs are easily synthesized with low energy and material consumption [41]. They are perfect building blocks for controlled nano assemblies on a molecular scale, such as spatially ordered structures [42] or colloidal supercrystals [43]. The typical length scale of QDs is responsible for chemical and physical properties that differ markedly from those of both their bulk and molecular counterparts. The properties of QDs depend on their size, shape and surface effects. Over the last two decades, extensive studies that have applied optical techniques to CdSe QDs.

Energy transfer between semiconductor NCs has attracted substantial interest in recent years [44-51]. Förster resonance energy transfer (FRET) is a nonradiative process that is driven by dipole–dipole interactions [52-54]. The efficiency of FRET depends on the degree of spectral overlap between the emission spectrum of the donor and the absorption spectrum of the acceptor, and on the sixth power of the separation between the donor and acceptor pair. The rate of nonradiative energy transfer according to the Förster theory is given by the formula [54],

$$k_T = \left(\frac{1}{\tau_D} \right) \times \left(\frac{R_0}{r} \right)^6, \quad (1)$$

where τ_D represents the excited-state radiative lifetime of the donor in the absence of transfer and R_0 is the Förster critical radius. R_0 (in angstrom) is given by

$$R_0 = 0.2108 \left[\kappa^2 \Phi_D n^{-4} \int_0^\infty I_D(\lambda) \varepsilon_A(\lambda) \lambda^4 d\lambda \right]^{1/6}, \quad (2)$$

where κ^2 is the orientational factor and depends on the relative orientation of the donor and acceptor dipoles. The values of κ^2 range from 0 (perpendicular) to 4 (collinear). Φ_D denotes the fluorescence quantum yield of the donor in the absence of transfer; n is the average refractive index of the medium in the wavelength range where spectral overlap is significant; $I_D(\lambda)$ is the fluorescence spectrum of the donor normalized such that $\int_0^\infty I_D(\lambda) d\lambda = 1$; $\varepsilon_A(\lambda)$ is the molar absorption coefficient of the acceptor, and λ is the wavelength in nanometers.

The transfer efficiency is given by

$$\Phi_T = \frac{k_T}{1/\tau_D + k_T} = \frac{1}{1 + (r/R_0)^6}. \quad (3)$$

According to Eq. (3), the dipole-dipole coupling mechanism is most sensitive to the donor-acceptor distance when this distance is comparable to the Förster critical radius. The characteristics of FRET can be adopted as a “spectroscopic ruler” [55]. FRET has been widely employed *in vivo* and *in vitro* biological studies, such as the monitoring of DNA hybridization and sequencing, protein conformation studies, and diffusion dynamics [55].

In contrast, radiative transfer is a two-step process: an acceptor absorbs a photon that is emitted by a donor. This process occurs when the average distance between the donor and acceptor exceeds the wavelength. Such a transfer does not involve any interaction between particles. Radiative transfer results in a decrease of the donor fluorescence intensity in the region of spectral overlap. The fraction a of photons emitted by donors and absorbed by acceptors is given by

$$a = \frac{2.3}{\Phi_D} C_A I \int_0^\infty I_D(\lambda) \varepsilon_A(\lambda) d\lambda, \quad (4)$$

where C_A is the molar concentration of acceptors [54].

The FRET process in semiconductor nanocrystals has recently attracted great interest. Bawendi’s group was the first to demonstrate the FRET process between close-packed CdSe

QDs [44,45]. Crooker *et al.* elucidated FRET dynamics in monodisperse, mixed-size, and layered assemblies of CdSe/ZnS QDs using time-resolved and spectrally-resolved PL [46]. They all found an enhancement in luminescence and lifetime of the acceptor that was accompanied by a reduction of both of the donor. These phenomena are direct evidence of energy transfer from small to large QDs, eliminating the reabsorption effect, which would not increase the decay rate from small QDs. Very recently, Feldmann's group also studied the cascaded FRET in a funnel-like structure and FRET in layer-by-layer assemblies of CdSe and water-soluble CdTe QDs [47-51]. The FRET process in an aqueous solution of QDs, which holds much promise for use in biological studies, is limited by the inter-dot distance and the spectral overlap between the donor emission and the acceptor absorption. Chapter 7 compares in detail the electronic energy transfer behavior of mixed CdTe QDs solution with that of the solid using time-resolved and spectrally-resolved PL.



References

- [1] S. T. Weir, Y. K. Vohra, and A. L. Ruoff, *Phys. Rev. B* **35**, 874 (1987).
- [2] R. Reichlin, K. E. Brister, A. K. McMahan, M. Ross, S. Martin, Y. K. Vohra, and A. L. Ruoff, *Phys. Rev. Lett.* **62**, 669 (1989).
- [3] K. A. Goettel, J. H. Eggert, and I. F. Silvera, *Phys. Rev. Lett.* **62**, 665 (1989).
- [4] H. Luo, S. Desgreniers, Y. K. Vohra, and A. L. Ruoff, *Phys. Rev. Lett.* **67**, 2998 (1991).
- [5] S. Desgreniers, Y. K. Vohra, and A. L. Ruoff, *J. Phys. Chem.* **94**, 1117 (1990).
- [6] H. K. Mao and R. J. Hemley, *Rev. Mod. Phys.* **66**, 671 (1994).
- [7] S. T. Weir, A. C. Mitchell, and W. J. Nellis, *Phys. Rev. Lett.* **76**, 1860 (1996).
- [8] H. K. Mao and R. J. Hemley, *Science* **244**, 1462 (1989).
- [9] C. Narayana, H. Luo, J. Orloff, and A. L. Ruoff, *Nature* **393**, 46 (1998).
- [10] P. Loubeyre, F. Occelli, and R. LeToullec, *Nature* **416**, 613 (2002).
- [11] J. A. Tuchman, S. Kim, Z. Sui, and I. P. Herman, *Phys. Rev. B* **46**, 13371 (1992).
- [12] P. L. Smith and J. E. Martin, *Phys. Lett.* **19**, 541 (1965).
- [13] G. Itkin, G. R. Hearne, E. Sterer, M. P. Pasternak, and W. Potzel, *Phys. Rev. B* **51**, 3195 (1995).
- [14] S. Ves, K. Strössner, N. E. Christensen, C. K. Kim, and M. Cardona, *Solid State Commun.* **56**, 479 (1985).
- [15] A. K. Arora, D. U. Bartholomew, D. L. Peterson, and A. K. Ramdas, *Phys. Rev. B* **35**, 7966 (1987).
- [16] A. K. Arora and T. Sakuntala, *Phys. Rev. B* **52**, 11052 (1995).
- [17] C. M. Lin, D. S. Chuu, T. J. Yang, W. C. Chou, J. Xu, and E. Huang, *Phys. Rev. B* **55**, 13641 (1997).
- [18] C. S. Yang, C. S. Ro, W. C. Chou, C. M. Lin, D. S. Chuu, J. Hu, E. Huang, and J. Xu, *J. Appl. Phys.* **85**, 8092 (1999).

- [19] C. M. Lin, D. S. Chuu, J. Xu, E. Huang, W. C. Chou, J. Hu, and J. Pei, *Phys. Rev. B* **58**, 16 (1998).
- [20] C. S. Yang, W. C. Chou, D. M. Chen, C. S. Ro, J. L. Shen, and T. R. Yang, *Phys. Rev. B* **59**, 8128 (1999).
- [21] A. Mujica, A. Munoz, and R. J. Needs, *Rev. Mod. Phys.* **75**, 863 (2003), and references therein.
- [22] W. Czaja, in *Festkörperprobleme XI*, edited by M. O. Madelung (Pergamon, Oxford, 1971), pp. 65–85.
- [23] D. G. Thomas and J. J. Hopfield, *Phys. Rev.* **150**, 680 (1966).
- [24] P. J. Dean and D. C. Herbert, in *Excitons*, edited by K. Cho (Springer, Berlin, 1979), pp. 55–182.
- [25] J. J. Hopfield, D. G. Thomas, and R. T. Lynch, *Phys. Rev. Lett.* **17**, 312 (1966).
- [26] S. P. Ahrenkiel, S. H. Xin, P. M. Reimer, J. J. Berry, H. Luo, S. Short, M. Bode, M. Al-Jassim, J. R. Buschert, and J. K. Furdyna, *Phys. Rev. Lett.* **75**, 1586 (1995).
- [27] M. J. S. P. Brasil, R. E. Nahory, F. S. Turco-Sandroff, H. L. Gilchrist, and R. J. Martin, *Appl. Phys. Lett.* **58**, 2509 (1991).
- [28] D. Lee, A. Mysyrowicz, A. V. Nurmikko, and B. J. Fitzpatrick, *Phys. Rev. Lett.* **58**, 1475 (1987).
- [29] W. Walukiewicz, W. Shan, K. M. Yu, J. W. Ager III, E. E. Haller, I. Miotkowski, M. J. Seong, H. Alawadhi, and A. K. Ramdas, *Phys. Rev. Lett.* **85**, 1552 (2000).
- [30] W. Shan, W. Walukiewicz, J. W. Ager III, E. E. Haller, J. F. Geisz, D. J. Friedman, J. M. Olson, and S. R. Kurtz, *Phys. Rev. Lett.* **82**, 1221 (1999).
- [31] J. Wu, W. Walukiewicz, K. M. Yu, J. W. Ager III, E. E. Haller, I. Miotkowski, A. K. Ramdas, Ching-Hua Su, I. K. Sou, R. C. C. Perera, and J. D. Denlinger, *Phys. Rev. B* **67**, 035207 (2003).

- [32] J. Wu, W. Walukiewicz, and E. E. Haller, *Phys. Rev. B* **65**, 233210 (2002).
- [33] I. V. Akimova, A. M. Akhekyan, V. I. Kozlovsky, Yu. V. Korostelin, and P. V. Shapin, *Sov. Phys. Solid State* **27**, 1041 (1985).
- [34] S. Coe, W. K. Woo, M. Bawendi, and V. Bulovic, *Nature* **420**, 800 (2002).
- [35] A. Biebersdorf, R. Dietmüller, A. S. Susha, A. L. Rogach, S. K. Poznyak, D. V. Talapin, H. Weller, T. A. Klar, and J. Feldmann, *NanoLett* **6**, 1559 (2006).
- [36] A. P. Alivisatos, *Nat. Biotechnol* **22**, 47 (2004).
- [37] X. Michalet, F. F. Pinaud, L. A. Bentolila, J. M. Tsay, S. Doose, J. J. Li, G. Sundaresan, A. M. Wu, S. S. Gambhir, and S. Weiss, *Science* **307**, 538 (2005).
- [38] I. Gur, N. A. Fromer, M. L. Geier, and A. P. Alivisatos, *Science* **310**, 462 (2005).
- [39] I. Robel, V. Subramanian, M. Kuno, and P. V. Kamat, *J. Am. Chem. Soc.* **128**, 2385 (2006).
- [40] P. V. Kamat, *J. Phys. Chem. C* **111**, 2834 (2007).
- [41] A. L. Rogach, T. Franzl, T. A. Klar, J. Feldmann, N. Gaponik, V. Lesnyak, A. Shavel, A. Eychemüller, Y. P. Rakovich, and J. F. Donegan, *J. Phys. Chem. C* **111**, 14628 (2007).
- [42] A. A. Mamedov, A. Belov, M. Giersig, N. N. Mamedova, and N. A. Kotov, *J. Am. Chem. Soc.* **123**, 7738 (2001).
- [43] A. L. Rogach, D. V. Talapin, E. V. Shevchenko, A. Kornowski, M. Haase, and H. Weller, *Adv. Funct. Mater.* **12**, 653 (2002).
- [44] C. R. Kagan, C. B. Murray, M. Nirmal, and M. G. Bawendi, *Phys. Rev. Lett.* **76**, 1517 (1996).
- [45] C. R. Kagan, C. B. Murray, and M. G. Bawendi, *Phys. Rev. B* **54**, 8633 (1996).
- [46] S. A. Crooker, J. A. Hollingsworth, S. Tretiak, and V. I. Klimov, *Phys. Rev. Lett.* **89**, 186802 (2002).
- [47] T. Franzl, D. S. Koktysh, T. A. Klar, A. L. Rogach, and J. Feldmann, *Appl. Phys. Lett.*

84, 2904 (2004).

[48] T. Franzl, S. Schietinger, A. L. Rogach, and J. Feldmann, *Nano Lett.* **4**, 1599 (2004).

[49] T. Franzl, A. Shavel, A. L. Rogach, N. Gaponik, T. A. Klar, A. Eychmüller, and J. Feldmann, *Small* **1**, 392 (2005).

[50] V. K. Komarala, A. L. Bradley, Y. P. Rakovich, S. J. Byrne, Y. K. Gun'ko, and A. L. Rogach, *Appl. Phys. Lett.* **93**, 123102 (2008).

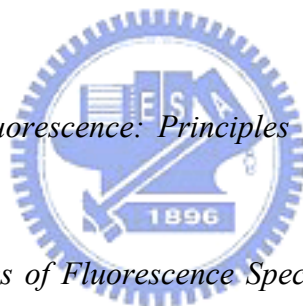
[51] D. Gross, A. S. Susa, T. A. Klar, E. D. Como, A. L. Rogach, and J. Feldmann, *Nano Lett.* **8**, 1482 (2008).

[52] T. Förster, in *Comparative Effects of Radiation*, edited by M. Burton, J. S. Kirby-Smith, and J. L. Magee (Wiley, New York, 1960), p. 301.

[53] D. L. Andrews and A. A. Demidov, *Resonance Energy Transfer*, (Wiley, Chichester, U.K., 1999).

[54] B. Valeur, *Molecular Fluorescence: Principles and Applications*, (Wiley, New York, 2002).

[55] J. R. Lakowicz, *Principles of Fluorescence Spectroscopy*, 2nd Ed., (Kluwer Academic, New York, 1999).




Chapter 2 Experimental Details

This chapter elucidates experimental approaches for the use of the diamond-anvil cell, and for performing Raman scattering studies of phase stability and electronic transition in $\text{ZnCd}_x\text{Se}_{1-x}$, $\text{ZnMn}_x\text{Te}_{1-x}$, and chlorine-doped ZnSe epilayers. The photoluminescence and time-resolved photoluminescence optical setups for examining $\text{ZnSe}_{1-x}\text{Te}_x$ epilayers and CdTe colloidal quantum dots are also depicted. Section 2.1 describes in detail the diamond-anvil cell that is adopted herein and the related techniques. Section 2.2 describes the optical spectroscopy, Raman scattering, photoluminescence, and time-resolved photoluminescence.

2.1 High-Pressure Techniques

I. Diamond Anvil Cell



The diamond-anvil cell (DAC) is currently the most popular instrument for studying materials under static high pressure. It has revolutionized high-pressure research, not only because it can easily reach the pressures that exist close to the center of the earth, but also because it allows the use of various measurement methods for the study of matter under such conditions. Before the DAC was developed, high-pressure studies of materials were conducted mostly using large hydraulic presses [1]. Although such hydraulic presses commonly occupy a full room and weigh several tons, they generate maximum pressures of only a few hundred kilobars (1 kbar = 0.1 GPa). In contrast, the modern DAC fits in the palm of one's hand and gives laboratory access to very high static pressures in a relatively easy and safe manner, allowing experimental measurements to be made at pressures above 100 GPa.

The DAC was first developed by J. C. Jamieson *et al.* [2] and Weir *et al.* [3] in 1959. Figure 2.1 presents the components of the diamond anvil cell. In Fig. 2.1(a), “A” denote the

hemispherical rockers on which the diamond anvil is mounted, “B” are the diamonds and “C” represents the gasket. The force is applied by turning the screws shown in Fig. 2.1(b), pressing together the two opposing diamonds. A uniform pressure is thus continuously applied as the screw is rotated.

The principles on which all types of high-pressure cells are based are similar. A force F is applied to a small surface of area A , generating a pressure $P = F/A$, which can be increased by reducing the size of the area of contact. The anvil flat (culet) is typically set parallel to the (100) or (110) plane of the diamond. The culet is removed by grinding a flat, octagonal surface with a vertex-to-opposite-vertex distance of approximately 0.10 to 0.60 mm; diamonds are typically sized from 1/8 to 1/2 carat. The DAC used herein is 1/3 carat and the culet has a diameter of 0.50 mm.

The selection of diamonds and their sizes depends on the type of DAC and the purpose of the investigation. Diamonds are classified into two types based on their UV excited fluorescence and their IR absorption spectra. Type I diamonds contain nitrogen impurities, and Type II are relatively pure and rare in nature. Both types are subdivided into (a) and (b) subgroups. Type I (a) diamonds contain nitrogen impurities in pairs or larger aggregates, and Type I (b) diamonds contain single substitution impurities. Type II (a) are regarded as pure and Type II (b) contain boron impurities, and are commonly semiconducting. Diamonds with very low fluorescence should be adopted for light scattering studies in the DAC. Type II diamonds typically have lower fluorescence. The selected Type I diamonds have low fluorescence and are used for both Raman and photoluminescence measurements because of their plentiful supply and low cost. Type II diamonds are required for infrared absorption measurements in the range 6 to 13 μm [4,5].

In the DAC, the sample is placed between the flat faces (culets) of two brilliant-cut diamonds. The culets are separated by a thin metallic foil (gasket) which has previously been

indented by the diamonds. In the middle of the indented zone a small hole forms the pressure chamber into which the sample is placed. The sample is usually immersed in a fluid, which fills the chamber and acts as a pressure medium, maintaining hydrostatic and homogeneous conditions. The deformation and eventual fracture of the material that forms the pressure device limits the generation of very high pressures. The DAC can generate very high pressures because of the exceptional hardness of diamond, but even high-quality diamonds shatter under sufficiently high loads. The transparency of diamond over a wide range of frequencies from the near ultraviolet (~ 5.5 eV) to the infrared is the most important property, which is exploited in optical measurements.

II. Metallic Foil (Gasket)

The introduction of a metal gasket to contain the pressure medium is key to the generation of hydrostatic pressure in the DAC. Early work on the operation of DAC was conducted on solids that were pressed between a pair of diamonds without the use of a gasket. This setup provided a seriously non-hydrostatic environment for the solids. Accordingly, a gasket must be introduced into the DAC apparatus, to make it an effective tool for high-pressure research.

The metal gaskets not only prevent the damage to the diamonds but also maintain hydrostatic conditions for samples surrounded with a pressure medium. The hydrostatic state is highly desirable because a non-hydrostatic environment prevents precise control of the pressure, and makes measurements difficult to make. The gasket with a hole (~ 150 μm in diameter) in the center of the indentation zone (~ 500 μm , depending on the culet of the diamonds) is drilled using an electric discharge machine. As shown in Fig. 2.2, typical gaskets have a thickness of about 0.3 mm, reduced to approximately 0.1 mm in the indented zone. The gasket is placed on the lower diamond culet, and then samples and ruby chips are loaded

into the hole. Then, the hole is filled with pressure medium and sealed immediately by covering the upper anvil.

III. Pressure Medium

The pressure-transmitting medium markedly affects conditions within the sample chamber. Samples and ruby chips in the sample chamber must be maintained under hydrostatic conditions by the use of an appropriate pressure-transmitting medium. Ideally, the medium should remain fluid at high pressure; however, at high enough pressures, all materials solidify and develop shear strength, producing non-hydrostatic conditions. Piermarini *et al.* discovered that a mixture of four parts methanol to one part ethanol by volume is a good pressure medium for hydrostatic experiments [6]. Fluids such as 4 : 1 methanol - ethanol mixture, 16 : 3 : 1 methanol - ethanol - water, and deionized water [7] are widely used to make high-pressure measurements. Moreover, helium, nitrogen, hydrogen, argon, and xenon are excellent pressure transmitters [8-11], and are usually used in the Mbar (1 GPa \sim 10⁴ bar) range and at cryogenic temperatures. However, they require the use of cryogenic or high-pressure gas loading techniques which complicate the experimental setup.

In the experiments herein, deionized water or 4 : 1 methanol – ethanol mixture was utilized as the pressure medium. Although water is considered to be a bad pressure medium because it transforms to ice VI and VII at 0.6 and 2.1 GPa, respectively, Lin *et al.* demonstrated that the R1-R2 splitting in ruby fluorescence was maintained up to 36 GPa [7]. Therefore, deionized H₂O seems to be a suitable pressure medium for high-pressure study.

IV. Pressure Calibration

The use of the fluorescence of ruby for pressure calibration was a breakthrough in the development of the DAC. Before that time, pressure in the DAC was estimated using many

methods including directly calculating force per unit area [12], relying on the well-established freezing points of numerous liquids or the known “fixed points” of various solid-solid phase transitions [13], and, in X-ray studies, recording the lattice constant of internal markers such as NaCl or silver [14]. These methods commonly proved to be either inconvenient or inaccurate [15].

Forman *et al.* initially calibrated the shift in the R-line ruby fluorescence peaks as a function of pressure in the DAC, and demonstrated that this shift could be used as a convenient internal pressure-calibrator [15]. Ruby consists of Al_2O_3 that is doped with Cr_2O_3 , in which some of the Al^{3+} ions are replaced by Cr^{3+} . Although the full site symmetry is C_{3v} , the crystal field is dominated by its cubic component, splitting the states of the Cr^{3+} ion, forming an A-symmetric quartet ground state and a doubly degenerate first-excited state with E-symmetry, as displayed in Fig. 2.3. The combined effects of the trigonal field and spin-orbit coupling further splits the first excited into $E_{3/2}$ and $E_{1/2}$ states such that they are separated by 3.6 meV [16]. The electronic transitions $E_{1/2} \rightarrow A$ and $E_{3/2} \rightarrow A$ give rise to the R1 line at 6942 Å and the R2 line at 6928 Å. These R-lines are the active transitions in a ruby laser. Using X-ray diffraction, Barnett *et al.* [16,17] measured the unit volume of NaCl while concurrently monitoring the ruby fluorescence. They found that the R-lines shift linearly to longer wavelength as the pressure increased, and demonstrated that this linear relation holds up to 30 GPa with an accuracy of 3 %. The accepted value for the ruby R-line shift in this pressure range is 3.65 Å / GPa or $-7.53 \text{ cm}^{-1} / \text{GPa}$. Above 30 GPa, nonlinear terms in the pressure-dependence of the R-line frequencies become important. Mao and Hemley have shown that a more accurate relation [18,19] for the R1-line shift is

$$P(\text{GPa}) = \frac{A}{B} \left[\left(\frac{\Delta\lambda}{\lambda_0} + 1 \right)^B - 1 \right]. \quad (1)$$

where $A = 1904 \text{ GPa}$, $B = 7.665$, $\lambda =$ wavelength of the ruby R1 line at pressure P , and $\lambda_0 =$

wavelength of the ruby R1 line at ambient pressure. The inaccuracy of Eq. 1 is about 5 % below 1 Mbar and probably at least around 10 % above 2 Mbar. Figure 2.4 plots the R-line wavelength shift as a function of pressure. The circles represent the experimental results from the X-ray studies of Hemley *et al.* [19], the solid [20] and dashed [21] lines represent the experimental results from the X-ray studies of Mao *et al.*. The dotted line plots the results of Aleksandrov *et al.* [22]. Figure 2.5 exhibits the pressure-dependent R-lines up to 25.4 GPa at room temperature.

The ruby lines are also sensitive to temperature and shift to longer wavelength as the temperature increases, but this dependence is substantially weaker ($\frac{d\lambda}{dT} = 0.068 \text{ \AA} / ^\circ\text{C}$) than the dependence on pressure [23,24]. Hence, below 30 GPa, the linear R-line pressure scale holds well at any temperature from 300 K down to 4.2 K, with the rate of the pressure shift essentially constant over this range of temperatures. The thermal population of R2 and R1 follows Boltzmann statistics, and consequently the intensity ratio R2 to R1 declines sharply as the temperature decreases, when kT is of the order of the R2-R1 splitting. Weinstein demonstrated that this property of the intensity ratio allows the R-lines also to be used as an in-situ thermometer in the DAC with reasonable accuracy over 10 – 100 K [25].

V. Sample Preparation

The thin-film samples studied herein were all grown on semi-insulating GaAs substrates. However, the presence of thick GaAs substrate may affect the transition pressure of each thin crystal. The final conclusions and the transition pressure may include some systematic errors, because the strain is not uniform. Moreover, if GaAs remains, precisely determining the semiconductor-to-metal phase transition pressure (whether the thin crystal becomes opaque at high pressure) is rather difficult. For these reasons, before the sample was loaded into the diamond cell, the GaAs substrates had already been removed from all of the samples by

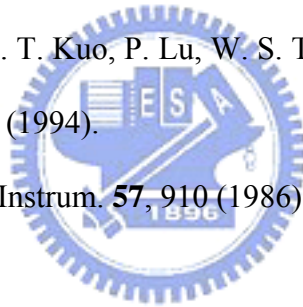
mechanical polishing and then were chemically etched using $\text{H}_2\text{O} : \text{H}_2\text{O}_2 : \text{NaOH} = 30 \text{ ml} : 21 \text{ ml} : 4 \text{ g}$. Therefore, the intense Raman singlets from GaAs at 267 and 292 cm^{-1} for TO and LO, respectively, were absent.



References

- [1] H. G. Drickamer and A. S. Balchan, in *Modern Very High Pressure Techniques*, edited by R. H. Wentorf, Jr. (Butterworths, Washington, DC, 1962), p. 25.H.
G. Drichamer, Rev. Sci. Instrum. **32**, 212 (1961).
- [2] J. C. Jamieson, A. W. Lawson, and N. D. Nachtrieb, Rev. Sci. Instrum. **30**, 1016 (1959).
- [3] C. E. Weir, E. R. Lippincott, A. van Valkenburg, and E. N. Bunting, J. Res. Natl. Bur. Stand., Sect. A **63**, 55 (1959).
- [4] C. D. Clark, in *Physical Properties of Diamond*, edited by R. Berman (Clarendon, Oxford, 1965) p. 295; G. Davies, in *Chemistry and Physics of Carbon*, edited by P. W. Phillips and P. A. Turner (Dekker, New York, 1977). Vol. **13**, p. 10.
- [5] R. J. Wijngaaden and I. F. Silvera, in *High Pressure Science and Technology*, edited by B. Vodar and P. H. Martean (pergamon, Oxford), **1**, 157 (1980).
- [6] G. J. Piermarini, S. Block, and J. D. Barnett, J. Appl. Phys. **44**, 5377 (1973).
- [7] C. M. Lin, D. S. Chuu, T. J. Yang, W. C. Chou, J. Xu, and E. Huang, Phys. Rev. B **55**, 13641 (1997).
- [8] P. M. Bell and H. K. Mao, in Carnegie Institution of Washington Year Book **80**, 404 (1981).
- [9] H. K. Mao and P. M. Bell, in Carnegie Institution of Washington Year Book **78**, 663 (1979).
- [10] K. Asami and A. L. Ruoff, report #5531, Mater. Sci. Center, Cornell University
- [11] H. K. Mao, J. Xu, and P. M. Bell, J. Geophys. Res. Jamieson Volume (1980).
- [12] S. Block, C. E. Weir, G. J. Piermarini, Science **169**, 586 (1970).
- [13] H. G. Drickamer, Rev. Sci. Instrum. **41**, 1667 (1970).
- [14] W. A. Bassett, T. Takahashi, H. K. Mao, J. Appl. Phys. **39**, 319 (1968).
- [15] R. A. Forman, G. J. Piermarini, J. D. Barnett, and S. Block, Science **176**, 284 (1972).

- [16] J. D. Barnett, S. Block, and G. J. Piermarini, *Rev. Sci. Instrum.* **44**, 1 (1973).
- [17] G. J. Piermarini, S. Block, J. D. Barnett, and R. A. Forman, *J. Appl. Phys.* **46**, 2774 (1975).
- [18] H. K. Mao, J. Xu, and P. M. Bell, *Journal of Geophysics Research*, **91**, 4620 (1986).
- [19] R. J. Hemley, C. S. Zha, A. P. Jephcoat, H. K. Mao, L. W. Finger, and D. E. Cox, *Phys. Rev. B* **39**, 11820 (1989).
- [20] H. K. Mao, P. M. Bell, J. W. Shaner, and D. J. Steinberg, *J. Appl. Phys.* **49**, 3276 (1978).
- [21] H. K. Mao, J. A. Xu, and P. M. Bell, *Journal of Geophysics Research*, **91**, 4673 (1986).
- [22] I. V. Aleksandrov, A. F. Goncharov, A. N. Zisman, and S. M. Stishov, *Zh. Eksp. Teor. Fiz.* **93**, 680 (1987) [*Sov. Phys. JETP* **66**, 384 (1987)].
- [23] D. M. Adams, R. Appleby, and S. K. Sharma, *J. Phys. E* **9**, 1140 (1976).
- [24] T. H. Huang, C. C. Hsu, C. T. Kuo, P. Lu, W. S. Tse, D. P. Wang, T. C. Chou, and A. Y. G. Fuh, *J. Appl. Phys.* **75**, 3599 (1994).
- [25] B. A. Weinstein, *Rev. Sci. Instrum.* **57**, 910 (1986).



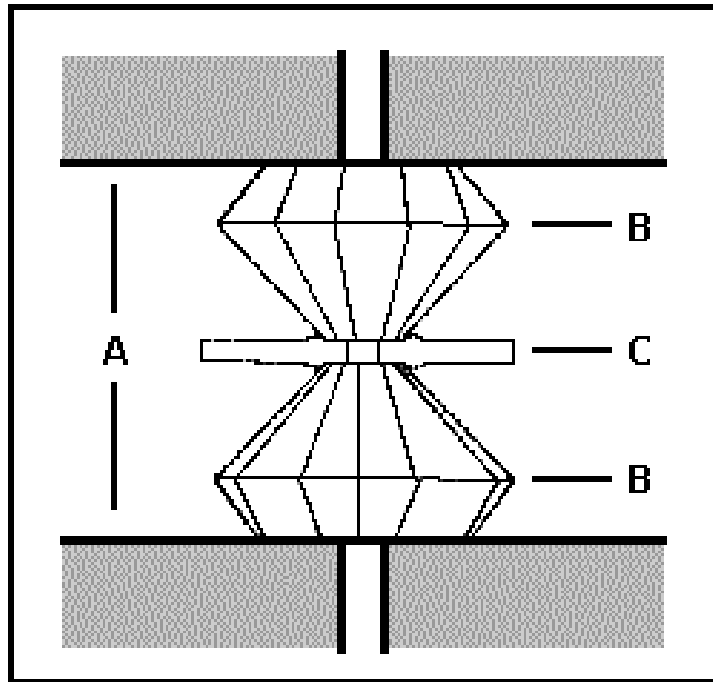


FIG. 2.1. (a) Schematic depiction of diamond anvil cell (DAC).

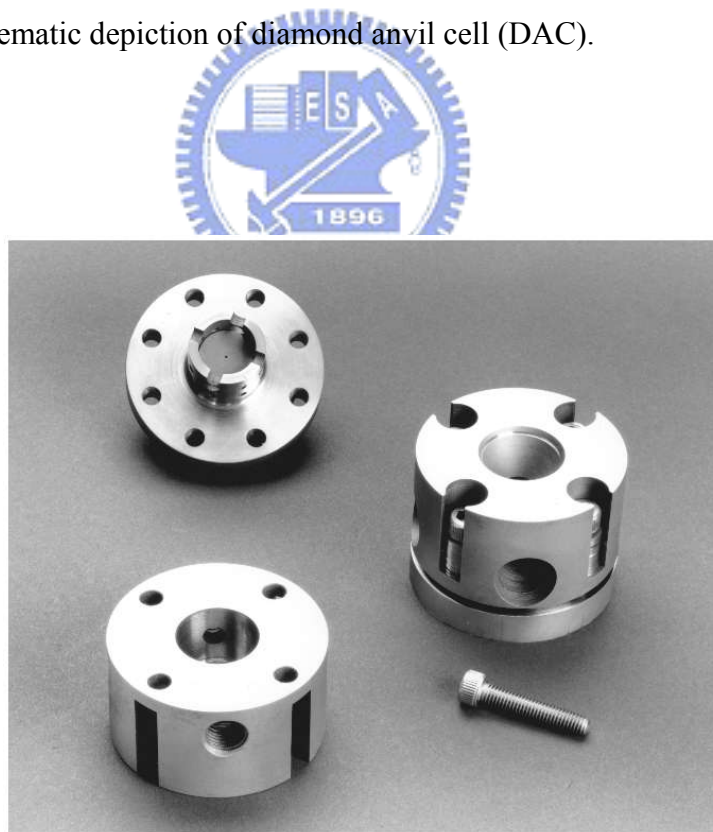


FIG. 2.1. (b) Diamond anvil cell as used in this thesis.

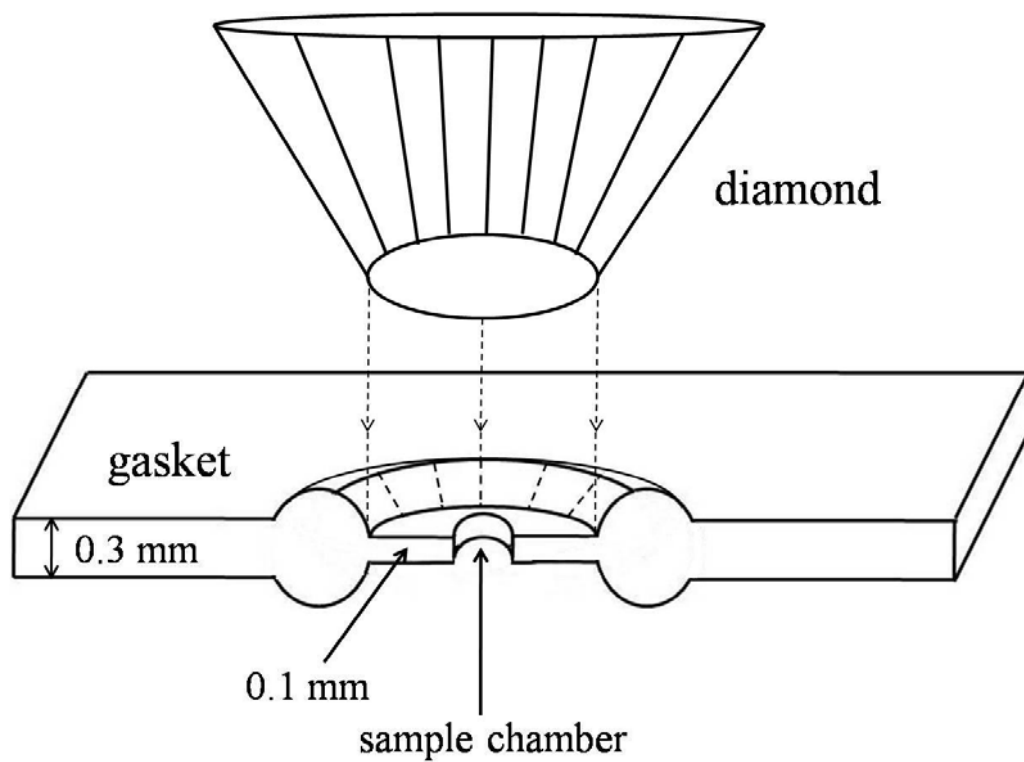


FIG. 2.2. Section of gasket indentation area and the sample chamber.

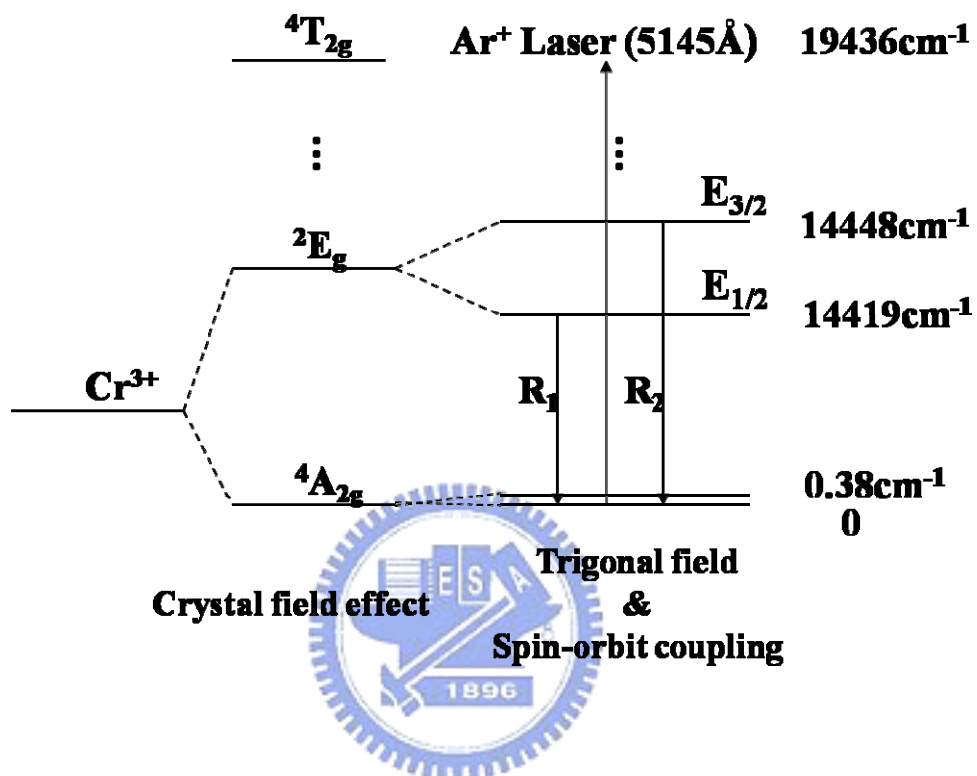


FIG. 2.3. Energy levels of Cr^{3+} in Al_2O_3 . The transitions $E_{1/2} \rightarrow A$ and $E_{3/2} \rightarrow A$ yield R1 and R2 lines, respectively.

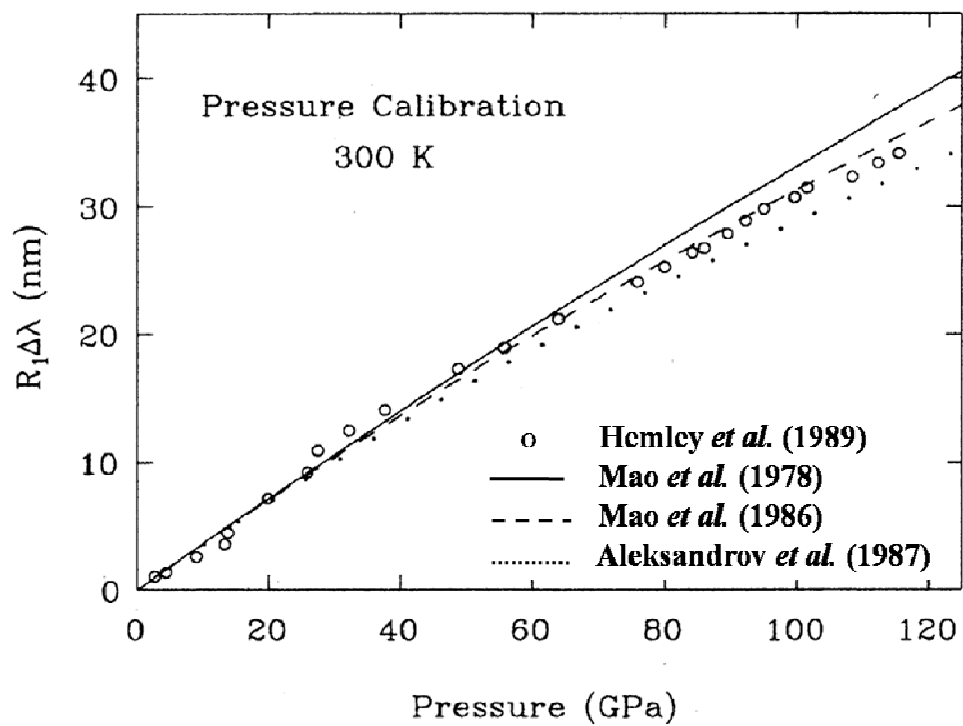


FIG. 2.4. Wavelength of ruby fluorescence against pressure. [Ref. 19]

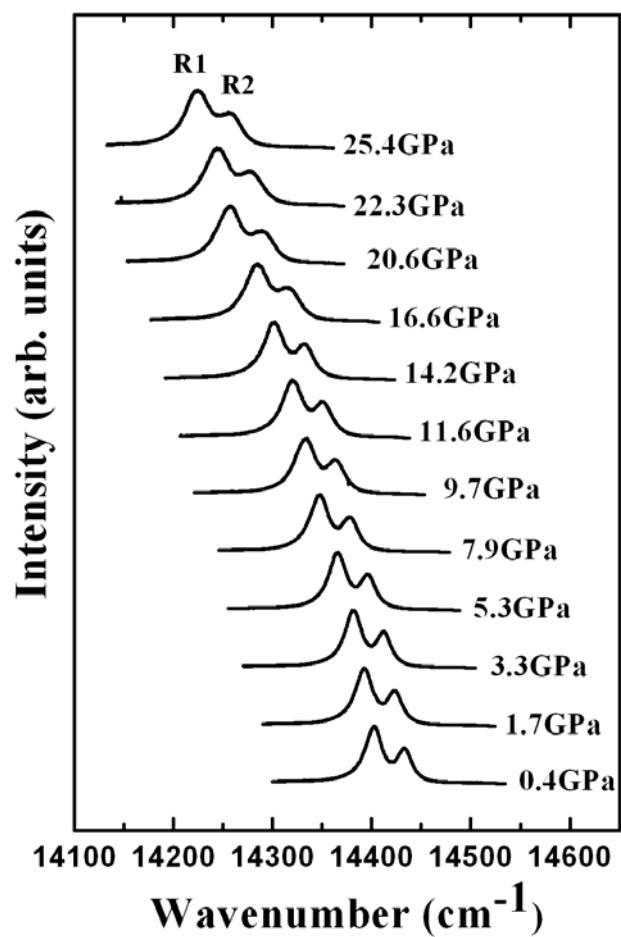


FIG. 2.5. Pressure-dependent ruby fluorescence spectra at room temperature.

2.2 Optical Spectroscopy

I. Introduction to Raman Scattering

All of the Raman parameters, such as frequencies, peak intensity, lineshape, linewidth, and polarization behavior, can be applied to characterize the lattice, impurities and free carriers in semiconductors. Intensity yields information about crystallinity. Raman phonon frequencies can reveal the composition of elements in a ternary material. The linewidth increases when a material is damaged or disordered because of phonon damping or changes to the selection rules.

Raman scattering is the interaction of the incident light with optical phonons. When the polarization of a phonon is transverse (longitudinal) relative to the wavevector of incident light, it is described as being in the TO (LO) mode. In terms of the corpuscular theory of light, Rayleigh scattering corresponds to an elastic collision process between the phonon and the crystal, whereas Raman scattering corresponds to an inelastic collision in which the phonon either loses one or more quanta (Stokes shifts) or acquires one or more quanta (anti-Stokes shifts). Figure 2.6 plots the transition associated with Rayleigh scattering, first-order Stokes scattering, and anti-Stokes scattering. As shown in Fig. 2.6, ν_i (K_i) is the frequency (wavevector) of incident photon, ν_s (K_s) is the frequency (wavevector) of the scattered phonon, and ν_o (K_o) represents the frequency (wavevector) of the optical phonon that is involved in the scattering process. Energy and momentum are conserved between the initial and final states of the system. The conservation conditions are

$$h\nu_s = h\nu_i \pm h\nu_o \quad (2)$$

$$K_s = K_i \pm K_o \quad (3)$$

where the plus sign refers to an anti-Stokes shift and the minus sign stands for Stokes shift. However, the conditions for Rayleigh scattering are $\nu_i = \nu_s$ and $K_i = K_s$. Generally, the intensity of the anti-Stokes modes is much weaker than that of the Stokes components.

Raman scattering is inherently a weak process, but lasers provide sufficient power to enable the spectra to be routinely measured.

II. Micro-Raman and Micro-PL Systems

Figure 2.7 depicts the experimental setup of the micro-Raman (PL) measurements which were made using a Jobin-Yvon microscope system. Raman and PL spectra were obtained at room temperature and collected in the backscattering configuration using 514.5 or 488.0 nm lines of an Ar⁺-ion laser as the excitation source. An incident beam from an argon-ion laser was focused to about 5 μm in diameter on the sample using a 20x long-working-distance (~ 20 mm) microscope objective.

To eliminate Rayleigh scattering, a 514.5 or 488.0 nm holographic super notch plus filter was used to filter it out of the laser. The spectra were analyzed using a SPEX 1404 double grating 0.85 m spectrometer that was equipped with a multichannel LN₂-cooled charge-coupled device (CCD). The spectrometer was controlled using a computer, which was used to store and plot the collected data.

III. Time-Resolved PL System

Figure 2.8 presents the experimental setup of the time-resolved PL (TRPL) system. The 300 ps GaN pulsed laser diode (405 nm / 2.5 MHz) and a 200 fs mode-locked Ti:sapphire laser (400 nm / 76 MHz) were used as an excitation source. The laser light is focused on the sample by a convex lens (L1). The combination lenses (L2 and L3) guide the luminescence into the spectrometer. The signal is dispersed using a SPEX 1403 double-grating 0.85 m spectrometer and detected using a high-speed photomultiplier tube. The signal is further analyzed by a computer with a plug-in time-correlated counting card.

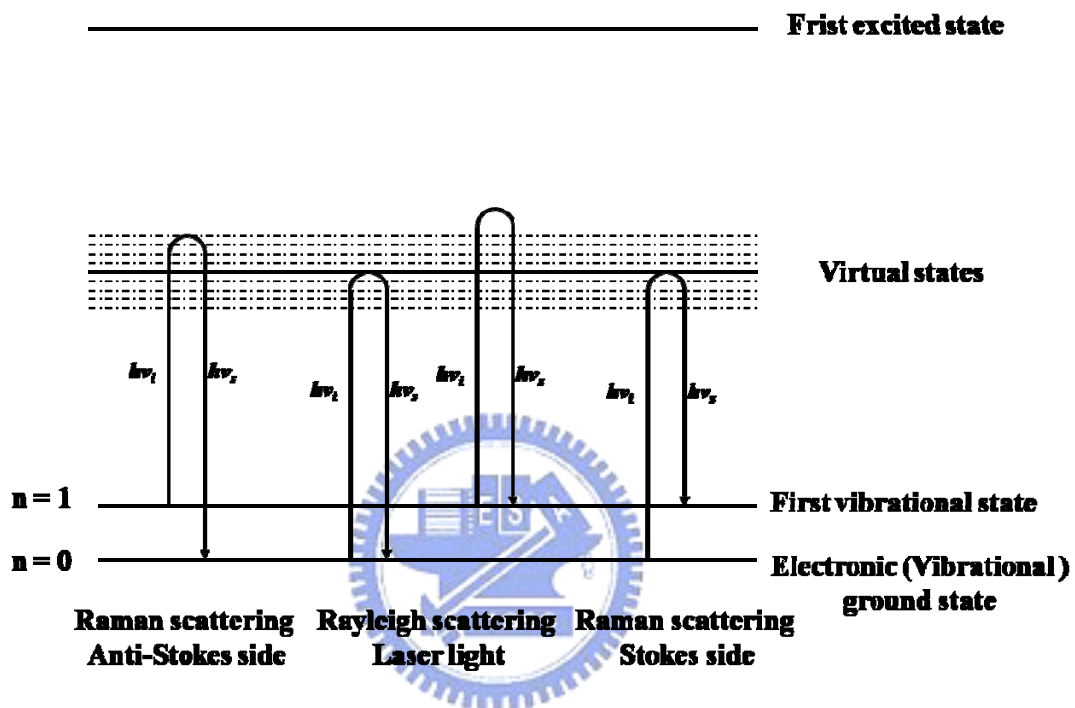


FIG. 2.6. Schematic scattering of light.

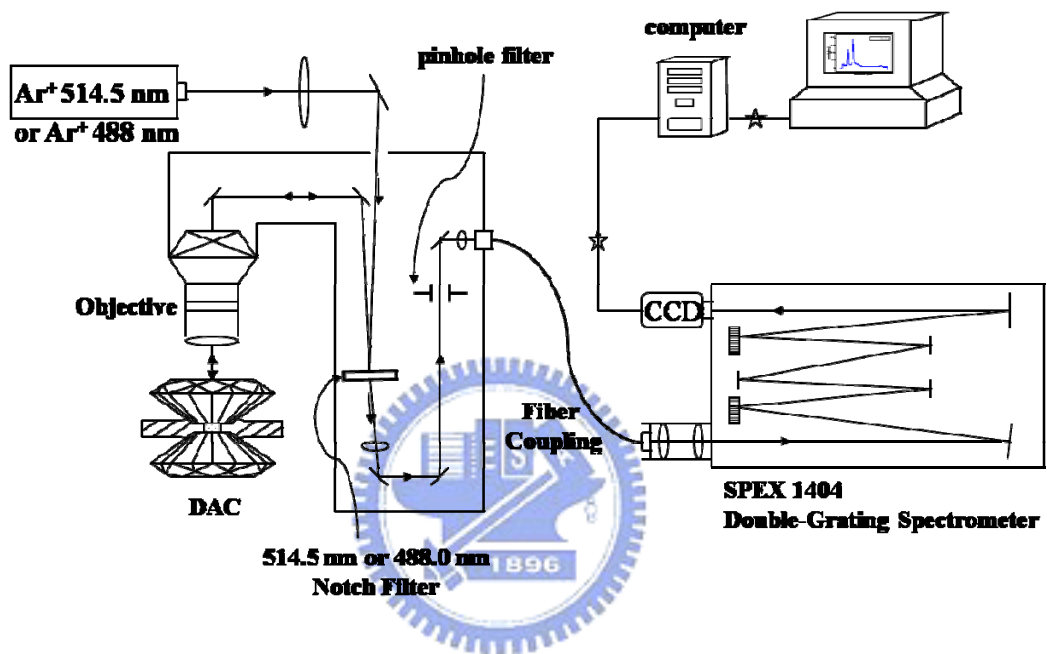


FIG. 2.7. Experimental setup of micro-Raman (PL) system.

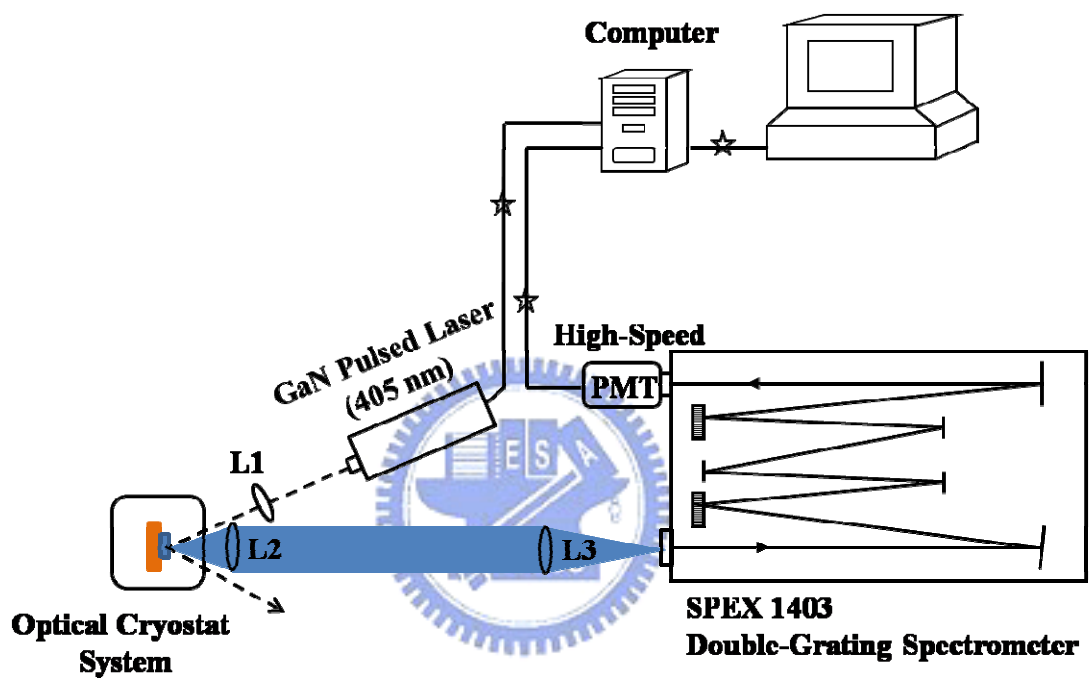
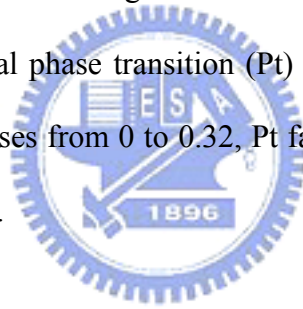


FIG. 2.8. Experimental setup of time-resolved PL system.

Chapter 3 Pressure-Dependent Raman Scattering and Photoluminescence of $\text{Zn}_{1-x}\text{Cd}_x\text{Se}$

This chapter discusses Raman and photoluminescence of cubic $\text{Zn}_{1-x}\text{Cd}_x\text{Se}$ ($0 \leq x \leq 0.32$) epilayers at high pressure. The impurity mode *I* observed in the phonon Raman spectra at low temperature confirms the intermediate phonon mode behavior. A split transverse optical phonon mode was found in the down-stroke high-pressure Raman scattering. Additionally, the pressure-dependent longitudinal optical phonon frequencies and the Grüneisen parameter were obtained by quadratic polynomial fitting. Pressure-driven resonant Raman scattering effect was observed in samples with a high Cd concentration ($x \geq 0.18$). The pressure at the onset of semiconductor-to-metal phase transition (Pt) decreases as the Cd content increases. As the Cd concentration increases from 0 to 0.32, Pt falls from 13.6 to 9.4 GPa, according to $\text{Pt (GPa)} = 13.6 - 6.8x - 20.3x^2$.



I. Introduction

Wide-band-gap II-VI ternary compound semiconductor, $\text{Zn}_{1-x}\text{Cd}_x\text{Se}$, has attracted much attention because its tunable band gap covers the visible spectrum. The physical properties of $\text{Zn}_{1-x}\text{Cd}_x\text{Se}$ have been extensively studied over the last decade because the material is extensively employed as an active layer in ZnSe-based laser diodes [1-4]. The crystal structure of bulk $\text{Zn}_{1-x}\text{Cd}_x\text{Se}$ is zincblende (ZB) for $x < 0.3$, wurtzite for $x > 0.7$, and is a mixture of both for $0.3 \leq x \leq 0.7$ [Ref. 5 and 6]. A single-phase ZB crystalline structure over the entire Cd composition range from ZnSe to CdSe [6-8] can be grown on (001) GaAs substrates by molecular beam epitaxy (MBE). Furthermore, the energy-dispersive X-ray diffraction (EDXD) and Raman scattering of ZnSe-based II-VI ternary compounds

[9-12] were investigated at high pressure to study the phase transformations. However, the pressure-induced phase transition and the crystal stability of ZB $\text{Zn}_{1-x}\text{Cd}_x\text{Se}$ epilayers under hydrostatic pressure still remain unexplored. The phase transitions from semiconductor to metal and the ZB (B_3 phase) to rocksalt (RS), (B_1 phase), were found to be consistent with the disappearance of the LO phonon from the Raman spectra [10-13].

This work discusses the phonon Raman and photoluminescence (PL) spectra of ZB $\text{Zn}_{1-x}\text{Cd}_x\text{Se}$ epilayers ($x = 0, 0.06, 0.11, 0.18, 0.25,$ and 0.32) at room temperature and high pressures. The optical phonon mode behavior, pressure-dependent LO phonon frequencies, LO phonon line broadening, the splitting of the TO mode in the down-stroke pressurized process and the Grüneisen parameter (γ_{LO}) of $\text{Zn}_{1-x}\text{Cd}_x\text{Se}$ epilayers were determined. Moreover, samples with a high ($x \geq 0.18$) Cd content exhibit pressure-driven resonant Raman scattering (RRS) enhancement. Additionally, the pressure at the onset of semiconductor-to-metal phase (Pt) transition was plotted as a function of Cd content (x).



II. Experiment

The $\text{Zn}_{1-x}\text{Cd}_x\text{Se}$ epilayers ($x = 0, 0.06, 0.11, 0.18, 0.25$ and 0.32) were grown on semi-insulating GaAs (001) substrates with a Veeco Applied EPI 620 MBE system using Zn (6N purity), Se (6N purity) and Cd (6N purity) solid sources. The substrate temperature was maintained at $300\text{ }^\circ\text{C}$, and the thickness of the $\text{Zn}_{1-x}\text{Cd}_x\text{Se}$ epilayers was fixed at around $0.5\text{ }\mu\text{m}$. The Cd content was determined by energy-dispersive X-ray (EDX) analysis.

High-pressure measurements were taken in a gasket diamond anvil cell (DAC). The culets of the diamond anvils are $500\text{ }\mu\text{m}$ in diameter. The sample chamber was a circular hole with a diameter of about $170\text{ }\mu\text{m}$, which was predrilled on the stainless steel gasket using an electrical discharge machine. A methanol-ethanol 4:1 mixed liquid was used as a pressure-transmitting medium in order to maintain the hydrostatic conditions. The hydrostatic

pressure was determined by the spectral shift of the ruby R1 line, which is widely used in high-pressure Raman and PL measurements [14,15]. The pressure gradient was less than 0.5 GPa, as determined by measurements made at various positions of the sample chamber. Before the $Zn_{1-x}Cd_xSe$ sample was loaded into the DAC, the GaAs substrate was removed by mechanical polishing and chemical etching with $H_2O : H_2O_2 : NaOH = 30 \text{ ml} : 21 \text{ ml} : 4 \text{ g}$.

Raman and PL spectra were performed at room temperature and collected in backscattering configuration using a 514.5 nm line of an Ar^+ -ion laser as the excitation source. The spectra were analyzed by a SPEX 1404 double grating spectrometer equipped with a multichannel LN_2 -cooled charge-coupled device (CCD). The 514.5 nm holographic notch filter was used to filter out the Rayleigh scattering.

III. Results and Discussion

Figure 3.1 presents the first-order Raman spectra of $Zn_{1-x}Cd_xSe$ ($x = 0, 0.06, 0.11, 0.18, 0.25, \text{ and } 0.32$) epilayers. The spectra were all obtained at room temperature and ambient pressure under $z(x+y, x+y)\bar{z}$ backscattering geometry. The Raman selection rule for this geometry forbids the TO and allows the emission of LO only. However, a weak TO feature which appears at 205.4, 203.3, and 201.6 cm^{-1} for $x = 0, 0.06, \text{ and } 0.11$ samples, respectively, can be attributed to a slight deviation from perfect backscattering geometry. Table 3.1 presents the LO and TO phonon frequencies and the linewidth of the LO phonons of all $Zn_{1-x}Cd_xSe$ samples. As the Cd content increases, the LO and TO phonon frequency decreases. Asymmetric broadening of the peaks of the LO phonon at high Cd content ($x \geq 0.18$) is observed, attributed primarily to the disorder of the alloy [16], and becomes more evident under pressure. Figure 3.2 shows the dependence of LO phonon frequencies and the full width at half maximum (FWHM) on the Cd concentration (x), respectively. The LO phonon frequency falls as x increases, and is accompanied by an increase in FWHM.

The zone-center optical phonon mode of ZB $\text{Zn}_{1-x}\text{Cd}_x\text{Se}$ was controversial in previous studies. Alonso *et al.* [17], Avendaño-López *et al.* [5], and Camacho *et al.* [18] found that in addition to the LO and TO phonon modes, an impurity mode I was present, and could be attributed to the impurity modes of Zn in CdSe for x close to 1 and to that of Cd in ZnSe for x close to 0. Therefore, they concluded that $\text{Zn}_x\text{Cd}_{1-x}\text{Se}$ exhibited mixed-mode behavior. However, Meredith *et al.* [16] and Li *et al.* [19] indicated that $\text{Zn}_x\text{Cd}_{1-x}\text{Se}$ exhibited single mode behavior because they observed no impurity mode and their experimental results were consistent with the mass criterion of one mode behavior [16]. Although at room temperature, only LO and TO phonons of $\text{Zn}_{1-x}\text{Cd}_x\text{Se}$ ($x = 0$ to 0.32) are observed in the Raman spectra, as shown in Fig. 3.1. However, the low-temperature Raman scattering measurements exhibit the impurity mode I (Fig. 3.3). In particular, at $x \geq 0.25$, under the RRS condition, the impurity mode I is clearly present. Moreover, the frequency of the I phonon falls as the Cd content increases, supporting the results given in Ref. 17. Accordingly, the vibration mode of $\text{Zn}_{1-x}\text{Cd}_x\text{Se}$ is an intermediate.

Figure 3.4 presents the up-stroke pressure-dependent Raman spectra of $\text{Zn}_{1-x}\text{Cd}_x\text{Se}$ epilayer ($x = 0.06$) at room temperature. A strong LO phonon and a weak TO feature are observed at ambient pressure, while the TO phonon becomes more intense as the pressure increases. The $x = 0$ and 0.11 samples exhibit the same behavior because the sample chips deviate from the perfect backscattering geometry when the samples are pressured in the diamond cell. The applied pressure reduces the lattice constant and the crystal volume. Therefore, the frequencies of the LO and TO phonons shift to higher frequencies, accompanied with decreasing in intensity. The LO phonon disappears and the sample becomes opaque at approximately 13.0 GPa. These facts are evidences of the phase transition from the semiconductor to the metal phase. However, a TO phonon is still observed in the Raman spectra when the semiconductor becomes metallic. It can be ascribed to the fact that

transverse surface lattice vibrations are allowed in both semiconductor and metal, even if the skin depth (or penetration depth) of the metal into which the laser penetrates is merely several tens of angstroms [10,11]. Similar experimental results were obtained from our samples with low Cd content ($x \leq 0.18$) and in earlier investigations of nonmagnetic and magnetic II-VI ternary compounds, ZnFeSe [10], ZnSeTe [11], and ZnMnSe [12] crystals.

In our previous investigations, the TO phonon splitting occurred in the up-stroke pressure process and was attributed to the pressure-induced formation of an additional phase. Despite numerous careful search; however, no TO splitting observed in any of the studied $\text{Zn}_{1-x}\text{Cd}_x\text{Se}$ samples during the up-stroke process, which were examined several times by reloading them and changing the pressure medium to de-ionized (DI) water. Nevertheless, in the down-stroke process of $\text{Zn}_{0.94}\text{Cd}_{0.06}\text{Se}$, shown in Fig. 3.5, a split TO phonon mode begins to develop as the pressure is reduced to around 11.5 GPa. It becomes more pronounced at 8.3 GPa. The split TO phonon mode is slightly blueshifted and its intensity falls as the pressure is released. The splitting of the TO mode in the down-stroke process also implies the formation of an additional high-pressure phase. Recent EDXD experiments by Pellicer-Porres *et al.* [20,21] demonstrated that ZnSe and $\text{ZnSe}_x\text{Te}_{1-x}$ exhibited a cinnabar structure between the ZB and RS structures, becoming apparent only in the down-stroke process. Côté *et al.* [22] also theoretically calculated the existence of a fourfold-coordinated cinnabar phase between ZB and RS phases, which could be found in the down-stroke process. Accordingly, this work presents the observation of a cinnabar phase in $\text{Zn}_{1-x}\text{Cd}_x\text{Se}$ by Raman scattering in the down-stroke process.

Table 3.2 lists the pressure-dependent LO phonon frequencies obtained by fitting a quadratic polynomial equation to our measurements,

$$\omega_{\text{LO}} = \omega_0 + ap + bp^2, \quad (1)$$

where ω_0 is the LO phonon frequency at ambient pressure, p is the pressure in gigapascal, and

a and b are the vibrational pressure coefficients for this mode. The pressure dependence of a mode frequency ω_{LO} can be defined in terms of the dimensionless Grüneisen parameter (γ_{LO}), which is given by [23]

$$\gamma_{\text{LO}} = - \left(\frac{d \ln \omega_{\text{LO}}}{d \ln V} \right) = \frac{1}{\beta} \frac{\partial \ln \omega_{\text{LO}}}{\partial p} = \left(\frac{K_0}{\omega_{\text{LO}}} \right) \left(\frac{d \omega_{\text{LO}}}{dp} \right), \quad (2)$$

where K_0 is the bulk modulus, defined as the inverse of the isothermal volume compressibility (β), and V is the molar volume in cm^3/mol . Since the bulk modulus (K_0) of $\text{Zn}_{1-x}\text{Cd}_x\text{Se}$ is unknown, $K_0(\text{ZnSe}) = 62.4 \text{ GPa}$ is used [24]. Table 3.2 presents the γ_{LO} values of all samples at ambient pressure. $d\omega/dp = 3.31 \text{ cm}^{-1}/\text{GPa}$, and $\gamma_{\text{LO}} = 0.82$ and $d\omega/dp = 4.53 \text{ cm}^{-1}/\text{GPa}$, and $\gamma_{\text{LO}} = 1.18$ are obtained for ZnSe and $\text{Zn}_{1-x}\text{Cd}_x\text{Se}$ ($x = 0.32$), respectively. Camacho *et al.* [18] noted that no pressure-dependent Raman results for bulk CdSe or epilayer had been published. However, Alivisatos *et al.* [25] found $d\omega/dp = 4.30 \text{ cm}^{-1}/\text{GPa}$ and $\gamma_{\text{LO}} = 1.1$ for ZB-phase CdSe nanocrystals. The ionization of the lattice can be deduced from γ_{LO} [26], and the ionicity (f_i) of CdSe (0.70) is larger than that of ZnSe (0.63) [Ref. 27]. By contrast, higher Cd concentration samples exhibit larger lattice ionization and higher pressure variation on the phonon frequency. In Table 3.2, we can see that the applied pressure tends to reduce the variation of phonon frequency and the lattice ionization due to the second negative term of $d\omega/dp$.

Figure 3.6 shows the pressure-dependent Raman spectra of $\text{Zn}_{1-x}\text{Cd}_x\text{Se}$ epilayer ($x = 0.25$) at room temperature. The TO phonon is not found and the intensity of LO phonons does not monotonously decline as the pressure increases. Samples with a high Cd content ($x = 0.18$, and 0.32) exhibit a similar trend, because of the pressure-driven RRS effect, which occurs when the incident laser energy is sufficiently close to the energy of the electronic excitations, described as

$$h\nu_{\text{laser}} - mh\nu_{\text{LO}}(x, p) \approx E_{\text{exc}}(x, p), \quad (3)$$

where $h\nu_{\text{laser}}$ is the photon energy of the incident laser (2.41 eV). $E_{\text{exc}}(x, p)$ and $h\nu_{\text{LO}}(x, p)$ are the electronic transition energy and the LO phonon energy, respectively, as functions of Cd content (x) and applied pressure (p). The m denotes the overtone order of LO phonons. The exciton energy of $\text{Zn}_{1-x}\text{Cd}_x\text{Se}$ was controlled by tuning the Cd concentration during the growth, or by manipulating the pressure and temperature of the sample chamber. In this investigation, $h\nu_{\text{laser}}$ was fixed at 2.41 eV and the exciton energy increased with pressure. As the external pressure was gradually tuned toward 6.6 GPa, the exciton energy approached the laser energy and an increase in intensity of LO phonon was observed. By further increasing the pressure, the exciton energy exceeds the incident laser energy (at around 7.5 GPa in Fig. 3.6) and begins to move away from the RRS condition, and the intensity of LO phonon decreases monotonously as the pressure increases. At around 11.0 GPa, the LO phonon disappears, revealing the phase transformation from the semiconductor to the metal phase.

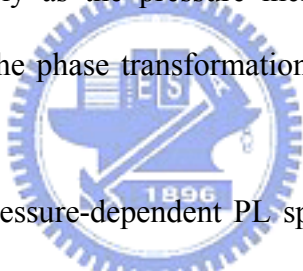


Figure 3.7 displays the pressure-dependent PL spectra of the $\text{Zn}_{1-x}\text{Cd}_x\text{Se}$ epilayer ($x = 0.25$) at 300 K. At 0.2 GPa, the broad peak at 2.08 eV is attributed to the near band edge (NBE) emission. As the pressure is increased to 2.2 GPa, the NBE emission shifts to higher energy. Further increasing the pressure causes the NBE emission to overlap the LO phonon peaks. The intensity of the LO phonon peaks of the Stokes side increases and the RRS effect occurs. The inset in Fig. 3.7 plots the peak energies of the room-temperature PL spectra before the phase transition as a function of pressure. The PL spectra were excited using an Ar^+ 488 nm laser line (2.54 eV) to observe the NBE emission above the 2.41 eV energy of the Ar^+ 514.5 nm laser line, which was used to excite phonon Raman scattering. As the pressure further increases to above 6.6 GPa, far from the RRS condition, the intensity of the 1LO phonon decreases abruptly and the PL spectra disappears because the NBE energy exceeds the excitation laser energy. When the pressure reaches the value for the phase transition (11.0

GPa), the LO phonons at both sides of Raman spectra disappears. This result is a strong evidence of the semiconductor-to-metal phase transition. The phase transition pressure of this sample, at which the LO phonon disappeared, was also verified using a 632.8 nm ruby laser as an excitation source, this wavelength is far from the RRS effect.

The pressures at the onset of semiconductor-to-metal phase transition of all $\text{Zn}_{1-x}\text{Cd}_x\text{Se}$ epilayers discussed herein are listed in Table 3.2. As the Cd concentration increases to 0.32, the phase transition pressure falls from 13.6 to 9.4 GPa. Figure 3.8 plots the decline in the phase transition pressure as a function of x . The solid line represents a quadratic fit, given by $P_t \text{ (GPa)} = 13.6 - 6.8x - 20.3x^2$. The fall of P_t with x suggests a reduction in structural stability. The structure becomes destabilized as the substituted element content increases; in addition, this relationship has been observed in other ZnSe-based ternary semiconductors. For instance, Yang *et al.* found that for $\text{ZnSe}_{1-x}\text{Te}_x$ epilayers with x up to 0.54, the pressure at the onset of semiconductor-to-metal phase transition decreased from 13.7 to 7.3 GPa. For $\text{Zn}_{1-x}\text{Mn}_x\text{Se}$ crystals, the structural transition from zincblende (B_3) to rocksalt (B_1) occurred at about 11.8 and 9.9 GPa for $x = 0.07$ and 0.24, respectively [11,12].

IV. Conclusions

The pressure-dependent Raman and PL spectra of $\text{Zn}_{1-x}\text{Cd}_x\text{Se}$ epilayers ($0 \leq x \leq 0.32$) were investigated. Low-temperature experiments reveal that the optical phonons of $\text{Zn}_{1-x}\text{Cd}_x\text{Se}$ exhibit intrinsic intermediate-mode behavior. The splitting of the TO mode in the down-stroke pressurized process may have been caused by the formation of an additional high-pressure phase. The pressure-dependent LO phonon frequencies are fitted with a quadratic polynomial equation and the Grüneisen parameters are obtained. The pressure-driven RRS effect was observed in samples with a high Cd concentration ($x \geq 0.18$). Both the Stokes and anti-Stokes sides of the LO phonons disappear as the crystal phase

changes from semiconductor-to-metal phase. The pressure at the onset of semiconductor-to-metal phase transition is found to decrease as the Cd content increases.



References

- [1] M. A. Haase, J. Qiu, J. M. Depuydt, and H. Cheng, *Appl. Phys. Lett.* **59**, 1272 (1991).
- [2] J. Ding, H. Jeon, T. Ishihara, M. Hagerott, A. V. Nurmikko, H. Luo, N. Samarth, and J. K. Furdyna, *Phys. Rev. Lett.* **69**, 1707 (1992).
- [3] W. Faschinger and J. Nürnberger, *Appl. Phys. Lett.* **77**, 187 (2000).
- [4] S. -B. Che, I. Nomura, A. Kikuchi, and K. Kishino, *Appl. Phys. Lett.* **81**, 972 (2002).
- [5] J. Avendaño-López, F. L. Castillo-Alvarado, A. Escamilla-Esquivel, G. Contreras-Puente, J. Ortiz-López, and O. Zelaya-Angel, *Solid State Commun.* **100**, 33 (1996).
- [6] U. Lunz, J. Kuhn, F. Goschenhofer, U. Schüssler, S. Einfeldt, C. R. Becker, and G. Landwehr, *J. Appl. Phys.* **80**, 6861 (1996).
- [7] N. Samarth, H. Luo, J. K. Furdyna, R. G. Alonso, Y. R. Lee, A. K. Ramdas, S. B. Qadri, and N. Otsuka, *Appl. Phys. Lett.* **56**, 1163 (1990).
- [8] S. Fujita, Y. Wu, Y. Kawakami, and S. Fujita, *J. Appl. Phys.* **72**, 5233 (1992).
- [9] S. B. Qadri, E. F. Skelton, A. W. Webb, N. Moulton, J. Z. Hu, and J. K. Furdyna, *Phys. Rev. B* **45**, 5670 (1992).
- [10] C. M. Lin, D. S. Chuu, T. J. Yang, W. C. Chou, J. Xu, and E. Huang, *Phys. Rev. B* **55**, 13641 (1997).
- [11] C. S. Yang, W. C. Chou, D. M. Chen, C. S. Ro, J. L. Shen, and T. R. Yang, *Phys. Rev. B* **59**, 8128 (1999).
- [12] C. S. Yang, C. S. Ro, W. C. Chou, C. M. Lin, D. S. Chuu, J. Hu, E. Huang, and J. Xu, *J. Appl. Phys.* **85**, 8092 (1999).
- [13] A. K. Arora and T. Sakuntala, *Phys. Rev. B* **52**, 11052 (1995).
- [14] G. J. Piermarini, S. Block, J. D. Barnett, and R. A. Forman, *J. Appl. Phys.* **46**, 2774 (1975).
- [15] H. K. Mao, P. M. Bell, J. W. Shaner, and D. J. Steinberg, *J. Appl. Phys.* **49**, 3276 (1978).

- [16] W. Meredith, G. Horsburgh, G. D. Brownlie, K. A. Prior, B. C. Cavenett, W. Rothwell, and A. J. Dann, *J. Cryst. Growth* **159**, 103 (1996).
- [17] R. G. Alonso, E. -K. Suh, A. K. Ramdas, N. Samarth, H. Luo, and J. K. Furdyna, *Phys. Rev. B* **40**, 3720 (1989).
- [18] J. Camacho, I. Loa, A. Cantarero, K. Syassen, I. Hernández-Calderón, and L. González, *Phys. Status Solidi B* **235**, 432 (2003).
- [19] W. S. Li, Z. X. Shen, D. Z. Shen, and X. W. Fan, *J. Appl. Phys.* **84**, 5198 (1998).
- [20] J. Pellicer-Porres, A. Segura, V. Muñoz, J. Zúñiga, J. P. Itié, A. Polian, and P. Munsch, *Phys. Rev. B* **65**, 012109 (2001).
- [21] J. Pellicer-Porres, D. Martínez-García, Ch. Ferrer-Roca, A. Segura, V. Muñoz-Sanjosé, J. P. Itié, A. Polian, and P. Munsch, *Phys. Rev. B* **71**, 035210 (2005).
- [22] M. Côté, O. Zakharov, A. Rubio, and M. L. Cohen, *Phys. Rev. B* **55**, 13025 (1997).
- [23] M. Blackman and W. B. Daniels, *Light Scattering in Solids IV*, edited by M. Cardona and G. Güntherodt (Springer, Berlin, 1984), Chap. 8.
- [24] S. Ves, K. Strössner, N. E. Christensen, C. K. Kim, and M. Cardona, *Solid State Commun.* **56**, 479 (1985).
- [25] A. P. Alivisatos, T. D. Harris, L. E. Brus, and A. Jayaraman, *J. Chem. Phys.* **89**, 5979 (1988).
- [26] R. W. Meulenberg and G. F. Strouse, *Phys. Rev. B* **66**, 035317 (2002).
- [27] J. C. Phillips, *Phys. Rev. Lett.* **27**, 1197 (1971).

Table 3.1 LO and TO phonon frequencies and FWHM of LO phonon for $Zn_{1-x}Cd_xSe$ epilayers.

Cd content (x)	LO phonon frequency (cm^{-1})	TO phonon frequency (cm^{-1})	FWHM of LO phonon (cm^{-1})
0	252.2	205.4	9.3
0.06	248.4	203.3	10.1
0.11	247.9	201.6	10.9
0.18	244.6	-	14.3
0.25	242.1	-	16.4
0.32	239.1	-	17.7

Table 3.2 Pressure-dependent LO phonon frequencies (ω_{LO}), $d\omega_{LO}/dp$, calculated mode Grüneisen parameters (γ_{LO}) and phase transition pressures for $Zn_{1-x}Cd_xSe$ epilayers.

Cd content (x)	ω_{LO} (cm^{-1})	$d\omega_{LO}/dp$ (cm^{-1}/GPa)	Grüneisen parameter (γ_{LO})	Phase transition pressure (GPa)
0	$252.2 + 3.31p - 0.04p^2$	$3.31 - 0.08p$	0.82	13.6 ± 0.2
0.06	$248.4 + 3.99p - 0.06p^2$	$3.99 - 0.12p$	1.00	12.9 ± 0.1
0.11	$247.9 + 4.26p - 0.09p^2$	$4.26 - 0.18p$	1.07	12.6 ± 0.1
0.18	$244.6 + 4.51p - 0.06p^2$	$4.51 - 0.12p$	1.15	12.0 ± 0.2
0.25	$242.1 + 3.82p - 0.09p^2$	$3.82 - 0.18p$	0.98	10.6 ± 0.4
0.32	$239.1 + 4.53p - 0.09p^2$	$4.53 - 0.18p$	1.18	9.4 ± 0.2

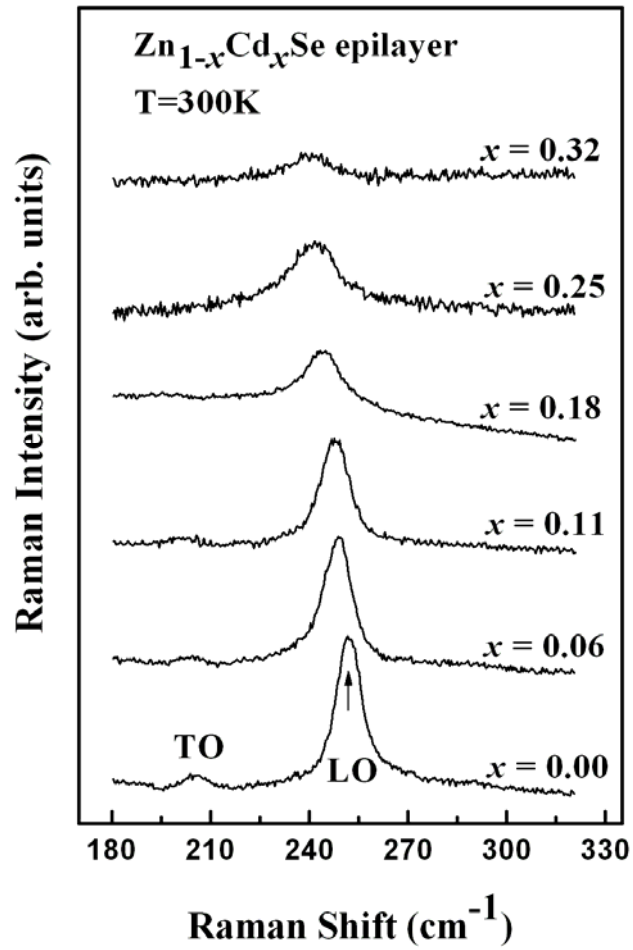


FIG. 3.1 Raman spectra of Zn_{1-x}Cd_xSe epilayers ($0 \leq x \leq 0.32$) at 300 K and ambient pressure.

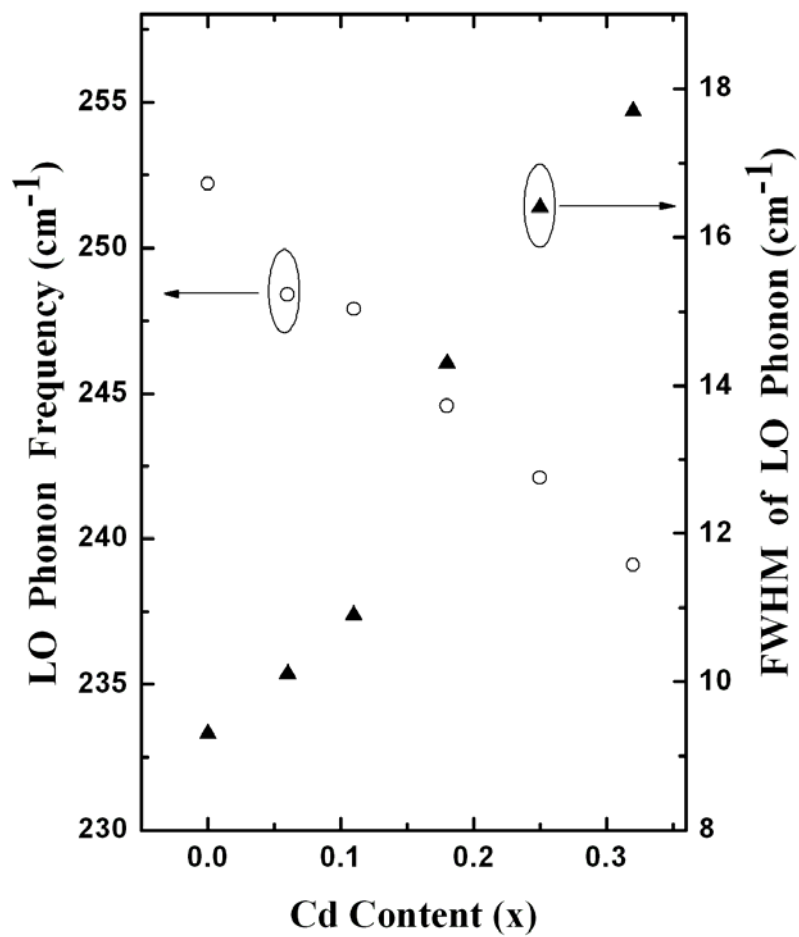


FIG. 3.2 Dependence of LO phonon frequencies (open circle) and FWHM (solid triangle) on Cd concentration (x).

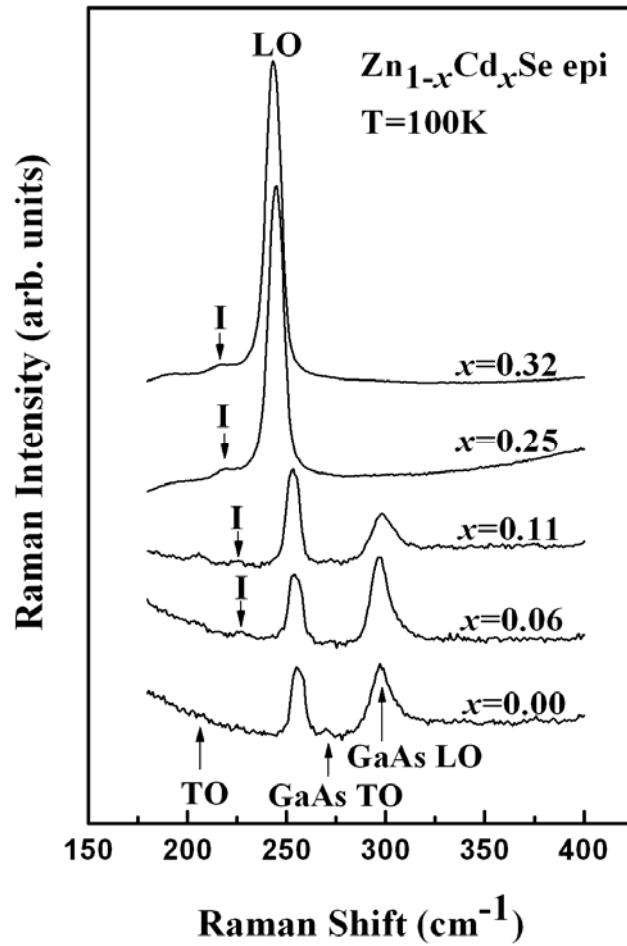


FIG. 3.3 Raman spectra of Zn_{1-x}Cd_xSe epilayers ($0 \leq x \leq 0.32$) at 100 K and ambient pressure. The impurity (*I*) modes, indicated by black arrows, appear at low temperature. The LO and TO phonons of the GaAs substrate are also labeled.

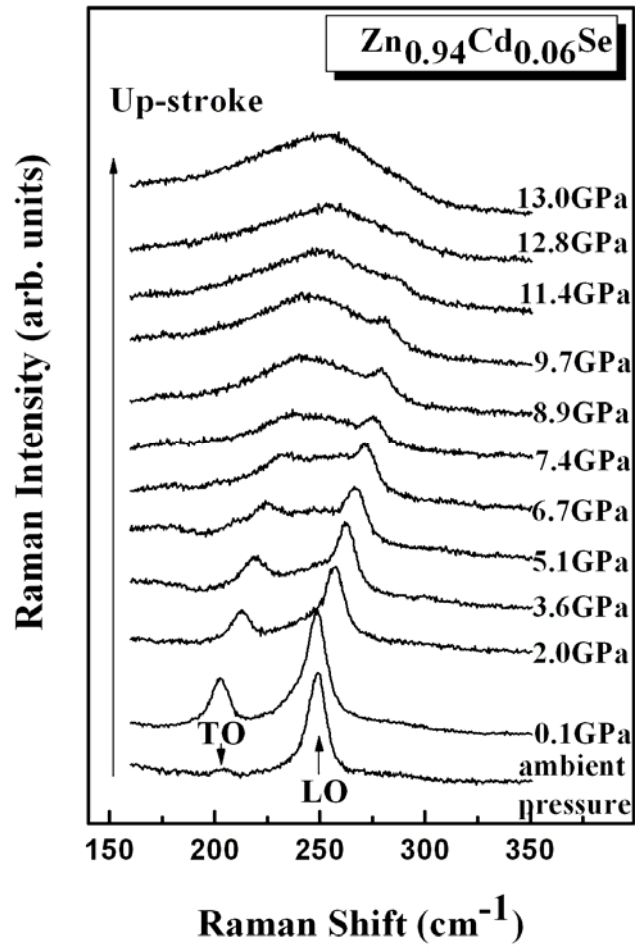


FIG. 3.4 Up-stroke pressure-dependent Raman spectra of $\text{Zn}_{1-x}\text{Cd}_x\text{Se}$ ($x = 0.06$) at room temperature. The LO phonon disappears at around 13.0 GPa, revealing a phase change from semiconductor to metal.

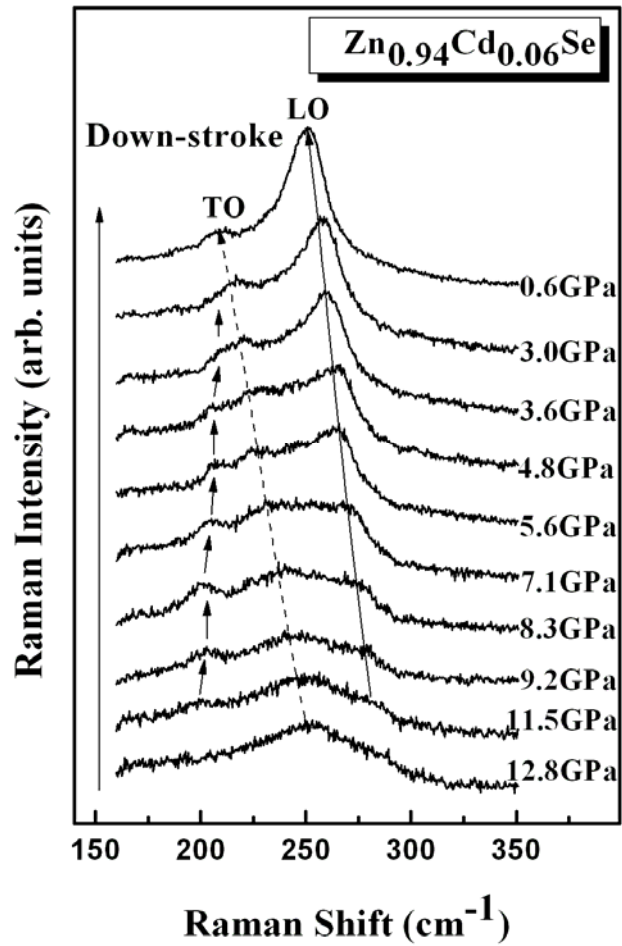


FIG. 3.5 Down-stroke pressure-dependent Raman spectra of $\text{Zn}_{1-x}\text{Cd}_x\text{Se}$ ($x = 0.06$) at room temperature. The splitting of the TO phonon, labeled by black arrows, was observed clearly as the pressure was released.

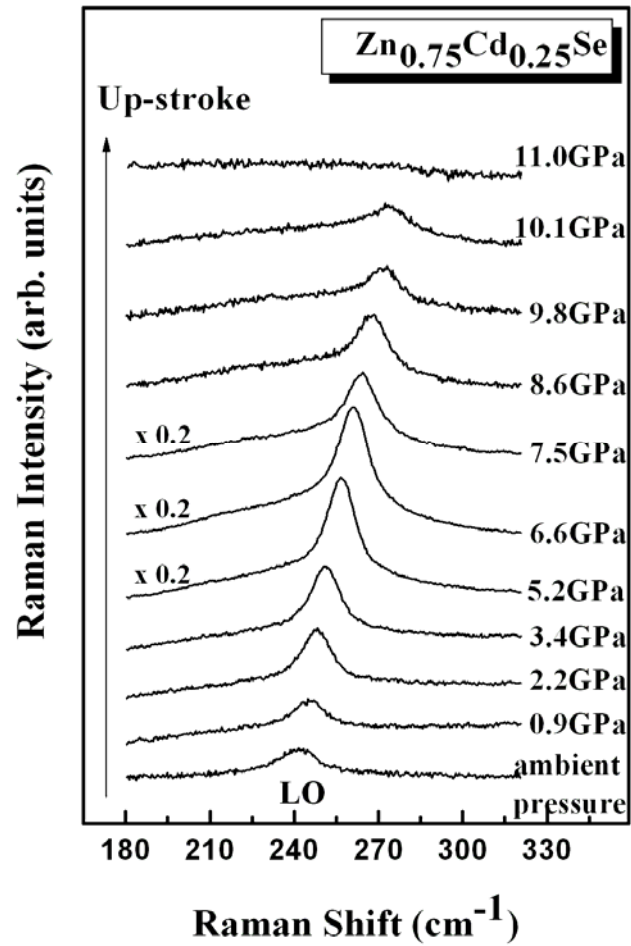


FIG. 3.6 Up-stroke pressure-dependent Raman spectra of $Zn_{1-x}Cd_xSe$ ($x = 0.25$) at room temperature. The pressure-driven resonant Raman scattering effect occurred as the pressure was increased. The LO phonon was found to disappear at about 11.0 GPa.

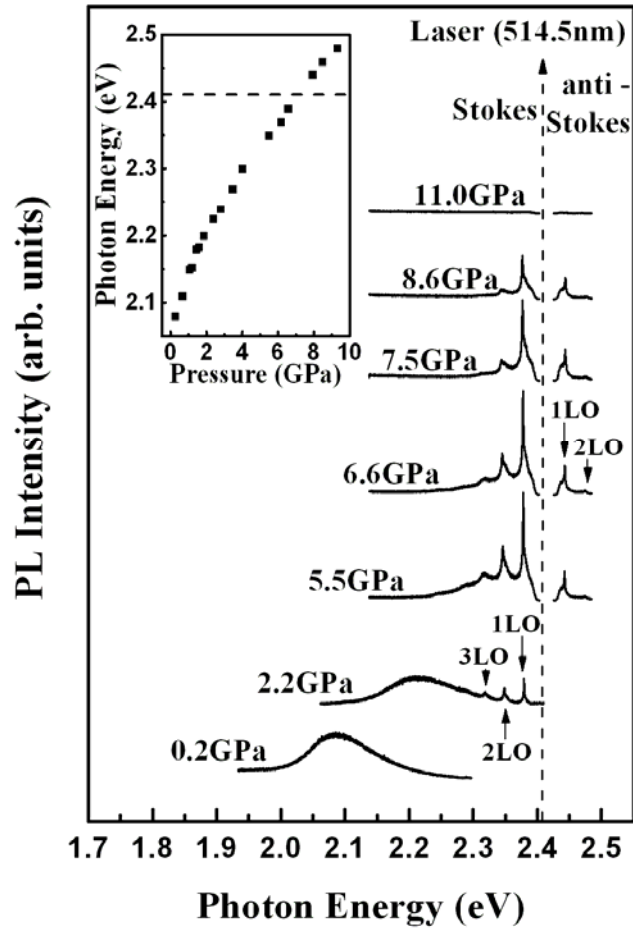


FIG. 3.7 Pressure-dependent photoluminescence spectra of Zn_{1-x}Cd_xSe ($x = 0.25$) at 300 K. The 514.5 nm (2.41 eV) Ar⁺ laser was fixed as an excitation source. The black dashed arrow at 2.41 eV labels the energy of the excitation laser, whereas the Stokes and anti-Stokes Raman spectra occur at the lower and higher energy sides of the laser, respectively. The inset plots the pressure dependence of PL energies, and the dashed line indicates the energy of the excitation laser.

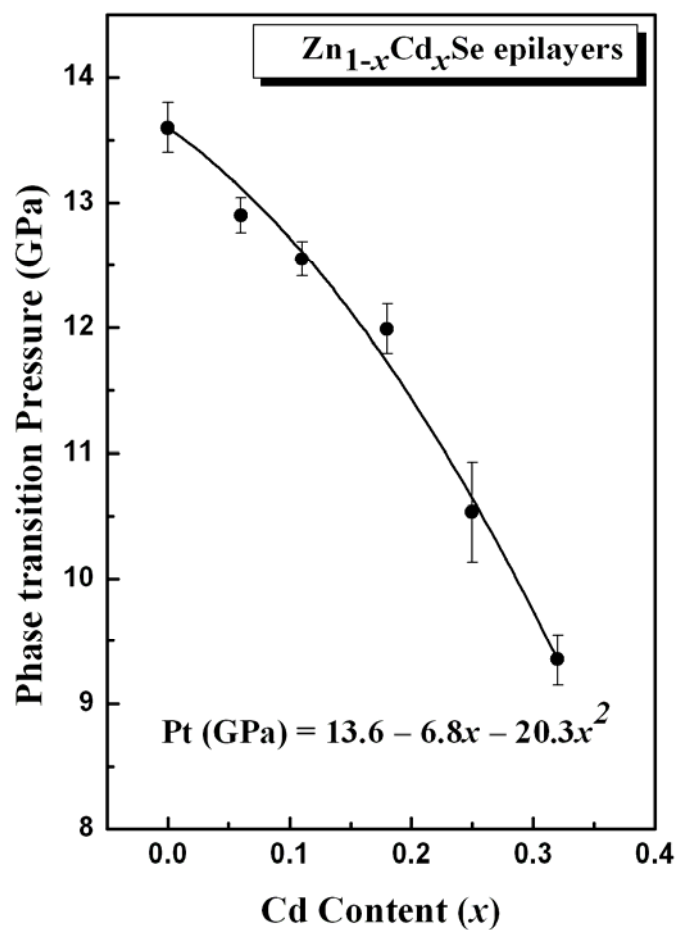
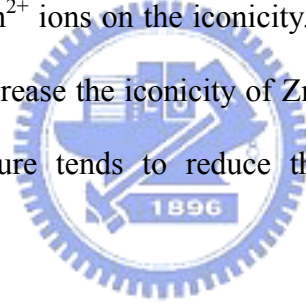


FIG. 3.8 Cd concentration (x)-dependent phase transition (semiconductor-to-metal) pressure of $\text{Zn}_{1-x}\text{Cd}_x\text{Se}$ epilayers. The solid curve represents a quadratic polynomial fit.

Chapter 4 Pressure-Induced Metallization and Resonant Raman Scattering in $\text{Zn}_{1-x}\text{Mn}_x\text{Te}$

In this chapter, pressure-induced resonant Raman scattering is adopted to analyze the zone-center optical phonon modes and crystal characteristics of $\text{Zn}_{1-x}\text{Mn}_x\text{Te}$ ($0 \leq x \leq 0.26$) thin films. The pressure (Pt) at which the semiconducting undergoes a transition to the metallic phase declines as a function of Mn concentration (x) according to the formula, $P_t(x) = 15.7 - 25.4 x + 19.0 x^2$ (GPa). Pressure-dependent longitudinal and transverse optical phonon frequencies and the calculated mode Grüneisen parameters were adopted to investigate the influence of Mn^{2+} ions on the ionicity. The experimental results indicate that the manganese ions tend to increase the ionicity of ZnTe under ambient conditions, whereas an external hydrostatic pressure tends to reduce the ionicity and the bond length of $\text{Zn}_{1-x}\text{Mn}_x\text{Te}$.



I. Introduction

Dilute magnetic semiconductor (DMS) $\text{Zn}_{1-x}\text{Mn}_x\text{Te}$, in which a fraction of Zn element are replaced by Mn atoms, crystallizes in the zincblende (ZB) structure for $x \leq 0.8$ under ambient conditions [1]. Magnetic properties of $\text{Zn}_{1-x}\text{Mn}_x\text{Te}$ -related materials are currently a focus of research activities in numerous interesting investigations [2-6]. Magnetic ordering in semiconductors can arise from the super-exchange interaction or free carrier-mediated exchange interaction between magnetic ions. Long-range ferromagnetic orderings, mediated by holes, were observed in $\text{Ga}_{1-x}\text{Mn}_x\text{As}$ [7] and $\text{In}_{1-x}\text{Mn}_x\text{As}$ [8], in which manganese ions act as acceptors. Alternatively, p-doped $\text{Zn}_{1-x}\text{Mn}_x\text{Te}$, in which magnetic ions are not dopants,

exhibits ferromagnetism that is induced by the exchange interaction of free holes with the localized spins of Mn^{2+} ions [3-6]. Moreover, our recent high-pressure study of n-doped ZnSe:Cl demonstrated that the hydrostatic pressure tends to reduce the carrier concentration, and that doping influences the metallic phase transition [9]. Therefore, the effect of applied pressure on the physical properties of DMS $Zn_{1-x}Mn_xTe$ will be of interest in future studies of the pressure-dependent magnetic properties of this material.

Pressure-induced phase transitions of ZnTe bulk crystal have been widely studied [10-13]. So far, all of the evidence has shown that the application of pressure to a semiconducting ZnTe exhibits a unique transition sequence. As the pressure is increased, the semiconducting ZB ZnTe phase (ZnTe I) first transforms to the other semiconducting cinnabar phase (ZnTe II), and then undergoes a transition to a metallic orthorhombic (*Cmcm*) phase (ZnTe III). These high-pressure phase behaviors differ from those of most II-VI semiconductors [14-16], which transform from ZB (or wurtzite) first to the cinnabar structure and then to the rocksalt (NaCl) structure as external pressure is applied. Even though the NaCl phase is unstable and has not been observed in ZnTe at room temperature under any pressure, it has been revealed to be stable only at high temperature [17]. This result is attributed to the fact that ZnTe is the lowest ionic semiconductor in the II-VI family [18]. The transition pressure from nonmetallic ZnTe to metallic ZnTe III (*Cmcm*) phase is controversial. Optical-absorption measurements yield a transition pressure of 11.9 GPa [10]. The electrical resistance approach yield a transformation of 13 ~ 15 GPa [11]. The metallic phase of ZnTe, as revealed by Raman scattering, forms at above 14.2 GPa [12]. Moreover, the crystalline structure of the ZnTe phase III is determined to be 16 GPa using angle-dispersive powder-diffraction techniques with synchrotron radiation [13]. To resolve these unusual and controversial phase transitions at high pressure, Raman scattering under high pressure was performed to investigate ZnTe and $Zn_{1-x}Mn_xTe$ thin films up to 17.0 GPa. Furthermore,

resonant Raman scattering (RRS) was adopted to enhance the Raman signal to identify more clearly semiconductor-to-metal phase transition pressure. The crystalline stability, ionicity, and Grüneisen parameters (γ_i) of $\text{Zn}_{1-x}\text{Mn}_x\text{Te}$ ($0 \leq x \leq 0.26$) thin films were also studied.

II. Experiment

$\text{Zn}_{1-x}\text{Mn}_x\text{Te}$ samples with various Mn contents ($0 \leq x \leq 0.26$) were deposited at 300 °C by molecular beam epitaxy on (001) oriented semi-insulating GaAs substrates. The samples' thicknesses were fixed at about 0.7 μm , and the Mn composition was determined by energy-dispersive X-ray analysis. Raman spectra under ambient pressure were all recorded at 300 K and excited using the 514.5 nm line of an Ar^+ laser, while the 488.0 nm line from the Ar^+ laser was used in high-pressure experiments. High-pressure Raman measurements were all made at room temperature using a ruby-calibrated diamond anvil cell (DAC) [Ref. 9]. A liquid methanol-ethanol 4:1 mixture was utilized as the pressure-transmitting medium, and the pressure gradient was less than 0.2 GPa throughout the sample chamber. Before loading the $\text{Zn}_{1-x}\text{Mn}_x\text{Te}$ crystal into the DAC, the GaAs substrate was removed by mechanical polishing and chemical etching. Spectra were all obtained in backscattering configuration and analyzed by a SPEX 1404 double grating spectrometer equipped with a multichannel LN_2 -cooled CCD. The high-pressure experiments are reproducible for each specimen. The PL energies were obtained at 300 K, using the 488.0 nm line of an Ar^+ laser.

III. Results and Discussion

Figure 4.1 presents the zone-center Raman spectra of $\text{Zn}_{1-x}\text{Mn}_x\text{Te}$ ($x = 0.00, 0.09, 0.14, 0.22, \text{ and } 0.26$), measured at room temperature and ambient pressure under $z(x+y, x+y)\bar{z}$ backscattering geometry. In this configuration, transverse optical (TO)

phonons are forbidden and longitudinal optical (LO) phonons are allowed. As the Mn content increases, the 1LO and its overtone (2LO) phonon frequencies increase. Figure 4.2 plots the dependence of the 1LO phonon frequency and the PL energy on the Mn concentration (x). The increase in the LO phonon frequency with Mn content is due to the difference between atomic masses, m_{Mn} (55) < m_{Zn} (65). As the Mn concentration increases, the PL energy is blueshifted and slowly approaches the incident laser energy. When the energy of the electronic transition energy is sufficiently close to the incident laser energy, the RRS effect occurs, enhancing the intensity of LO phonons. Based on the RRS condition,

$$h\nu_{\text{laser}} - mh\nu_{\text{LO}}(x, p) \approx E_{\text{exc}}(x, p), \quad (1)$$

where $h\nu_{\text{laser}}$ is the photon energy of the incident laser. $E_{\text{exc}}(x, p)$ and $h\nu_{\text{LO}}(x, p)$ are the electronic transition energy and the LO phonon energy, respectively, as functions of Mn content (x) and applied pressure (p). The m denotes the overtone order of LO phonons. Under ambient conditions, when the laser is fixed at 2.41 eV, the Raman scattering of the larger overtone phonon comes into resonance first (Fig. 4.1). As shown in Fig. 4.1, besides the LO mode, an impurity (I) mode and its overtone ($2I$) at the lower-frequency side of the LO phonon in $\text{Zn}_{1-x}\text{Mn}_x\text{Te}$ ($x > 0$) are also visible. As the Mn content increases, the impurity (I and $2I$) modes shift to lower frequencies and become intense. Similar phenomena are also found in $\text{Zn}_{1-x}\text{Mn}_x\text{Se}$ [15] and $\text{Zn}_{1-x}\text{Cd}_x\text{Se}$ [16] II-VI ternary compounds. Since the impurity mode discussed herein lies between the LO and TO modes and can also be apparently observed at high pressure, it can be identified as the impurity mode of Mn in ZnTe. Accordingly, the zone-center optical phonon mode of $\text{Zn}_{1-x}\text{Mn}_x\text{Te}$ can be concluded to exhibit mixed-mode behavior. This finding is consistent with an earlier work [1].

Figure 4.3 shows the up-stroke pressure-dependent Raman spectra of the ZnTe thin film at up to 17.0 GPa. The TO mode, which is not allowed under ambient conditions before pressurization, appears at high pressure. The emergence of the TO mode can be attributed to

the pressure-induced RRS enhancement and the deviation of the sample chip from the perfect backscattering geometry in the DAC. The LO and TO phonon both shift to higher frequencies with increasing pressure, wherein the shift is accompanied by clear changes in their intensities. The reduction in the lattice constant and the crystal volume under external pressure increases LO and TO phonons frequencies. The pressure-driven RRS effect, according to Eq. (1), causes the intensity of LO phonon to increase abruptly at first and then to decline smoothly. As the pressure increases, the LO phonon disappears and the sample becomes opaque at 15.7 ± 0.2 GPa, indicating a semiconductor-to-metal phase transition [9,14-16]. This phenomenon is distinct from that revealed by the Raman results of Camacho *et al.* [12], in which the LO phonon was invisible above 9.6 GPa - far below the pressure obtained under the RRS condition discussed herein. The metallic phase transition pressure of ZnTe, measured by the RRS experiment, is consistent with the experimental results of Nelmes *et al.* [13], who determined, using angle-dispersive diffraction techniques with synchrotron radiation source, which the crystal structure changed to the ZnTe phase III at 16 GPa. Recently, Shchennikov and Ovsyannikov revealed that the sharp drop of resistance from 10^6 to $10^1 \Omega$ in ZnTe at about 13.0 ~ 15.0 GPa is related to the transformation into the orthorhombic *Cmcm* phase [11]. The difference between the phase-transition pressures obtained by X-ray and electrical resistance methods is attributable to the fact that X-ray techniques determine the phase transition pressure closer to the completion of the transformation, whereas the electrical resistance measurements reveal the beginning of the transition [11]. In Fig. 4.3, the TO mode does not disappear until at about 17.0 GPa. Other II-VI compounds exhibited similar phenomenon because transverse surface lattice vibration is allowed in both semiconductor and metal, even though the skin depth (or penetration depth) of the metal for a laser is only several tens of angstroms [9,14-16]. In the down-stroke high-pressure process, only hysteresis is observed, and no additional phonon appears.

Figure 4.4 displays the up-stroke pressure-dependent Raman spectra of $\text{Zn}_{0.91}\text{Mn}_{0.09}\text{Te}$. In addition to the LO and TO modes, a Mn-related impurity mode (I) and a double structure associated to LO + TA (transverse acoustic) phonon appear between LO and TO phonons and at the higher-frequency side of the LO phonon, respectively. As the pressure increases, the impurity mode, the LO phonon, and the TO phonon shift to high frequencies which can be fitted by a quadratic polynomial, listed in Table 4.1. Since Zn is partially replaced by Mn, the intensity of the Raman spectra is lower than that of ZnTe, because the 3d orbital of Mn^{2+} ions hybridizes into tetrahedral bonds, causing distortions and altering the overall ZnMnTe crystal symmetry. Furthermore, the LO phonon becomes opaque and disappears at 13.6 ± 0.2 GPa. When the pressure is 15.7 GPa, the TO and I modes become invisible. As the Mn content is increased from 0 to 0.09, the semiconductor-to-metal phase transition pressure falls from 15.7 to 13.6 GPa.

Figure 4.5 plots the phase transition pressure as a function of the Mn content. A decline in the semiconductor-to-metal phase transition pressure (Pt) versus x is shown and is fitted using a quadratic curve, given by $P_t(x) = 15.7 - 25.4x + 19.0x^2$ (GPa). As the Mn content increases from 0 to 0.26, the phase transition pressure falls from 15.7 to 10.3 GPa (Table 4.1), indicating that the substituted Mn^{2+} ions tend to reduce the stability of the crystal. The Mn^{2+} ions in $\text{Zn}_{1-x}\text{Mn}_x\text{Te}$ may alter the overall symmetry and soften the lattice by generating large distortions. As the substituted element content increases, the structure becomes less stable. This dependence is similar to other DMS II-VI ternary compounds. Yang *et al.* [15] found that, for $\text{Zn}_{1-x}\text{Mn}_x\text{Se}$ compounds, as x is increased from 0.07 to 0.24, the pressure of the metallic phase transition falls from 11.8 to 9.9 GPa. For the $\text{Zn}_{1-x}\text{Fe}_x\text{Se}$ semiconductor, the existence of Fe ions ($x = 0.16$) in the ZnSe reduces the semiconductor-metal phase transition pressure from 14.4 to 10.9 GPa [14]. Table 4.1 summarizes the pressure-dependent LO, TO, and I phonon frequencies derived from quadratic polynomial fits to our measurements. Moreover, the

pressure dependence of a mode frequency ω_i can be defined using the dimensionless Grüneisen parameters (γ_i) [Ref. 19],

$$\gamma_i = -\left(\frac{d \ln \omega_i}{d \ln V}\right) = \frac{1}{\beta} \frac{\partial \ln \omega_i}{\partial p} = \left(\frac{K_0}{\omega_i}\right) \left(\frac{d \omega_i}{dp}\right), \quad (2)$$

where K_0 is the bulk modulus, defined as the reciprocal of the isothermal volume compressibility (β), and V is the molar volume in cm^3/mol . Since the bulk modulus (K_0) of $\text{Zn}_{1-x}\text{Mn}_x\text{Te}$ is unavailable, $K_0(\text{ZnTe}) = 50.5 \text{ GPa}$ is used [20]. As shown in Table 4.1, several conclusions can be drawn. At ambient pressure ($p \sim 0$), (i) the LO phonon frequency increases and the TO phonon frequency decreases as the Mn composition increases: the LO-TO splitting increases with Mn content; (ii) $\gamma_{\text{LO}} < \gamma_{\text{TO}}$ is observed throughout all the specimens, and the ratio, $\gamma_{\text{TO}} / \gamma_{\text{LO}}$, rises from 1.38 to 1.77 as the Mn concentration increases from 0 to 0.26. At high pressure, (iii) $d\omega_{\text{LO}}/dp < d\omega_{\text{TO}}/dp$, such that the LO-TO splitting falls under external pressure for all samples herein; (iv) $d\omega_i/dp$ and γ_i follow no consistent trend over the entire Mn range of interest ($0.09 \leq x \leq 0.26$). These results demonstrate that under ambient conditions, the manganese ions slightly increase the ionicity of ZnTe. Nevertheless, an externally applied pressure reduces the ionicity and bond length of $\text{Zn}_{1-x}\text{Mn}_x\text{Te}$ crystals.

IV. Conclusions

Resonant Raman scattering can enhance the LO and TO phonon intensities in studying pressure-dependent vibrational spectra of $\text{Zn}_{1-x}\text{Mn}_x\text{Te}$ thin films. Intermediate optical phonon mode behavior was identified. The disappearance of the LO phonon, which accompanies a semiconductor-to-metal phase transition in ZnTe occurs at about $15.7 \pm 0.2 \text{ GPa}$. As the Mn content increases from 0 to 0.26, the metallic phase transition pressure falls from 15.7 to 10.3 GPa. Based on the pressure-dependent LO and TO phonon frequencies and Grüneisen parameters (γ_i), externally applying pressure reduces the ionicity of $\text{Zn}_{1-x}\text{Mn}_x\text{Te}$.

References

- [1] D. L. Peterson, A. Petrou, W. Giriat, A. K. Ramdas, and S. Rodriguez, *Phys. Rev. B* **33**, 1160 (1986).
- [2] M. C. Kuo, J. S. Hsu, J. L. Shen, K. C. Chiu, W. C. Fan, Y. C. Lin, C. H. Chia, W. C. Chou, M. Yasar, R. Mallory, A. Petrou, and H. Luo, *Appl. Phys. Lett.* **89**, 263111 (2006).
- [3] H. Keça, L. V. Khoi, C. M. Brown, M. Sawicki, J. K. Furdyna, T. M. Giebultowicz, and T. Dietl, *Phys. Rev. Lett.* **91**, 087205 (2003).
- [4] Le Van Khoi, M. Sawicki, K. Dybko, V. Domukhovski, T. Story, T. Dietl, A. Jędrzejczak, J. Kossut, and R. R. Gałazka, *phys. stat. sol. (b)* **229**, 53 (2002).
- [5] Le Van Khoi and R. R. Gałazka, *phys. stat. sol. (c)* **3**, 837 (2006).
- [6] D. Ferrand, J. Cibert, A. Wasiela, C. Bourgognon, S. Tatarenko, G. Fishman, T. Andrearczyk, J. Jaroszyński, S. Koleśnik, T. Dietl, B. Barbara, and D. Dufeu, *Phys. Rev. B* **63**, 085201 (2001).
- [7] H. Ohno, A. Shen, F. Matsukura, A. Oiwa, A. End, S. Katsumoto, and Y. Iye, *Appl. Phys. Lett.* **69**, 363 (1996).
- [8] H. Munekata, H. Ohno, S. von Molnar, A. Segmüller, L. L. Chang, and L. Esaki, *Phys. Rev. Lett.* **63**, 1849 (1989).
- [9] Y. C. Lin, C. H. Chiu, W. C. Fan, S. L. Yang, D. S. Chuu, M. C. Lee, W. K. Chen, W. H. Chang, and W. C. Chou, *J. Appl. Phys.* **102**, 123510 (2007).
- [10] K. Strössner, S. Ves, C. K. Kim, and M. Cardona, *Solid State Commun.* **61**, 275 (1987).
- [11] V. V. Shchennikov, S. V. Ovsyannikov, A. Y. Derevskov, and V. V. Shchennikov Jr, *J. Phys. Chem. Sol.* **67**, 2203 (2006).
- [12] J. Camacho, I. Loa, A. Cantarero, and K. Syassen, *High Pressure Research* **22**, 309 (2002).
- [13] R. J. Nelmes, M. I. McMahon, N. G. Wright, and D. R. Allan, *Phys. Rev. Lett.* **73**, 1805

(1994).

[14] C. M. Lin, D. S. Chuu, T. J. Yang, W. C. Chou, J. Xu, and E. Huang, *Phys. Rev. B* **55**, 13641 (1997).

[15] C. S. Yang, C. S. Ro, W. C. Chou, C. M. Lin, D. S. Chuu, J. Hu, E. Huang, and J. Xu, *J. Appl. Phys.* **85**, 8092 (1999).

[16] Y. C. Lin, C. H. Chiu, W. C. Fan, S. L. Yang, D. S. Chuu, and W. C. Chou, *J. Appl. Phys.* **101**, 073507 (2007).

[17] A. Mujica, A. Munoz, and R. J. Needs, *Rev. Mod. Phys.* **75**, 863 (2003), and references therein.

[18] J. C. Phillips, *Phys. Rev. Lett.* **27**, 1197 (1971).

[19] M. Blackman and W. B. Daniels, in *Light Scattering in Solids IV*, edited by M. Cardona and G. Güntherodt (Springer, Berlin, 1984), Chap. 8.

[20] A. San-Miguel, A. Polian, M. Gauthier, and J. P. Itié, *Phys. Rev. B* **48**, 8683 (1993).

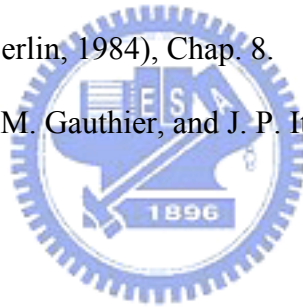


Table 4.1 Pressure-dependent LO, TO, and I phonon frequencies (ω_i), $d\omega_i/dp$, calculated mode Grüneisen parameters (γ_i), and phase transition pressures of $\text{Zn}_{1-x}\text{Mn}_x\text{Te}$.

Mn content (x)	mode	ω_i (cm^{-1})	$d\omega_i/dp$ ($\text{cm}^{-1}/\text{GPa}$)	Grüneisen parameter (γ_i)	Phase transition pressure (GPa)
0	LO	$203.6 + 3.42p - 0.10p^2$	$3.42 - 0.20p$	0.85	15.7 ± 0.2
	TO	$179.2 + 4.16p - 0.11p^2$	$4.16 - 0.22p$	1.17	
0.09	LO	$206.3 + 3.34p - 0.11p^2$	$3.34 - 0.22p$	0.82	13.6 ± 0.2
	TO	$177.0 + 4.26p - 0.09p^2$	$4.26 - 0.18p$	1.22	
	I	$193.4 + 3.15p - 0.08p^2$	$3.15 - 0.16p$	0.82	
0.14	LO	$207.4 + 3.29p - 0.10p^2$	$3.29 - 0.20p$	0.80	12.4 ± 0.2
	TO	$176.1 + 4.30p - 0.06p^2$	$4.30 - 0.12p$	1.24	
	I	$192.0 + 2.90p - 0.06p^2$	$2.90 - 0.12p$	0.76	
0.22	LO	$208.7 + 3.15p - 0.03p^2$	$3.15 - 0.06p$	0.76	11.2 ± 0.2
	TO	$175.5 + 4.43p - 0.14p^2$	$4.43 - 0.28p$	1.27	
	I	$189.7 + 3.02p - 0.05p^2$	$3.02 - 0.10p$	0.80	
0.26	LO	$209.7 + 3.06p - 0.08p^2$	$3.06 - 0.16p$	0.74	10.3 ± 0.2
	TO	$174.8 + 4.55p - 0.07p^2$	$4.55 - 0.14p$	1.31	
	I	$187.4 + 3.18p - 0.08p^2$	$3.18 - 0.16p$	0.85	

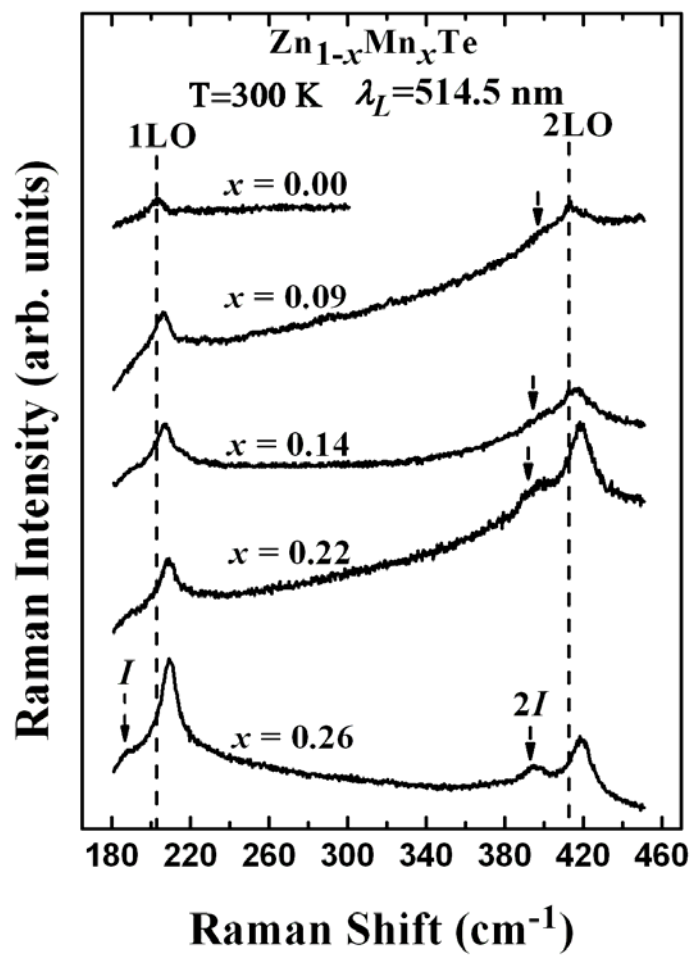


FIG. 4.1. Raman spectra of Zn_{1-x}Mn_xTe ($0 \leq x \leq 0.26$) at 300 K under ambient pressure.

The excitation source is a 514.5 nm line from an Ar⁺ laser.

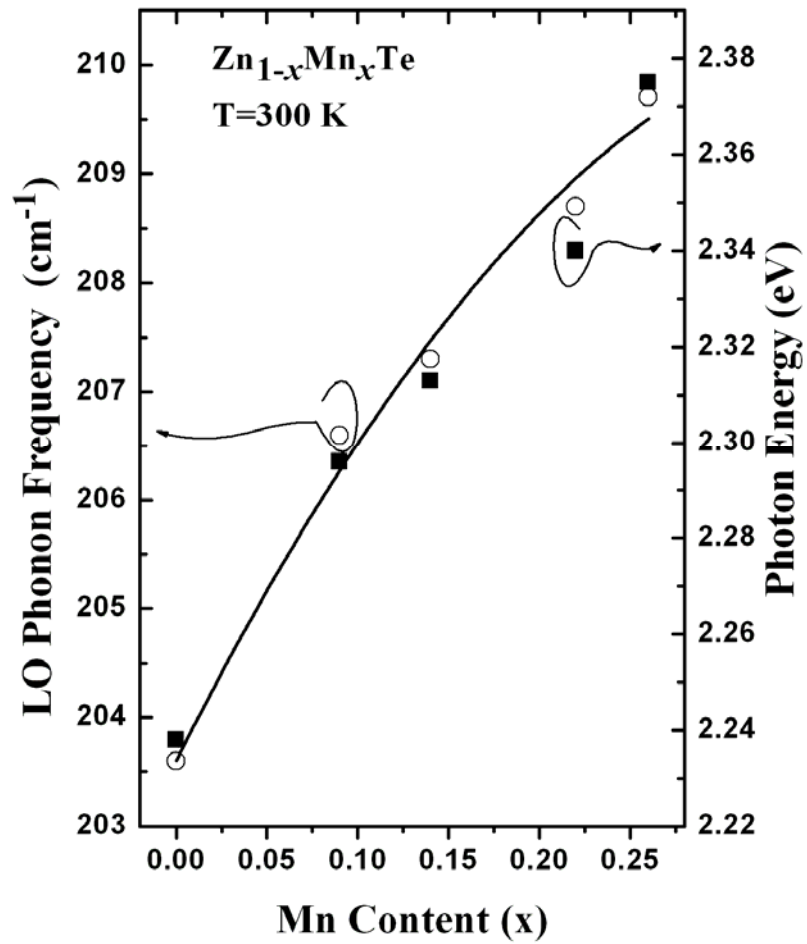


FIG. 4.2. Dependence of LO phonon frequencies (open circle) and PL energy (solid square) on Mn concentration (x) at room temperature. The solid curve is a quadratic polynomial fit for the LO phonon.

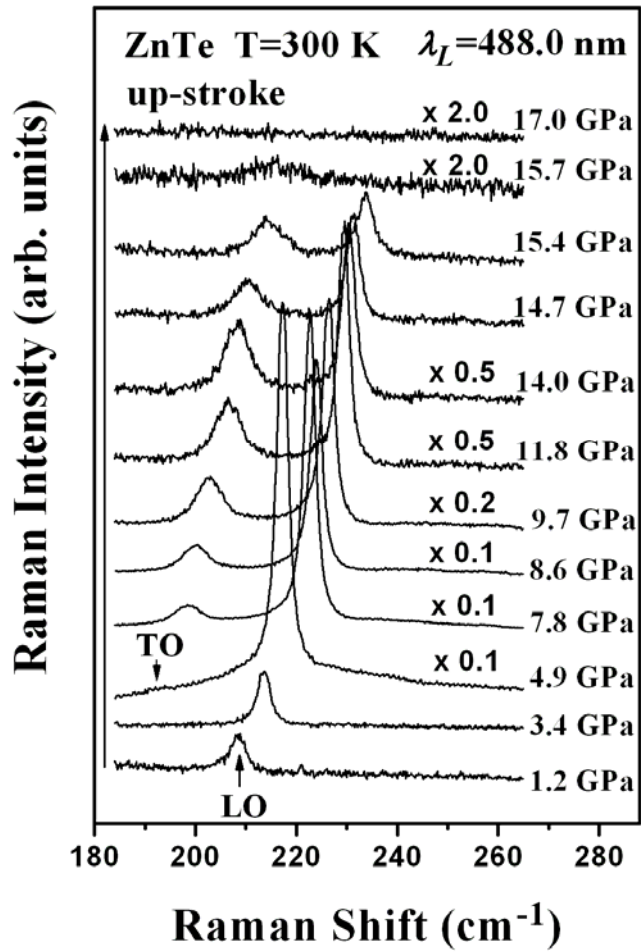


FIG. 4.3. Up-stroke pressure-dependent Raman spectra of ZnTe at 300 K. Black arrows indicate the LO and the TO phonons. The excitation source is a 488.0 nm line from an Ar^+ laser. The pressure-induced RRS enhancement occurs as the external pressure is increased.

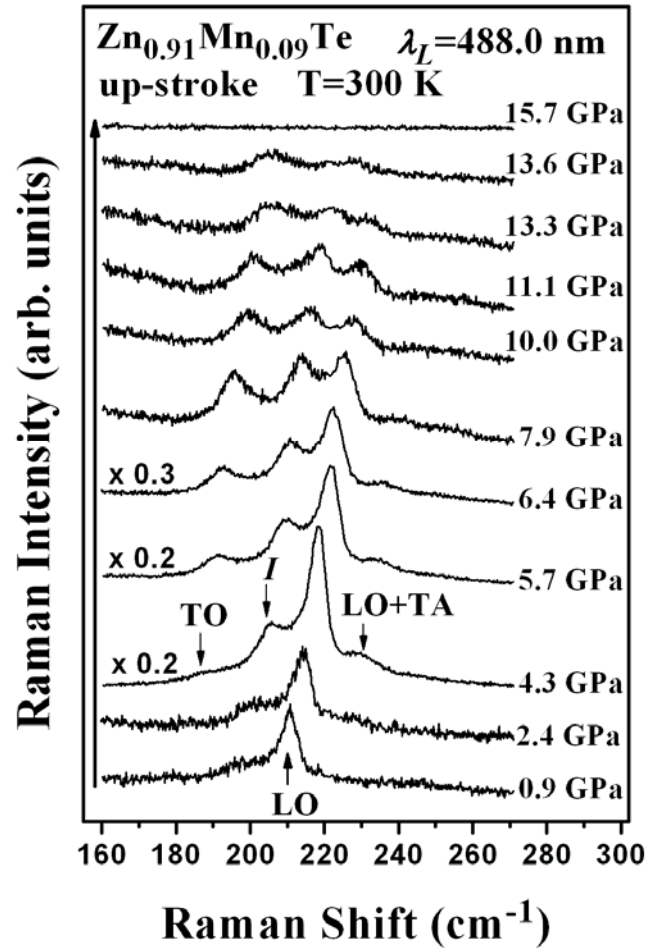


FIG. 4.4. Up-stroke pressure-dependent Raman spectra of $\text{Zn}_{0.91}\text{Mn}_{0.09}\text{Te}$ at 300 K. LO, TO, LO + TA, and impurity (I) modes are labeled.

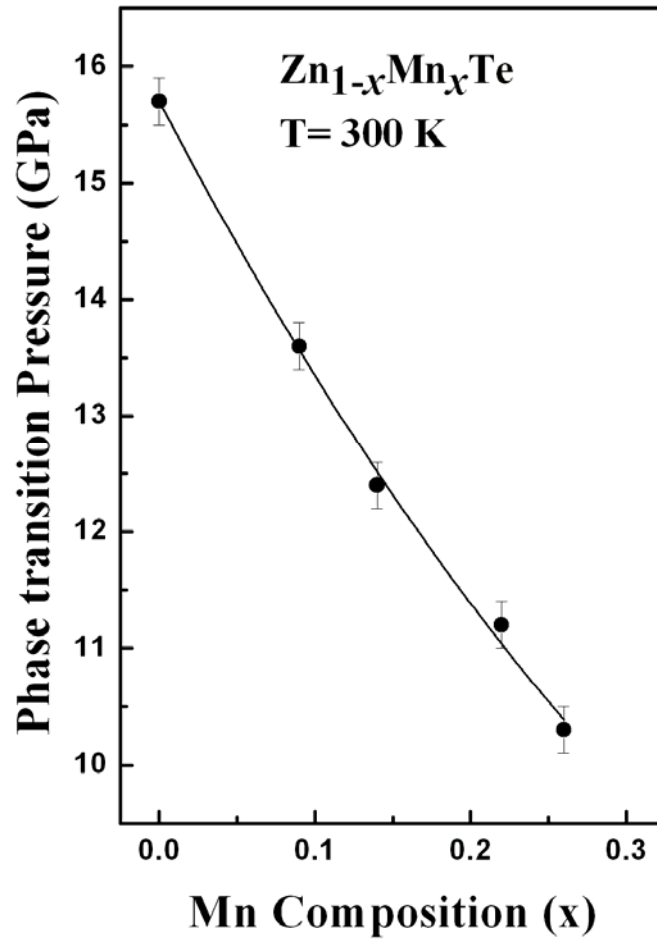


FIG. 4.5. Mn concentration (x)-dependent semiconductor-to-metal phase transition pressure of $\text{Zn}_{1-x}\text{Mn}_x\text{Te}$. The solid curve is a quadratic polynomial fit, given by $P_t(x) = 15.7 - 25.4x + 19.0x^2$ (GPa).

Chapter 5 Raman Scattering of Longitudinal Optical Phonon-Plasmon Coupling in Cl-Doped ZnSe under High Pressure

This chapter, the vibrational, electronic, and crystalline properties of n-type chlorine-doped ZnSe (ZnSe:Cl) layers with a carrier concentration from 8.2×10^{15} to $1.8 \times 10^{18} \text{ cm}^{-3}$ will be studied by Raman spectroscopy. The spectral lineshapes of the longitudinal-optical-phonon and plasmon coupling (LOPC) mode are analyzed using the Raman scattering efficiency and the dielectric function to obtain the electron densities and mobility. The splitting of the transverse-optical (TO) phonon and the redshift of the chlorine-related impurity vibration mode are clearly observed when pressure is applied. The semiconductor-to-metal phase transition pressure of ZnSe:Cl layers declines as the carrier concentration increases, indicating that n-type doping reduces crystal stability. Additionally, the pressure-induced weakening of the longitudinal-optical-phonon-plasmon coupling efficiency suggests that pressure tends to degrade the n-type characteristic of ZnSe:Cl because of the emergence of the new deep donor-like state.

I. Introduction

Materials at high pressure exhibit interesting phenomena. For example, Mao *et al.* made optical measurements at ~ 250 GPa and observed that hydrogen becomes metallic due to band overlap [1]. Water (H_2O) molecules under high pressure cleave and form O_2 and H_2 bonds [2]. Semiconductors at high pressure also exhibit fascinating behavior. Smith *et al.* [3] found that ZnSe undergoes a crystallographic phase transition from a fourfold coordination zincblend

(ZB) structure to a sixfold-coordinated rocksalt (RS) structure at about 13.5 GPa. Itkin *et al.* studied the sharp drop of resistance from 10^{21} to $10^4 \Omega$ in ZnSe at 13.5 GPa [4], which indicates that pressure-induced metallization of ZnSe occurs when the crystalline structure is transformed from ZB to RS. The high-pressure resistance measurement is consistent with the optical measurement, yielding a monotonic energy blueshift with pressure and an abrupt transformation to opaque at 13.5 GPa [5]. Our earlier studies investigated the physical properties of undoped ZnSe [6] and ZnSe-based ternary compounds, ZnMnSe [7], ZnFeSe [6], ZnCdSe [8,9], and ZnSeTe [10], at high pressure using energy-dispersive x-ray diffraction (EDXD), Raman scattering and photoluminescence measurements. The disappearance of the LO phonon at high pressure is caused by the metallization of the ZnSe-based ternary compounds.

Recently, longitudinal-optical-phonon and plasmon coupling (LOPC) was investigated using Raman scattering to characterize the hole concentration of GaMnAs [11,12]. The strong interaction between LO phonons and collective excitations (plasmons) via their associated macroscopic electric fields has also been extensively studied [13] in other compound semiconductors such as SiC, GaAs, and GaN [14-16]. According to related works, the free carrier concentration and mobility can be obtained by analyzing the lineshapes of the measured Raman spectra. A question arises: based on the powerful high-pressure approach for tuning the physical properties of semiconductors, can the applied high pressure significantly alter the interesting LO phonon and plasmon coupling? The applied pressure modifies the vibration frequency of the LO phonon and the carrier concentration by contracting the lattice. A notable change in LOPC under the applied high pressure might be expected. In particular, little attention has been paid to the LOPC of the II-VI semiconductors because of their low electron mobility and large plasmon damping. Furthermore, the pressure-induced semiconductor-to-metal transition and the crystal stability of n-type ZnSe:Cl layers, which

are affected by the doping concentration, remain unexplored.

In this work, Raman scattering is adopted to investigate the LOPC as a function of applied pressure for n-type ZnSe:Cl layers. Based on the Raman scattering efficiency and the dielectric function, the spectral lineshape is analyzed to obtain the free carrier concentration and mobility. Moreover, the semiconductor-to-metal phase transition of n-type ZnSe:Cl layers is studied.

II. Experiment

ZnSe:Cl layers were grown by molecular beam epitaxy on semi-insulating GaAs (001) substrates, which were chemically etched and thermally desorbed to remove residual oxide just prior to growth. The Cl beam was supplied *in situ* from a ZnCl₂ compound source, using the conventional effusion cell. The Cl-doping level was controlled by adjusting the ZnCl₂ effuse temperature (T_{Cl}). The substrate temperature was maintained at 300 °C, and the thickness of the ZnSe:Cl layers was fixed at about 0.9 μm. The samples were electrically characterized using conventional Hall measurements at room temperature (RT) in the Van der Pauw configuration. The undoped sample was highly resistive with carrier concentration of under 10¹⁵ cm⁻³ at RT, and net n-type carrier concentration from 8.2 × 10¹⁵ to 1.8 × 10¹⁸ cm⁻³ for T_{Cl} between 110 and 140 °C were discussed.

High-pressure measurements were made in a gasket diamond anvil cell (DAC). A methanol-ethanol 4:1 mixed liquid, loaded under high pressure, was used as a pressure-transmitting medium to maintain the hydrostatic conditions. The hydrostatic pressure was calibrated by the spectral shift of the ruby R1 line. The pressure gradient was less than 0.2 GPa, as determined by measurements made at various positions of the sample chamber. Before the ZnSe:Cl sample was loaded into the DAC, the GaAs substrate was removed by mechanical polishing and chemical etching.

Raman spectra were obtained at RT and collected in the backscattering configuration using a 514.5 nm-line of an Ar⁺-ion laser as the excitation source. The spectra were obtained using a SPEX 1404 double grating spectrometer equipped with a multichannel LN₂-cooled charge-coupled device (CCD). The reproducibility of the Raman peak frequencies was better than $\pm 0.1 \text{ cm}^{-1}$. The photoluminescence (PL) spectra were obtained at RT, using the 325 nm-line of an He-Cd laser, and detected with a photo-multiplier tube (PMT).

III. Results and Discussion

Figure 5.1 presents the Raman spectra of n-type ZnSe:Cl layers for various carrier concentration and an undoped ZnSe layer. The spectra were all obtained at room temperature and ambient pressure under $z(x+y, x+y)\bar{z}$ backscattering geometry. In this configuration, based on the selection rule, scattering from LO phonon is allowed, while that from transverse optical (TO) phonon is forbidden. However, a weak TO feature, which appears at around 203.5 cm^{-1} , is attributable to a slight deviation from perfect backscattering geometry. As the carrier concentration increases from less than 10^{15} cm^{-3} (undoped) to $1.8 \times 10^{18} \text{ cm}^{-3}$ ($T_{Cl} = 140 \text{ }^\circ\text{C}$), the LO-phonon line shifts from 252.2 cm^{-1} to 248.8 cm^{-1} due to coupling of the LO phonons and plasmons (LOPC). This LOPC mode behavior is characteristic of semiconductors with low carrier mobility or large plasmon damping. Therefore, only one overdamped phononlike LOPC mode near the LO phonon is observed, rather than two coupled LOPC modes [11-13,17]. Also, the linewidth, which is the full width at half maximum (FWHM), of the LOPC mode broadens from 10.4 cm^{-1} to 25.6 cm^{-1} , and the peak intensity ratios (I_{LOPC} / I_{TO}), which are given in Table 5.1, drop from 6.7 to 1.3. A lineshape analysis of the LOPC mode is performed and displayed as solid lines in Fig. 5.1 to examine further the correlation between the vibrational and the electronic properties of n-type ZnSe:Cl for various carrier concentration. The lineshape fitting analysis is based on the Raman

efficiency and is given by [18]

$$I(\omega) = S A(\omega) \text{Im}[-1/\varepsilon(\omega)] \quad (1)$$

where ω represents the Raman shift and S is an ω -independent proportionality constant. $A(\omega)$ is a coefficient, given by

$$A(\omega) = 1 + 2C\omega_T^2[\omega_p^2\gamma(\omega_T^2 - \omega^2) - \omega^2\Gamma(\omega^2 + \gamma^2 - \omega_p^2)]/\Delta \\ + C^2(\omega_T^4/\Delta) \times \{\omega_p^2[\gamma(\omega_L^2 - \omega_T^2) + \Gamma(\omega_p^2 - 2\omega^2)] + \omega^2\Gamma(\omega^2 + \gamma^2)\}/(\omega_L^2 - \omega_T^2), \quad (2)$$

$$\Delta = \omega_p^2\gamma[(\omega_T^2 - \omega^2)^2 + (\omega\Gamma)^2] + \omega^2\Gamma(\omega_L^2 - \omega_T^2)(\omega^2 + \gamma^2). \quad (3)$$

Here, the dimensionless Faust-Henry coefficient (C) can be deduced from the intensity ratio of LO and TO phonon peaks from an undoped ZnSe layer [19].

$$\frac{I_{LO}}{I_{TO}} = \left(\frac{\omega_I - \omega_L}{\omega_I - \omega_T}\right)^4 \frac{\omega_T}{\omega_L} \left(1 + \frac{\omega_T^2 - \omega_L^2}{C\omega_T^2}\right)^2. \quad (4)$$

In Eq. (4), ω_I is the incident photon frequency. The Faust-Henry coefficient used in the analysis is $C = -0.21$. The dielectric function with the plasmon damping term (γ) is given by

$$\varepsilon(\omega) = \varepsilon_\infty \left(1 + \frac{\omega_L^2 - \omega_T^2}{\omega_T^2 - \omega^2 - i\omega\Gamma} - \frac{\omega_p^2}{\omega^2 - i\omega\gamma}\right), \quad (5)$$

where ε_∞ is the high-frequency dielectric constant; ω_L (ω_T) are the LO (TO) phonon frequencies of undoped ZnSe; Γ is the phonon damping constant, ω_p is the plasmon frequency,

$$\omega_p^2 = \frac{4\pi n e^2}{\varepsilon_\infty m^*}, \quad (6)$$

where m^* is an electron effective mass. Hence, the free electron density, n , can be estimated using Eq. (6) with lineshape analysis. Table 5.2 gives the fitting parameters, and $\gamma > \omega_p$ is clearly observed, revealing that the plasmon is overdamped. The overdamped plasmon strongly influences the linewidth of the LOPC mode and yields only one observable phononlike mode [13,17].

Table 5.2 presents the carrier concentration obtained from Raman (n_R) measurements at 300 K as a function of ZnCl_2 effusion cell temperature. Figure 5.2 plots the carrier concentrations obtained from the Hall (n_H) and Raman (n_R) measurements. The figure demonstrates that the carrier concentration obtained from the two methods agree closely, revealing that the Raman scattering is an effective and nondestructive approach for determining the free carrier density in n-type ZnSe:Cl layers. The slight deviation between these two experimental results has several causes. Firstly, the GaAs TO phonon near the high-frequency side of the LOPC mode may influence the accuracy of the lineshape fitting. Secondly, the Cl-related impurity mode, which is only clearly identified at high pressure appears at the low frequency side of LOPC and will be discussed later. However, it may slightly affect the lineshape analysis. Finally, $m^* = 0.16 m_0$ and $\epsilon_\infty = 6.1$ [20], were used in Eq. (6) to calculate the free carrier density. Because of the polaron effect [21], it is rather difficult to determine the electron effective mass properly. The possible values of electron concentration and mobility calculated by using different values of effective mass and dielectrics were expressed by the error-bars in Fig. 5.2 and 5.3.

Figure 5.3 compares the mobility obtained from the Hall measurements (μ_H) and the lineshape analysis of Raman spectra (μ_R) using the equation $\mu_R = \frac{e}{m^* \gamma}$. The mobility ratio (μ_H/μ_R) is between 2.0 and 3.4, depending on the electron concentration. Similar experimental results were reported in p-type GaAs with lower mobility. For instance, Fukasawa *et al.* [22], Gargouri *et al.* [23], Mlayah *et al.* [24] and Irmer *et al.* [25] respectively obtained $\mu_H/\mu_R \approx 1.5$ to 2.6, 3.7, 2.0, and 2.3. The difference between μ_H (Hall mobility) and μ_R (optical Raman mobility) is reasonable because the optical Raman mobility is calculated from the plasmon damping due to individual excitation, while the Hall mobility originates from electron scattering with phonons and ionized impurities.

Figure 5.4 (a) shows the up-stroke pressure-dependent Raman spectra of n-type ZnSe:Cl

layer ($8.2 \times 10^{15} \text{ cm}^{-3}$) at room temperature. The applied pressure reduces the lattice constant and the crystal volume, shifting the LOPC and TO phonons to higher frequencies, accompanied with a decrease in intensity. As presented in Fig. 5.4 (a), the TO phonon splits into two peaks at $7.6 \pm 0.3 \text{ GPa}$, and the peaks depend differently on pressure. Investigations of nonmagnetic and magnetic II-VI ternary compounds have shown that pressure-induced TO phonon splitting contributes to the formation of an additional (cinnabar) phase [6,7,10]. Furthermore, a weak feature, which is assigned to a Cl-related impurity mode (*I*), appears at the low-frequency side of the LOPC mode. As the pressure increases, this phonon mode tends to exhibit negative dependence on pressure and becomes more intense. At $3.0 \pm 0.3 \text{ GPa}$, the *I* mode overlaps with the TO phonon. As the pressure increases further, the two modes cross each other. Figure 5.4 (b) plots the Raman-shift versus the pressure of all of the phonon modes, with quadratic polynomial fitting. The LO phonon disappears and the sample becomes opaque at $13.6 \pm 0.2 \text{ GPa}$. These facts are evidence of the semiconductor-to-metal phase transition. The transition pressure, which is almost identical to that of the undoped binary ZnSe crystals [9,10], can be attributed to the lower doping concentration. However, two TO phonon modes and the *I* mode are still observed in the Raman spectra when the semiconductor-to-metal phase transition occurs, because the Cl-related and TO modes are transverse vibration modes and can exist on the surface of metal even if the depth of penetration by the excitation laser beam into the metal is merely several tens of angstroms [6,9].

Figure 5.5 (a) displays the up-stroke pressure-dependent Raman spectra of ZnSe:Cl layer ($1.8 \times 10^{18} \text{ cm}^{-3}$). Figure 5.5 (b) summarizes all of the phonon modes. As can be seen in Fig. 5.5 (a), the Cl-related impurity mode (*I*) is more clearly identified than that of the samples with lower concentration. The mode *I* and the TO phonon are found to overlap at $3.4 \pm 0.3 \text{ GPa}$. Additionally, at $7.6 \pm 0.4 \text{ GPa}$, pressure-induced TO phonon splitting is observed.

However, as the applied pressure is increased to 12.5 ± 0.1 GPa, the LO phonon disappears and the sample becomes opaque. The semiconductor-to-metal phase transition pressure is lower, 12.5 GPa, than that of the sample with the lower concentration ($8.2 \times 10^{15} \text{ cm}^{-3}$), 13.6 GPa, discussed above.

Figure 5.6 plots the phase transition pressure versus the carrier concentration of all studied ZnSe:Cl layers. As the carrier concentration is increased from 8.2×10^{15} to $1.8 \times 10^{18} \text{ cm}^{-3}$, the phase transition pressure falls from 13.6 to 12.5 GPa, indicating that n-type doping tends to reduce the stability of the crystal. The inset in Fig. 5.6 presents the PL spectra of all samples excited by the 325 nm line of a He-Cd laser at room temperature, to understand the source of the decrease in the phase transition pressure as carrier concentration increases. The sharp peak at 2.68 eV is the near band edge (NBE) emission, arising from a Cl_{Se} donor to valence band transition. The broad midgap band in the 1.8 to 2.4 eV range is typically assigned to the donor-to-acceptor pair (DAP) recombination or self-activated (SA) emission [26]. The SA emission is caused by recombination from the intentional shallow donor (Cl_{Se}) to the deep acceptor state (zinc vacancy). The oscillations are interference fringes associated with the thin-film nature of the specimens. As the carrier concentration increases, the SA emission becomes more pronounced: the density of shallow donor (Cl_{Se}) and deep acceptor state (zinc vacancy) pairs increases. Such a crystal defect serves as nucleation sites for the structural phase transition. This result corroborates the work of Pöykkö *et al.* [27], who found that defect complexes that are formed by Cl-impurity atoms and the native defects in ZnSe soften the lattice by producing large distortions. Muratov *et al.* [28] claimed that the zinc vacancies in ZnSe result in large lattice relaxation and alter the overall symmetry of a ZnSe crystal because of the relative shift in the distances of the first and second neighboring atoms from each vacancy. Therefore, the Cl-donor and zinc vacancy pairs in n-type ZnSe:Cl layers are very likely to reduce the crystalline stability and the semiconductor-to-metal phase

transition pressure.

Figure 5.7 plots the dependence of undoped ZnSe LO phonon and ZnSe:Cl ($n_H = 8.2 \times 10^{15} \text{ cm}^{-3}$ and $1.8 \times 10^{18} \text{ cm}^{-3}$) LOPC mode frequencies on pressure, to further elucidate the pressure-dependent LOPC mode of n-type ZnSe:Cl layers. The solid curve shows a quadratic polynomial fit to the undoped ZnSe LO phonon results and the dashed line displays the same fitting curve but shifted downward to capture the assumed behavior of the LOPC mode of ZnSe:Cl ($n_H = 1.8 \times 10^{18} \text{ cm}^{-3}$) under pressure. Apparently, when the applied pressure is less than 2.5 – 3.0 GPa, the behavior of the LOPC mode of ZnSe:Cl ($n_H = 1.8 \times 10^{18} \text{ cm}^{-3}$) follows the dashed curve. However, it deviates and turns to follow undoped behavior as the pressure increases further. Similar results are observed for other samples with different carrier concentration. Moreover, as the carrier density increases, this behavior becomes pronounced. In addition to the blueshift of the LOPC mode, the decline in the FWHM in the LOPC mode when pressure is applied (inset in Fig. 5.7) is also a signature of a decreasing in electron concentration, as discussed in Fig. 5.1. This behavior could also be associated with the pressure-induced weakening of LO-phonon-plasmon coupling that is caused by the fall in electron concentration.

Photoluminescence measurements made by Ritter *et al.* also revealed the degradation of n-type behavior in ZnSe at high pressure [26]. They indicated that applied hydrostatic pressure destabilizes the deep acceptor ground state of the zinc-vacancies-donor complexes and cause a new deep donor-like state (*D*) to enter the band gap of n-type ZnSe, modifying the rate of pressure shift of the SA emission, and degrading the n-type behavior of n-type ZnSe. Ritter *et al.* concluded that the *D* state, which is located at 0.15 – 0.18 eV above the conduction band edge (CBE) at ambient pressure (Fig. 5.8), is very likely to be an excited state of the zinc-vacancies-donor complex. The pressure at which the LOPC mode deviates and turns to follow the undoped LO phonon is identical to the change in pressure of the SA

emission in Ref. 26. Accordingly, the pressure-induced weakening of LO-phonon-plasmon coupling can be interpreted as being related to the emergence of the new deep donor-like state. The D state exhibits a much weaker dependence on pressure than the CBE [26]. Consequently, the energy difference between the D state and the conduction band minimum (at Γ point), ΔE ($E_D - E_C$), varies with the applied pressure. As can be seen in Fig. 5.8, ΔE is positive at ambient pressure. Under compression, ΔE decreases and eventually becomes negative. As ΔE becomes negative at about 2.5 – 3.0 GPa, the D state becomes entirely trapped with the transfer of electrons from the conduction band, degrading the n-type behavior of ZnSe:Cl, and reducing the LO-phonon-plasmon coupling efficiency.

IV. Conclusions

This work studied the vibrational, electronic, and crystalline properties of n-type ZnSe:Cl layers with carrier concentration from $8.2 \times 10^{15} \text{ cm}^{-3}$ to $1.8 \times 10^{18} \text{ cm}^{-3}$ using Raman spectroscopy. The spectra are well-modeled by taking into account the phononlike coupled mode of the electron plasmons and the LO phonon. The Raman scattering efficiency and the dielectric function were calculated for the spectral lineshape fittings. Carrier concentration obtained from the Hall and optical Raman measurements agree well. The semiconductor-to-metal phase transition pressure of n-type ZnSe:Cl layer declines as the carrier concentration increases. As the carrier concentration increases from 8.2×10^{15} to $1.8 \times 10^{18} \text{ cm}^{-3}$, the phase transition pressure falls from 13.6 to 12.5 GPa, suggesting that n-type doping tends to reduce structural stability. Additionally, high-pressure Raman measurements revealed degradation of n-type behavior in ZnSe under compression. This behavior is attributable to the emergence of deep donor-like states.

References

- [1] H. K. Mao and R. J. Hemley, *Science* **244**, 1462 (1989).
- [2] W. L. Mao, H. K. Mao, Y. Meng, P. J. Eng, M. Y. Hu, P. Chow, Y. Q. Cai, J. Shu, and R. J. Hemley, *Science* **314**, 636 (2006).
- [3] P. L. Smith and J. E. Martin, *Phys. Lett.* **19**, 541 (1965).
- [4] G. Itkin, G. R. Hearne, E. Sterer, M. P. Pasternak, and W. Potzel, *Phys. Rev. B* **51**, 3195 (1995).
- [5] S. Ves, K. Strössner, N. E. Christensen, C. K. Kim, and M. Cardona, *Solid State Commun.* **56**, 479 (1985).
- [6] C. M. Lin, D. S. Chuu, T. J. Yang, W. C. Chou, J. Xu, and E. Huang, *Phys. Rev. B* **55**, 13641 (1997).
- [7] C. S. Yang, C. S. Ro, W. C. Chou, C. M. Lin, D. S. Chuu, J. Hu, E. Huang, and J. Xu, *J. Appl. Phys.* **85**, 8092 (1999).
- [8] C. M. Lin, D. S. Chuu, J. Xu, E. Huang, W. C. Chou, J. Z. Hu, and J. H. Pei, *Phys. Rev. B* **58**, 16 (1998).
- [9] Y. C. Lin, C. H. Chiu, W. C. Fan, S. L. Yang, D. S. Chuu, and W. C. Chou, *J. Appl. Phys.* **101**, 073507 (2007).
- [10] C. S. Yang, W. C. Chou, D. M. Chen, C. S. Ro, J. L. Shen, and T. R. Yang, *Phys. Rev. B* **59**, 8128 (1999).
- [11] M. J. Seong, S. H. Chun, H. M. Cheong, N. Samarth, and A. Mascarenhas, *Phys. Rev. B* **66**, 033202 (2002).
- [12] W. Limmer, M. Glunk, S. Mascheck, A. Koeder, D. Klarer, W. Schoch, K. Thonke, R. Sauer, and A. Waag, *Phys. Rev. B* **66**, 205209 (2002).
- [13] G. Abstreiter, M. Cardona, and A. Pinczuck, in *Light Scattering in Solids IV*, edited by M. Cardona and G. Güntherodt (Springer, Berlin, 1984), p. 5, and references therein.

- [14] H. Harima, S. Nakashima, and T. Uemura, *J. Appl. Phys.* **78**, 1996 (1995).
- [15] A. Mooradian and G. B. Wright, *Phys. Rev. Lett.* **16**, 999 (1966).
- [16] T. Kozawa, T. Kachi, H. Kano, Y. Taga, and M. Hashimoto, *J. Appl. Phys.* **75**, 1098 (1994).
- [17] G. Irmer, M. Wenzel, and J. Monecke, *Phys. Rev. B* **56**, 9524 (1997).
- [18] M. V. Klein, B. N. Ganguly, and P. J. Colwell, *Phys. Rev. B* **6**, 2380 (1972).
- [19] W. L. Faust and C. H. Henry, *Phys. Rev. Lett.* **17**, 1265 (1966).
- [20] H. Hartmann, R. Mach, and B. Selle, in *Current Topics in Materials Science*, edited by E. Kaldis (North-Holland, Amsterdam, 1982), Vol. 9, p. 1, and references therein.
- [21] D. M. Larsen, in *Polarons in Ionic Crystals and Polar Semiconductors*, edited by J. T. Devreese (North-Holland, Amsterdam, 1972), Chap. III.
- [22] R. Fukasawa and S. Perkowitz, *Phys. Rev. B* **50**, 14119 (1994).
- [23] M. Gargouri, B. Prevot, and C. Schwab, *J. Appl. Phys.* **62**, 3902 (1987).
- [24] A. Mlayah, R. Carles, G. Landa, E. Bedel, and A. Muñoz-Yagüe, *J. Appl. Phys.* **69**, 4064 (1991).
- [25] G. Irmer, J. Monecke, W. Siegel, G. Kühnel, B. H. Bairamov, and V. V. Toporov, in *Proceedings of the 13th International Conference on Raman Spectroscopy*, edited by W. Kiefer, M. Cardona, G. Schaack, F. W. Schneider, and H. W. Schrötter (Wiley, Chichester, 1992).
- [26] T. M. Ritter, B. A. Weinstein, R. M. Park, and M. C. Tamargo, *Phys. Rev. Lett.* **76**, 964 (1996).
- [27] S. Pöykkö, M. J. Puska, and R. M. Nieminen, *Phys. Rev. B* **57**, 12164 (1998).
- [28] L. Muratov, S. Little, Y. Yang, B. R. Cooper, T. H. Myers, and J. M. Wills, *Phys. Rev. B* **64**, 035206 (2001).

Table 5.1 Hall carrier concentration (n_H) and mobility (μ_H), LOPC mode frequencies, linewidth (FWHM) and peak intensity ratio (I_{LOPC} / I_{TO}) of all studied ZnSe samples with various ZnCl₂ doping temperatures (T_{Cl}).

T_{Cl} (°C)	Hall concentration n_H (cm^{-3})	Hall mobility μ_H ($cm^2/V \cdot s$)	LOPC mode frequency (cm^{-1})	FWHM of LOPC mode (cm^{-1})	Intensity ratio $\left(\frac{I_{LOPC}}{I_{TO}} \right)$
Undoped	–	–	252.2 ^a	10.4 ^a	6.7 ^a
110	8.2×10^{15}	154	251.3	19.8	5.2
120	2.4×10^{17}	141	250.5	24.4	3.0
130	6.8×10^{17}	106	249.2	25.3	1.3
140	1.8×10^{18}	67	248.8	25.6	1.3

^aPhonon frequency, FWHM, and intensity ratio of undoped ZnSe LO phonon.

Table 5.2 Carrier concentration (n_R), mobility (μ_R), and mobility ratios (μ_H / μ_R) obtained by optical Raman measurements. Plasmon frequency (ω_p), plasmon damping constant (γ), and phonon damping constant (Γ) are derived by the calculated lineshape analysis.

T_{Cl} ($^{\circ}C$)	Carrier concentration from Raman n_R (cm^{-3})	Mobility		Fitting parameters		
		from Raman μ_R ($cm^2/V \cdot s$)	Mobility Ratio (μ_H / μ_R)	ω_p (cm^{-1})	γ (cm^{-1})	Γ (cm^{-1})
110	7.3×10^{15}	76	2.0	26	770	23
120	2.1×10^{17}	45	3.1	140	1300	29
130	4.8×10^{17}	32	3.3	210	1800	50
140	7.1×10^{17}	20	3.4	255	2890	53

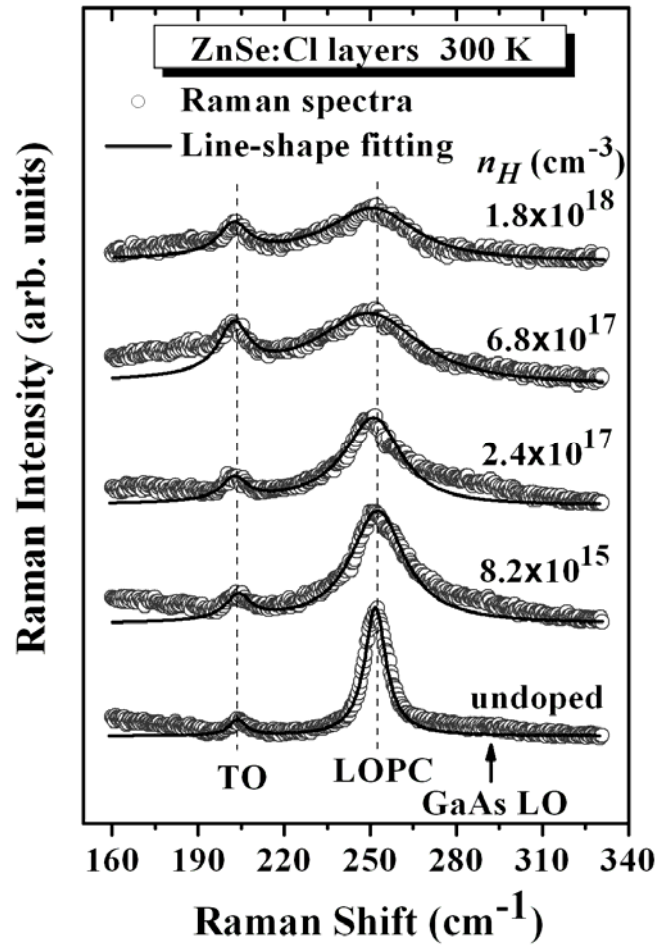


FIG. 5.1. Raman spectra (open circles) with calculated lineshape analysis (solid lines) of n-type ZnSe:Cl layers for various carrier densities at 300 K and ambient pressure, including Lorentzian fit for the TO phonon.

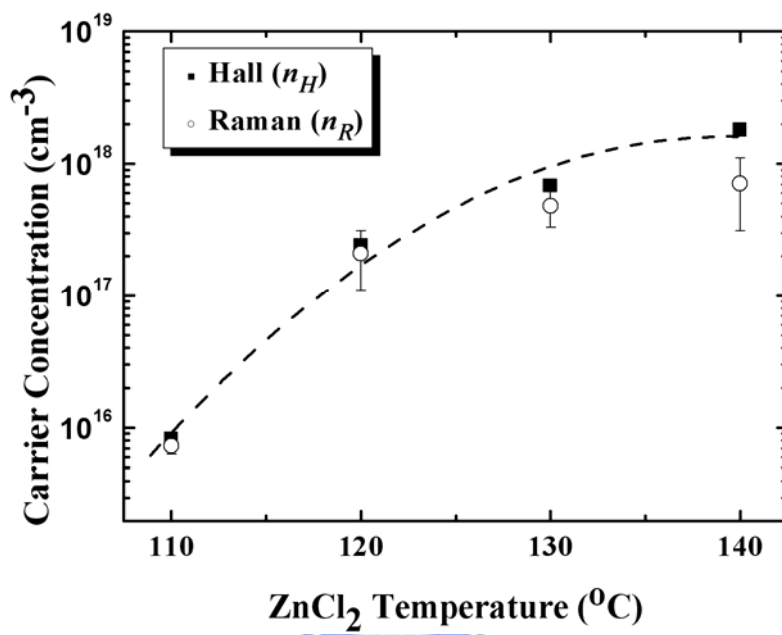


FIG. 5.2. Carrier concentration obtained at 300 K from Hall measurement n_H (full squares), compared with those obtained from optical Raman measurement n_R (open circles), as function of ZnCl₂ source temperature. The dashed line is merely a guide for the eye.

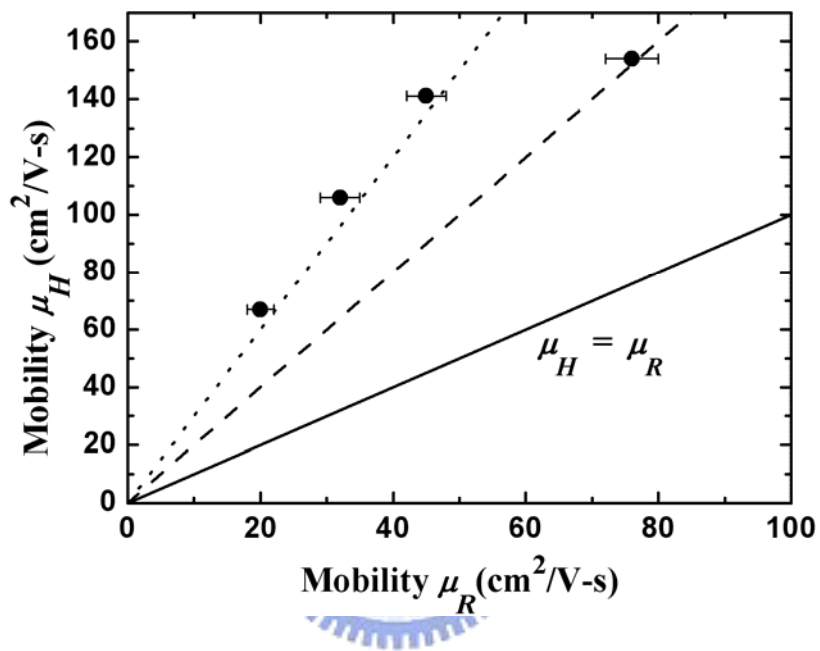


FIG. 5.3. Mobility obtained at 300 K from Hall measurement μ_H versus those obtained from optical Raman measurement μ_R . The solid, dashed, and dotted lines, respectively, represent the ratio, $\mu_H/\mu_R = 1, 2,$ and 3 .

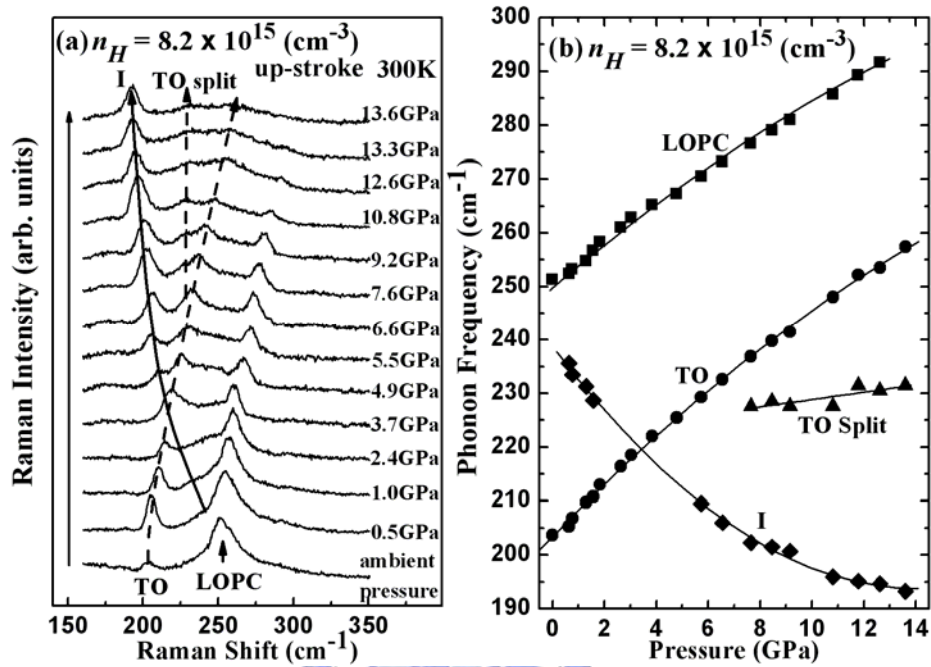


FIG. 5.4. (a) Up-stroke pressure-dependent Raman spectra of the ZnSe:Cl layer ($n_H = 8.2 \times 10^{15} \text{ cm}^{-3}$) at 300 K. The behavior of mode I and the TO phonon are indicated by solid and dashed arrows, respectively. (b) Pressure dependence of Raman shifts for LO, TO, TO split, and mode I of ZnSe:Cl layer ($n_H = 8.2 \times 10^{15} \text{ cm}^{-3}$). The solid curves are quadratic polynomial fits.

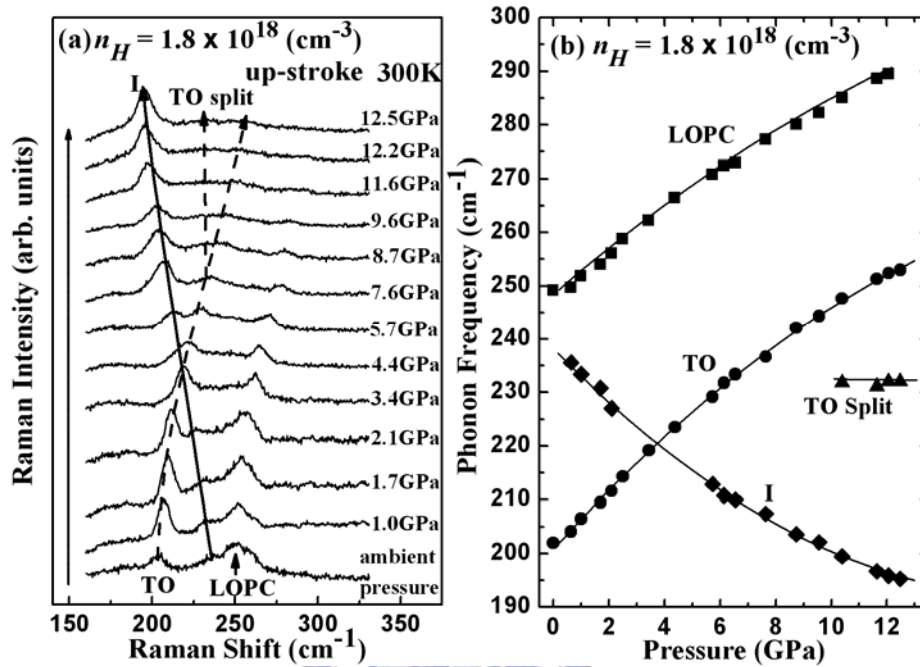


FIG. 5.5. (a) Up-stroke pressure-dependent Raman spectra of the ZnSe:Cl layer ($n_H = 1.8 \times 10^{18} \text{ cm}^{-3}$) at 300 K. The LO phonon disappears at about 12.5 GPa. (b) Pressure-dependent Raman shifts of ZnSe:Cl layer ($n_H = 1.8 \times 10^{18} \text{ cm}^{-3}$). The solid curves represent quadratic polynomial fits.

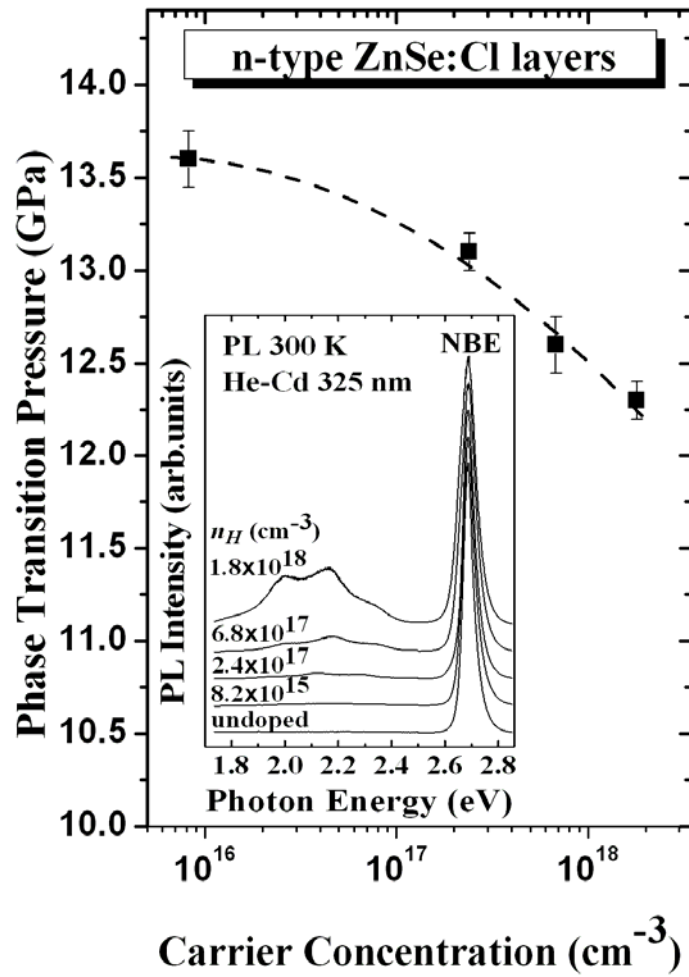


FIG. 5.6. Carrier concentration (n_H)-dependent semiconductor-to-metal phase transition pressure of n-type ZnSe:Cl layers. The dashed curve represents a quadratic polynomial fit. The inset displays the PL spectra of undoped ZnSe and the n-type ZnSe:Cl layers at 300 K, excited by an He-Cd 325 nm laser.

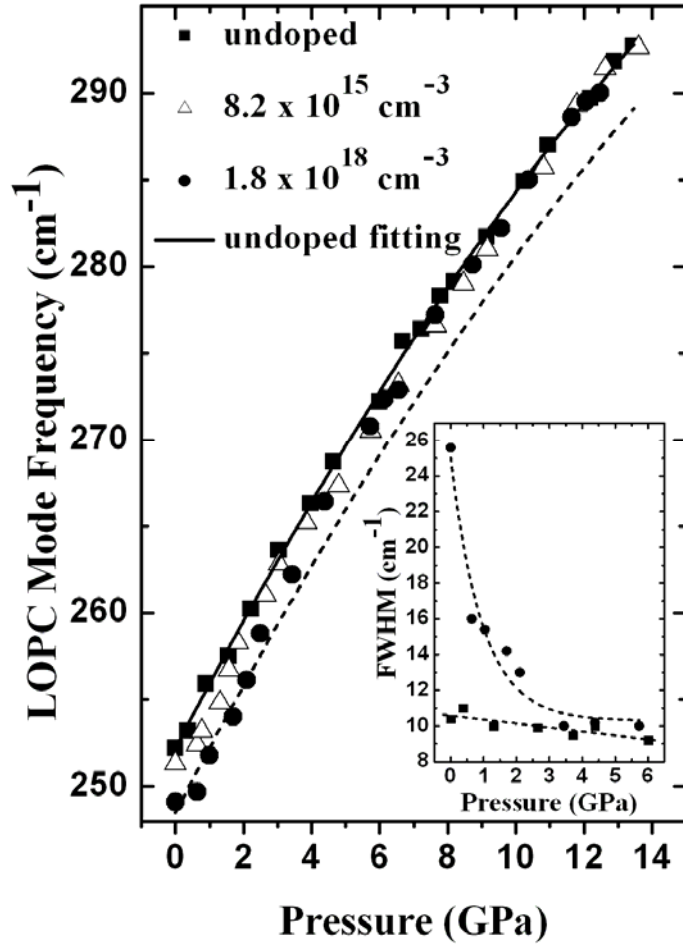


FIG. 5.7. Pressure-dependent LO phonon of undoped ZnSe (full squares) and LOPC mode of n-type ZnSe:Cl for $n_H = 8.2 \times 10^{15} \text{ cm}^{-3}$ (open triangles) and $n_H = 1.8 \times 10^{18} \text{ cm}^{-3}$ (full circles). The solid curve is a quadratic polynomial fit of an undoped ZnSe LO phonon, and the dashed curve is the same curve but shifted downward to capture the presumed behavior of the LOPC mode of ZnSe:Cl ($n_H = 1.8 \times 10^{18} \text{ cm}^{-3}$). The inset plots the pressure-dependent FWHM of the undoped ZnSe LO phonon and the ZnSe:Cl LOPC mode ($n_H = 1.8 \times 10^{18} \text{ cm}^{-3}$).

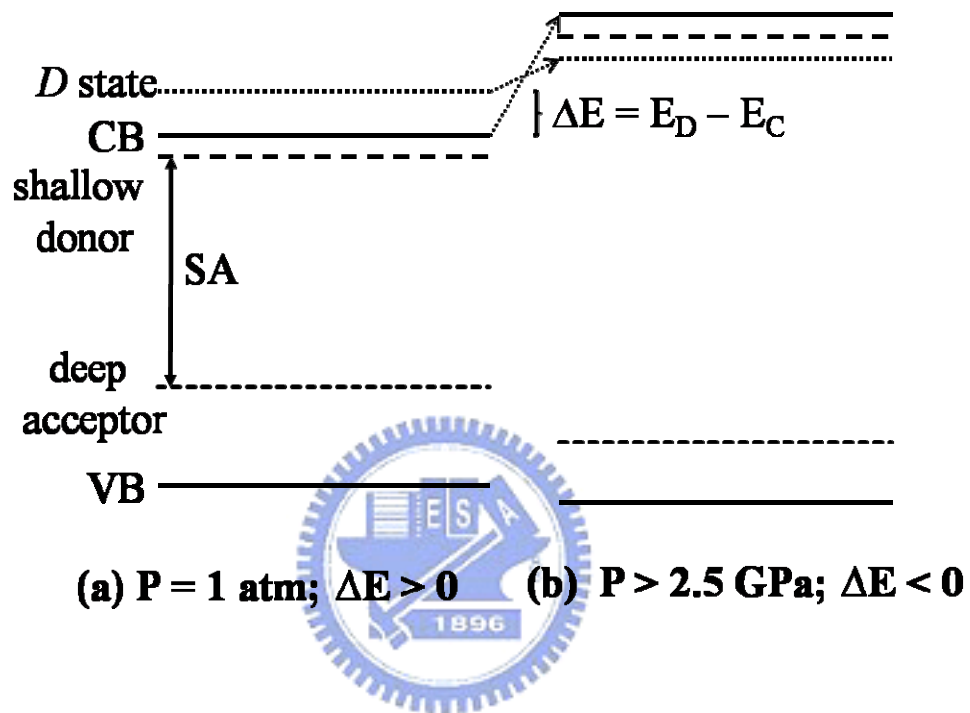


FIG. 5.8. Schematic band structure of n-type ZnSe:Cl. (a) At ambient pressure, the energy difference between the D state and the conduction band minimum, ΔE ($E_D - E_C$), is positive. (b) With compression, ΔE ($E_D - E_C$) declines and eventually becomes negative.

Chapter 6 Time-Resolved Photoluminescence of Isoelectronic Traps in $\text{ZnSe}_{1-x}\text{Te}_x$ Semiconductor Alloys

In this chapter, the Kohlrausch's stretched exponential law is adopted to analyze the photoluminescence (PL) decay profiles of $\text{ZnSe}_{1-x}\text{Te}_x$. As the Te concentration increases, the stretching exponent β initially declines and then monotonically increases. This result can be understood using the hopping-transport and energy transfer model. The increase in the number of isoelectronic Te localized traps can reduce the PL decay rate and increase the linewidth, whereas the hybridization of the Te localized states with the valence-band edge states causes a reduction in both the lifetime and linewidth.



I. Introduction

The unique and interesting physical properties of isoelectronic $\text{ZnSe}_{1-x}\text{Te}_x$ semiconductors have motivated extensive study. These properties include, for example, the unusual spontaneous formation of a superlattice [1], large band-gap bowing [2], and a broad emission linewidth [2,3]. The band anticrossing (BAC) model [4,5] with the Green's function calculation [6,7] was proposed to elucidate the large band-gap bowing and the emission linewidth broadening. Additionally, the transfer of excitons among the Te localized sites in $\text{ZnSe}_{1-x}\text{Te}_x$ with a low Te concentration has also been studied [3]. To investigate further energy transfer behaviors, experiments were performed to determine the photoluminescence (PL) decay time as a function of Te composition. The PL decay profiles are well-fitted by the stretched exponential function, as in the so-called Kohlrausch law [8]. Although the Kohlrausch law closely fits donor-acceptor pair luminescence decay, Kuskovsky *et al.* concluded that it has no fundamental significance [9]. However, Phillips, who reviewed the

decay dynamics of numerous material systems, summarized a few microscopic models based on the Kohlrausch law and concluded that this law is nature's best kept secret [10]. The hopping-transport model has also been proposed to explain the stretched exponential relaxation in complex condensed-matter systems [11]. Therefore, the applicability of the stretched exponential function to the decay dynamics of $\text{ZnSe}_{1-x}\text{Te}_x$ is of interest.

II. Experiment

The samples were grown on (001) GaAs substrates using an EPI 620 molecular beam epitaxy system, and the thicknesses were all fixed at about $0.5 \mu\text{m}$. Samples were all of good crystalline quality since they exhibited intense phonon peaks in both Raman scattering and Fourier transform infrared reflectance spectra [12]. The Te concentration was determined by energy-dispersive X-ray analysis. PL and time-resolved PL (TRPL) was excited by either a 200 fs mode-locked Ti:sapphire laser (400 nm/76 MHz) or a 300 ps pulsed laser diode (405 nm/2.5 MHz). The PL (TRPL) signal was dispersed by a Spex1403 double-grating 0.85 m spectrometer and detected using a (high-speed) photomultiplier tube.

III. Results and Discussion

Figure 6.1 shows the PL spectra of $\text{ZnSe}_{1-x}\text{Te}_x$ ($0 \leq x \leq 1$) measured at 13 K. The sharp near-band-edge emission of $\text{ZnSe}_{1-x}\text{Te}_x$ ($x = 0$) at about 2.80 eV comprises a free exciton (X), a donor-bound exciton (X/D), and an acceptor-bound exciton (X/A). When approximately 0.5 % Se is substituted by Te, the sharp excitonic emission disappears. A broad band, generally attributed to excitons that are bound to isoelectronic Te_{Se} atoms and/or clusters ($\text{X}/\text{Te}_{n \geq 2}$), dominates the spectrum at around 2.65 eV. The emissions in the range from 2.78 to 2.70 eV are assigned to an exciton bound to a Te atom (X/Te) and its phonon replicas [13]. As the Te concentration is further increased, the PL emission shifts to lower energy, from 2.65 eV for x

= 0.005 to 2.13 eV for $x = 0.680$. On the Te-rich side, as the Se content is increased, the PL energies are also red-shifted, from 2.39 eV ($x = 1$) to 2.13 eV ($x = 0.680$). The dependence of the large band-gap bowing on the composition can be explained using the BAC model in which the interaction between the Te (Se) localized states and the ZnSe (ZnTe) valence (conduction) band causes the reduction in the band-gap energy [4,5].

Figure 6.2 presents the TRPL spectra monitored at the peak positions and 13 K. At low temperature, the PL is dominated by the radiative recombination, and the nonradiative recombination could be neglected. Clearly, the following two conclusions can be drawn. (i) The PL lifetime initially increases with the Te content up to 10 %. However, if x is increased, the lifetime monotonically decreases; (ii) None of the TRPL spectra could be fitted by a mono-exponential decay. These experimental profiles indicate complex decay dynamics in $\text{ZnSe}_{1-x}\text{Te}_x$. To make a more quantitative analysis of the decay behavior, as displayed in the inset in Fig. 6.2, the decay curves are fitted by the stretched exponential function [10],

$$I(t) = I_0 \cdot e^{-(t/\tau)^\beta}, \quad (1)$$

where β is the stretching exponent and τ is the exciton lifetime. The gradient of the double natural logarithm versus the natural logarithm, plotted in the inset, yields the stretching exponent β . Sturman *et al.* suggested that the origin of the stretched exponential behavior in complex condensed-matter systems can be well understood using a geometric random site hopping-transport model [11]. The concentrations of both transport and trapping sites determine the value of the variable stretching exponent β . Stretched exponential decay behavior has also been observed in single colloidal semiconductor nanocrystals [14], because of the presence of multi-nonradiative decay channels that surround the single nanocrystal. In this study, the stretched exponential decay is attributed to the presence of Te localized states, which provide multi-decay paths in $\text{ZnSe}_{1-x}\text{Te}_x$.

Figures 6.3(a) – 6.3(c) display the measured full width at half maximum (FWHM), PL

lifetime and stretching exponent β as functions of x . As shown in Fig. 6.3(a), the initial broadening of the linewidth can be attributed to the increase in concentration of Te localized states at several hundreds meV above the ZnSe valence band maximum. The increase in the number of isoelectronic Te traps provides alternate recombination paths for the excitons [11], resulting in an initial increase in the PL lifetime to about 78 ns and a decline in the stretching exponent β , as plotted in Figs. 6.3(b) and 6.3(c), respectively. However, as the Te content is further increased, the FWHM monotonically falls. This result follows from the hybridization of the Te localized states with the valence-band edge states. Wu *et al.* fitted the BAC model to the dependence of the linewidth on composition [6]. The drop in the linewidth is accompanied by decreases in both lifetime and β . The stretching exponent β falls to approximately 0.5 at $x \sim 0.2$, indicating that excitons are still transferred among Te traps.

Based on these observations, the energy transfer model is applied to $\text{ZnSe}_{1-x}\text{Te}_x$. The transfer of excitons from shallow to deep Te localized states explains the initial increase in the PL lifetime, the large linewidth broadening, and the decline in β . As the localized states and the valence band hybridize, the PL lifetime and the linewidth decrease. Wu *et al.* found that, on the Te-rich side, however, the Se localized states lie 2.85 eV above the valence-band edge of ZnTe [6], such that no transfer of excitons among Se localized states could be observed. Accordingly, the decay profiles of $\text{ZnSe}_{1-x}\text{Te}_x$ with high Te concentrations have short lifetimes and decay in a manner that closely approximates mono-exponential decay. Restated, on the Te-rich side, the stretching index β rises and approaches one, as presented in Fig. 6.3(c).

To verify the suggested energy transfer process, the TRPL measurements of $\text{ZnSe}_{0.90}\text{Te}_{0.10}$, were made with an interval of 10 meV and a fixed period of exposure from 2.16 to 2.51 eV. As can be seen in Fig. 6.4(a), the PL decay rate at the high energy side exceeds that at the low energy side. The lifetime (~ 140 ns) at 2.25 eV exceeds that (~ 78 ns)

at 2.37 eV. The ZnSeTe superlattice yielded similar experimental findings [15]. Cheung *et al.* attributed this result to the formation of type-II ZnTe/ZnSe quantum dots (QDs), in which the spatially separated electrons and holes were responsible for the long lifetime. Generally, the band-bending and the electron/hole filling effect in type-II semiconductor systems can induce a large PL peak energy blueshift as the excitation intensity increases [16]. Nevertheless, the samples yielded no obvious PL energy blueshift over a range of excitation intensities of three orders of magnitude. Hence, the long lifetime herein is not associated with the formation of type-II ZnTe/ZnSe QDs, induced by the self-segregation of ZnTe and ZnSe.

The PL peak is red-shifted as the detection time passes. Figure 6.4(b) displays the overall evolution of TRPL results. It is clearly seen that within the first 10 ns after excitation the emission peak is at about 2.40 eV. As time passes, the emission peak dramatically shifts towards the low energy side and is asymmetric, revealing that some of the localized excitons of higher energies are transferred to the deep traps at the low energy side, resulting in a slow decay on the lower energy side. The period of transfer can exceed several tens of nanoseconds. The transfer of excitons among localized states creates an alternative recombination route. Consequently, the decay curves can only be fitted using the stretched exponential function instead of the mono-exponential function.

IV. Conclusions

In summary, the TRPL of isoelectronic $\text{ZnSe}_{1-x}\text{Te}_x$ semiconductors was studied. The decay curves are well-fitted using the Kohlrausch law. As the Te concentration is increased, the stretching exponent β initially declines and then monotonically increases. This result, consistent the increase in PL lifetime and linewidth, shows strong evidence of the transfer of excitons from shallow to deep Te trap states. On the Te-rich side, since the Se localized states lie above the conduction-band edge and the Te localized states hybridize with the

valence-band states, the decay profiles of $\text{ZnSe}_{1-x}\text{Te}_x$ exhibit short lifetimes and an increase in the stretching index β .



References

- [1] S. P. Ahrenkiel, S. H. Xin, P. M. Reimer, J. J. Berry, H. Luo, S. Short, M. Bode, M. Al-Jassim, J. R. Buschert, and J. K. Furdyna, *Phys. Rev. Lett.* **75**, 1586 (1995).
- [2] M. J. S. P. Brasil, R. E. Nahory, F. S. Turco-Sandroff, H. L. Gilchrist, and R. J. Martin, *Appl. Phys. Lett.* **58**, 2509 (1991).
- [3] D. Lee, A. Mysyrowicz, A. V. Nurmikko, and B. J. Fitzpatrick, *Phys. Rev. Lett.* **58**, 1475 (1987).
- [4] W. Walukiewicz, W. Shan, K. M. Yu, J. W. Ager III, E. E. Haller, I. Miotkowski, M. J. Seong, H. Alawadhi, and A. K. Ramdas, *Phys. Rev. Lett.* **85**, 1552 (2000).
- [5] W. Shan, W. Walukiewicz, J. W. Ager III, E. E. Haller, J. F. Geisz, D. J. Friedman, J. M. Olson, and S. R. Kurtz, *Phys. Rev. Lett.* **82**, 1221 (1999).
- [6] J. Wu, W. Walukiewicz, K. M. Yu, J. W. Ager III, E. E. Haller, I. Miotkowski, A. K. Ramdas, Ching-Hua Su, I. K. Sou, R. C. C. Perera, and J. D. Denlinger, *Phys. Rev. B* **67**, 035207 (2003).
- [7] J. Wu, W. Walukiewicz, and E. E. Haller, *Phys. Rev. B* **65**, 233210 (2002).
- [8] R. Kohlrausch, *Ann. Phys. (Leipzig)* **12**, 393 (1847).
- [9] I. Kuskovsky, G. F. Neumark, V. N. Bondarev, and P. V. Pikhitsa, *Phys. Rev. Lett.* **80**, 2413 (1998).
- [10] J. C. Phillips, *Rep. Prog. Phys.* **59**, 1133 (1996).
- [11] B. Sturman, E. Podivilov, and M. Gorkunov, *Phys. Rev. Lett.* **91**, 176602 (2003).
- [12] C. S. Yang, W. C. Chou, D. M. Chen, C. S. Ro, J. L. Shen, and T. R. Yang, *Phys. Rev. B* **59**, 8128 (1999).
- [13] C. S. Yang, D. Y. Hong, C. Y. Lin, W. C. Chou, C. S. Ro, W. Y. Uen, W. H. Lan, and S. L. Tu, *J. Appl. Phys.* **83**, 2555 (1998).
- [14] G. Schlegel, J. Bohnenberger, I. Potapova, and A. Mews, *Phys. Rev. Lett.* **88**, 137401

(2002).

[15] M. C.-K. Cheung, A. N. Cartwright, I. R. Sellers, B. D. McCombe, and I. L. Kuskovsky, Appl. Phys. Lett. **92**, 032106 (2008).

[16] M. C. Kuo, J. S. Hsu, J. L. Shen, K. C. Chiu, W. C. Fan, Y. C. Lin, C. H. Chia, W. C. Chou, M. Yasar, R. Mallory, A. Petrou, and H. Luo, Appl. Phys. Lett. **89**, 263111 (2006).



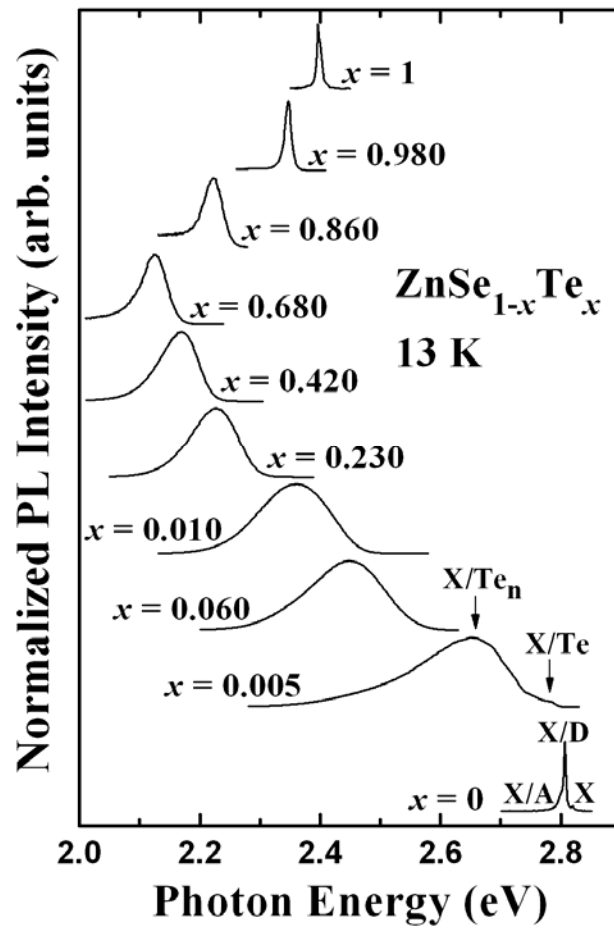


FIG. 6.1. Normalized PL spectra of $\text{ZnSe}_{1-x}\text{Te}_x$ ($0 \leq x \leq 1$) at 13 K.

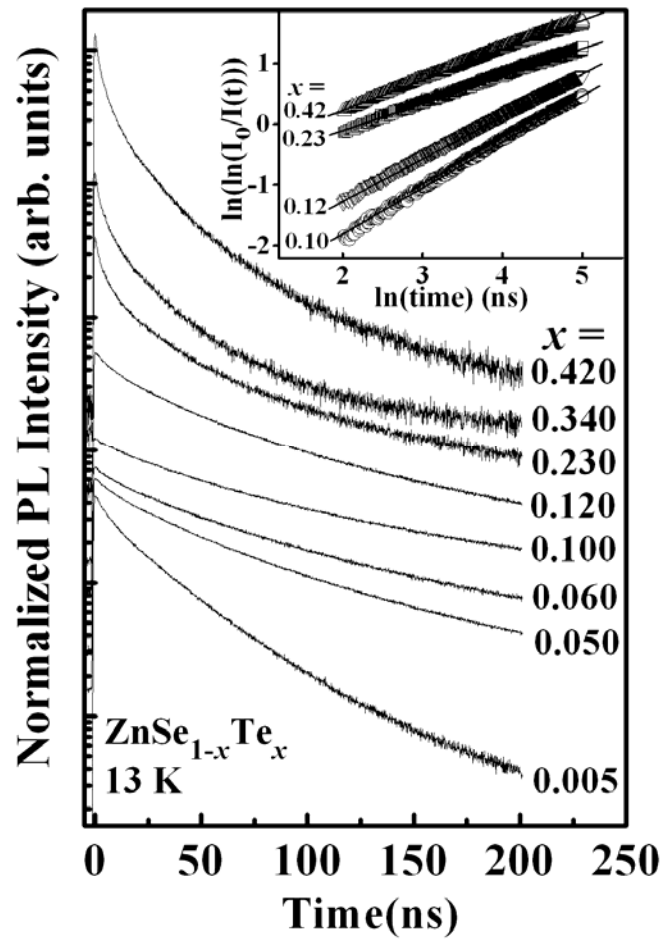


FIG. 6.2. TRPL spectra of ZnSe_{1-x}Te_x at 13 K. The inset plots the data on a double logarithmic scale; the stretched-exponential function is then a straight line.

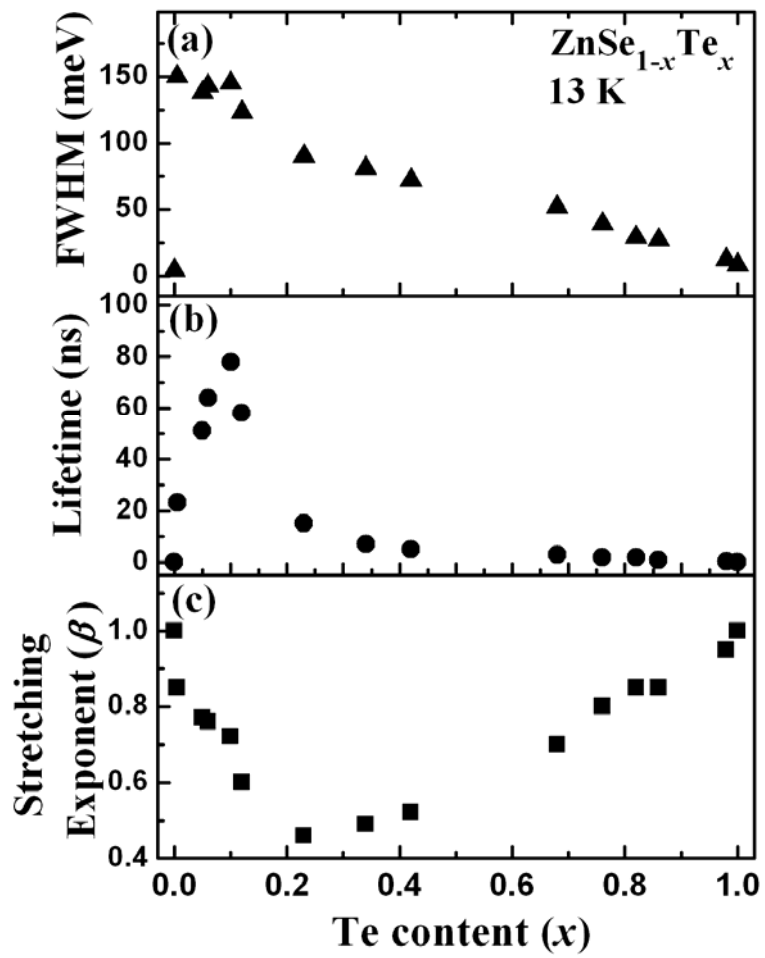


FIG. 6.3. (a) PL lifetime, (b) PL linewidth, and (c) stretching exponent β of $\text{ZnSe}_{1-x}\text{Te}_x$ as functions of Te concentration.

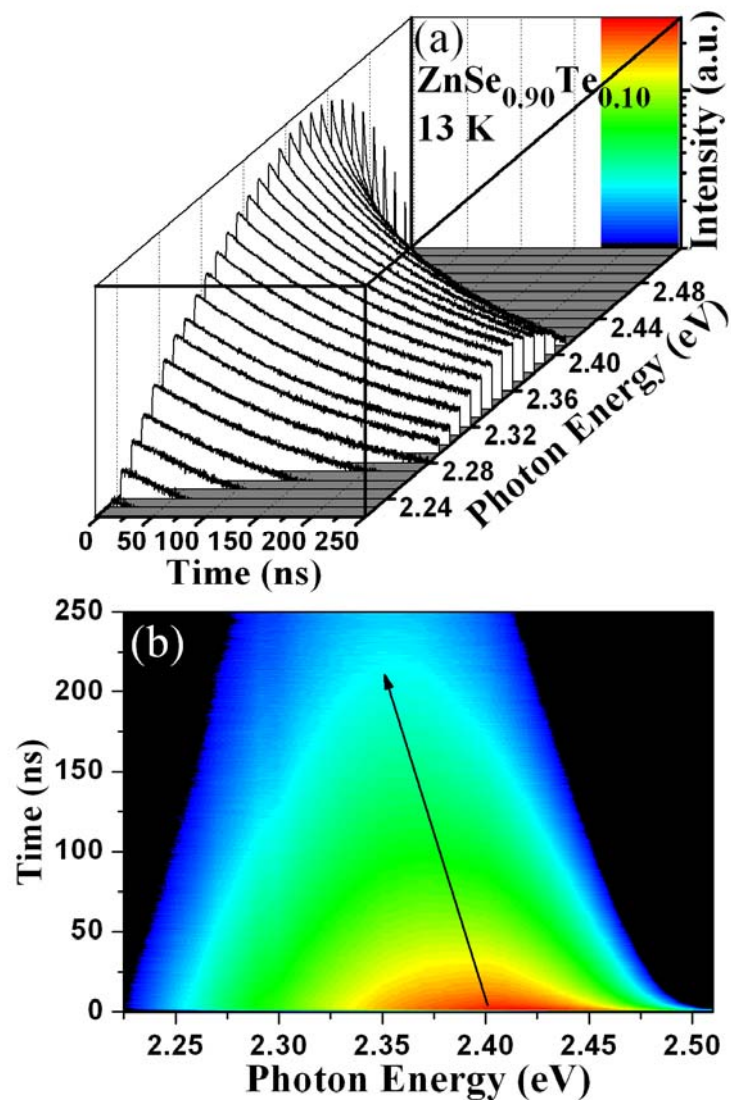


FIG. 6.4. (a) Dependence of TRPL measurements on probing energies of ZnSe_{0.90}Te_{0.10}. (b) TRPL image of ZnSe_{0.90}Te_{0.10}.

Chapter 7 Electronic Energy Transfer in CdTe

Colloidal Quantum Dots

This chapter addresses the transfer of electronic energy between CdTe colloidal quantum dots (QDs) using time-resolved photoluminescence (PL) spectroscopy. The efficiency of energy transfer in QDs depends not only on the spectral overlap of small dots emission and large dots absorption, but also on the inter-dot distances. The quenching of the PL intensity (lifetime) of small dots, as well as an enhancement of large dots in mixed solution and a solid film are evidence of a resonant transfer of energy due to dipolar coupling between proximal QDs. In a solid with mixed QDs, the stretching exponent β increases as the probe-energy declines, and approaches one, implying efficient energy transfer from smaller to larger QDs.




I. Introduction

As a nonradiative process, Förster resonant energy transfer (FRET) is driven by dipole-dipole coupling and transports excitation energy between semiconductor quantum dots (QDs) [1-3]. The efficiency of FRET depends on the degree of spectral overlap between the emission spectrum of the small QDs (donor) and the absorption spectrum of the large QDs (acceptor), and on the sixth power of the separation between the donor and the acceptor [1-3]. Bawendi's group [4,5] was the first to demonstrate the FRET process between close-packed CdSe QDs. Crooker *et al.* elucidated FRET dynamics in monodispersed, mixed-size and layered assemblies of CdSe/ZnS QDs using time-resolved and spectrally-resolved PL [6]. They identified an enhancement in the luminescence and lifetime of large QDs, accompanied by a reduction in those of small QDs. These phenomena are direct evidence of the transfer of energy from small to large QDs. Recently, Franzl *et al.* investigated cascaded energy transfer

in a funnel-like structure [7] and observed a very efficient energy transfer process in layer-by-layer assemblies of oppositely charged CdTe QDs without any linkers between them [8]. Komarala *et al.* demonstrated a surface plasmon-enhanced energy transfer process between CdTe QDs that are close to gold nanoparticles [9].

Improved spectral overlap of emission from small dots and absorption by large dots, and reduced inter-dot distances between small and large QDs can improve the efficiency of energy transfer between QDs. This work explores the electronic energy transfer in CdTe QDs as a function of concentration of QDs. Moreover, a mixture of CdTe QDs in water and in a solid film was studied using photoluminescence (PL) and time-resolved PL (TRPL). Observations demonstrated that the mixed solid film with short inter-dot distance provides efficient dipolar coupling and electronic energy transfer.

II. Experiment



CdTe QDs with diameters of 2.3 nm ($\sim 1.2 \times 10^{-4} \text{ mol} \cdot \text{L}^{-1}$) and 3.4 nm ($\sim 2.2 \times 10^{-5} \text{ mol} \cdot \text{L}^{-1}$) were synthesized directly in water using mercaptopropionic acid (MPA) as a stabilizer [10]. The water-soluble CdTe QDs with diameters of 3.3, 3.7, and 4.0 nm were purchased from PlasmaChem. The QD concentration and diameter were calculated from the extinction spectra, as described elsewhere [10]. The room-temperature absorption spectra were recorded in air using a Cary 50 spectrometer (Varian). PL and TRPL were excited by a 300 ps pulsed laser diode (405 nm/2.5 MHz) at room temperature, and signals were dispersed using a Spex1403 double-grating 0.85 m spectrometer and detected using a (high-speed) photomultiplier tube. The decay traces were recorded using the time-correlated single photon counting approach (Time-Harp, PicoQuant). The overall temporal resolution was about 0.4 ns.

III. Results and Discussion

Figure 7.1(a) presents the PL spectra of 3.3 nm CdTe QDs in water at various concentrations, which ranged from 1 to 1.0×10^{-4} mol \cdot L $^{-1}$. Clearly, the emission peaks were redshifted and the asymmetrical linewidth became narrower as the concentration of the QDs increased. Similar experimental results were observed from 3.7 and 4.0 nm CdTe QDs. Figure 7.1(b) plots the PL peak energy against concentration. The energy shift over the entire concentration range is about 35 meV. The magnitude of the energy shift depends on the homogeneity of QDs and not on their size. According to Fig. 7.1(b), a marked change in the gradient of the energy redshift against concentration occurs at approximately 1.0×10^{-1} mol \cdot L $^{-1}$. The above phenomena can be understood by considering the electronic energy transfer process, which quenches the emission from small dots, and the enhancement of emission from the large dots. The rapid redshift at high concentration occurs because the distance between the QDs dramatically falls as the density of the solution increases, promoting energy transfer. Kagan *et al.* and Crooker *et al.* made similar experimental findings using CdSe QDs [5,6]. To confirm the energy transfer process, TRPL measurements were made. Figure 7.1(c) displays the dynamic evolution of the PL spectra for CdTe QDs (3.3 nm, 1.0×10^{-1} mol \cdot L $^{-1}$). Initially, the peak energy is at 2.20 eV; as time passes, it shifts to the red. Beyond 150 ns, the PL energy remains constant at about 2.18 eV, suggesting that the energy transfer process ceases and the probability of further transfer is suppressed.

This study also investigated the dynamics of electronic energy transfer between QDs by fabricating a mixed system of 50 % 2.3 nm (small) and 50 % 3.4 nm (large) CdTe QDs. In the mixed system, the small and large QDs acted as the donors and acceptors, respectively. Figure 7.2(a) and 7.2(b) present the room-temperature absorption and PL spectra of pure small (D) and pure large (A) QDs in water, indicating sufficient spectral overlap between the emission spectrum of donors and the absorption spectrum of acceptors, and a minor overlap between

their emission spectra. Figure 7.2(b) displays the PL spectrum of the mixed solution. The mixture exhibits an increase in the ratio of the PL intensities of the large to small QDs, which is attributable to the electronic energy transfer from the small to large QDs. The spectral overlap of two distinct QDs was excluded since it would reduce the intensity ratio. To verify the suggestion, Fig. 7.3(a) presents the TRPL spectra of pure donors and a mixture in solution monitored at peak (537 nm) energy. The decay rate of the mixture obviously increases over that of pure donors. However, in Fig. 7.3(b), the decay rate of the mixture recorded at the peak (618 nm) decreases, as compared with pure acceptors. The pronounced increase in donor decay rate and decrease in acceptor decay rate of the mixture can be observed by monitoring the blue (red) side of the donor (acceptor) emission, eliminating the PL crosstalk associated with spectral overlap. The multi-exponential PL decay for CdTe QDs results from a dispersion in trap energy levels, which originate from Te surface atoms [10,11].

To measure more quantitatively the decay dynamics, the decay curves are analyzed using Kohlrausch's stretched exponential law [12].

$$I(t) = I_0 \cdot e^{-(t/\tau)^\beta}, \quad (1)$$

where β is the stretching exponent and τ is the exciton lifetime. The τ and β of the mixture, as obtained at 537 nm, fall from 19 to 16 ns and from 0.75 to 0.72, respectively, as compared with pure donors. Conversely, τ and β of the mixture, recorded at 618 nm, increase from 20 to 23 ns and from 0.72 to 0.77, respectively, as compared with pure acceptors. The decrease in PL lifetime and the intensity of the small QDs and the increase in those of the large QDs are direct evidence of electronic energy transfer from the small to the large QDs, eliminating the reabsorption effect, which would not increase the decay rate from small QDs [3,6]. Furthermore, the decrease in the β of donors and the increase in the β in acceptors reflect the transfer of excitons from donors to acceptors, enhancing the emission intensity of the acceptors and reducing the probability of nonradiative trapping.

Reducing the inter-dot separation would increase the efficiency of energy transfer between small and large QDs. Figure 7.2(c) presents the PL spectra of close-packed pure donors, pure acceptors, and mixed solid films. The PL peak energy of solids is redshifted from that of the mixture in solution [Fig. 7.2(b)] because of electronic energy transfer presented in Fig. 7.1. Additionally, a substantial increase in the PL intensity ratio of large to small QDs in the mixed solid over that in mixed solution is observed, revealing an efficient electronic energy transfer. To verify the proposed energy transfer process, the time-resolved and spectrally-resolved PL of mixed solid were obtained with an interval of 10 meV and a fixed period of exposure from 2.53 eV (490 nm) to 1.85 eV (670 nm). As shown in Fig. 7.4(a), the PL decay rate at the high energy side exceeds that at the low energy side. The lifetime at 2.27 eV (546 nm) of small dots is about 8 ns, which increases steadily with the dot size, reaching 27 ns at 1.95 eV (636 nm). The decay curves of the double natural logarithm versus the natural logarithm of PL, plotted in the inset of Fig. 7.4(b), yield the stretching exponent β . A sharp increase in β from 0.57 (at 2.27 eV) to 0.93 (at 1.95 eV) is observed, reflecting efficient energy transfer from small to large QDs as well as a huge suppression of nonradiative recombination. Figure 7.4(b) plots the overall evolution of the TRPL results. Initially after excitation, the emission peak of the acceptors is at approximately 610 nm. As time passes, the emission intensity of donors falls sharply and the emission from acceptors dominates the entire spectrum. Moreover, the emission peak of acceptors shifts dramatically towards the low energy side. Beyond 10 ns, the emission peak is roughly constant at 632 nm, revealing the suppression of further energy transfer. These experimental results are strong evidence of electronic energy transfer, which results from a dramatic decline in the inter-dot distance of the solid mixture.

Figure 7.5 shows true-color images of the pure small, pure large and mixed samples in water and solid films, excited by a 405 nm laser. The color directly reflects the spectral

changes in each sample. The images of pure small (large) QDs in both solution and solid films appear green (red). Energy transfer is responsible for the slight difference between the colors of the images of QDs in solution and those in the solid. The image of the mixed QDs in the solid is almost the same color (red) as that of the pure large QDs in the solid, but the image of the mixed QDs in solution is yellow or orange (a color between green and red), reflecting limited energy transfer. The above observations demonstrate that the electronic energy transfer efficiency of the mixed CdTe QDs in solid films exceeds that of the QDs in solution.

IV. Conclusions

In summary, this work elucidated the electronic energy transfer between CdTe QDs using time-resolved PL. As the concentration of CdTe QDs increases, a redshift in the PL peak energy is accompanied by a decrease in linewidth, because of the energy transfer from small to large QDs. The mixed CdTe QDs solid exhibits more efficient energy transfer than that in solution, because the inter-dot distance drastically declines as the mixture is dispersed in solid film. Additionally, a significant enhancement in PL intensity as well as in the stretching exponent β for large dots in mixed QDs reveals the suppression of nonradiative recombination.

References

- [1] T. Förster, in *Comparative Effects of Radiation*, edited by M. Burton, J. S. Kirby-Smith, and J. L. Magee (Wiley, New York, 1960), p. 301.
- [2] D. L. Andrews and A. A. Demidov, *Resonance Energy Transfer*, (Wiley, Chichester, U.K., 1999).
- [3] B. Valeur, *Molecular Fluorescence: Principles and Applications*, (Wiley, New York, 2002).
- [4] C. R. Kagan, C. B. Murray, M. Nirmal, and M. G. Bawendi, *Phys. Rev. Lett.* **76**, 1517 (1996).
- [5] C. R. Kagan, C. B. Murray, and M. G. Bawendi, *Phys. Rev. B* **54**, 8633 (1996).
- [6] S. A. Crooker, J. A. Hollingsworth, S. Tretiak, and V. I. Klimov, *Phys. Rev. Lett.* **89**, 186802 (2002).
- [7] T. Franzl, S. Schietinger, A. L. Rogach, and J. Feldmann, *Nano Lett.* **4**, 1599 (2004).
- [8] T. Franzl, A. Shavel, A. L. Rogach, N. Gaponik, T. A. Klar, A. Eychmüller, and J. Feldmann, *Small* **1**, 392 (2005).
- [9] V. K. Komarala, A. L. Bradley, Y. P. Rakovich, S. J. Byrne, Y. K. Gun'ko, and A. L. Rogach, *Appl. Phys. Lett.* **93**, 123102 (2008).
- [10] A. L. Rogach, T. Franzl, T. A. Klar, J. Feldmann, N. Gaponik, V. Lesnyak, A. Shavel, A. Eychmüller, Y. P. Rakovich, and J. F. Donegan, *J. Phys. Chem. C* **111**, 14682 (2007).
- [11] G. Schlegel, J. Bohnenberger, I. Potapova, and A. Mews, *Phys. Rev. Lett.* **88**, 137401 (2002).
- [12] Y. C. Lin, W. C. Chou, W. C. Fan, J. T. Ku, F. K. Ke, W. J. Wang, S. L. Yang, W. K. Chen, W. H. Chang, and C. H. Chia, *Appl. Phys. Lett.* **93**, 241909 (2008).

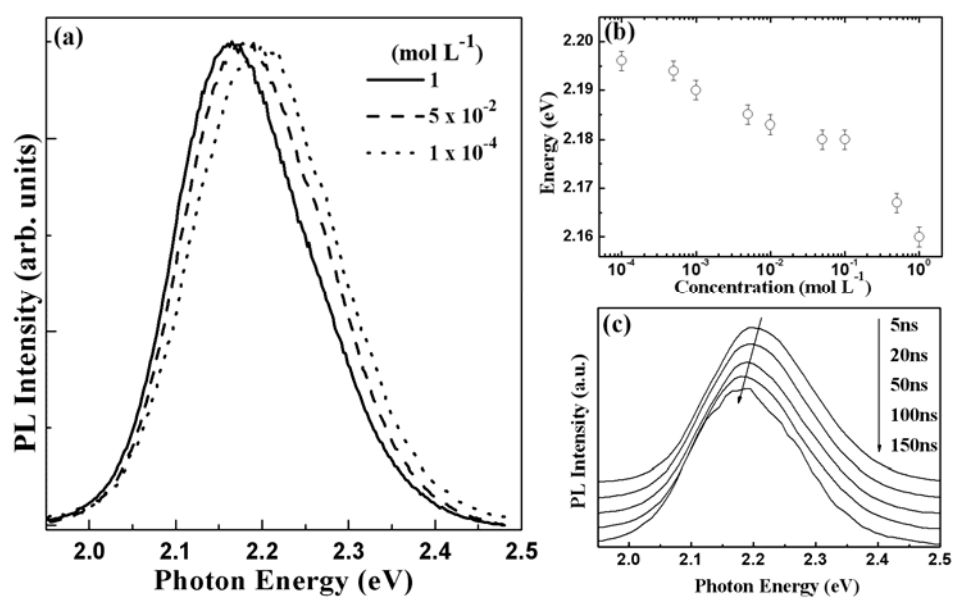


FIG. 7.1. (a) PL spectra of 3.3 nm CdTe QDs in water at various concentrations - 1 mol · L⁻¹ (solid), 5.0 × 10⁻² mol · L⁻¹ (dashed), and 1.0 × 10⁻⁴ mol · L⁻¹ (dotted). (b) PL peak intensity versus concentration of QDs. (c) Temporal evolution of PL spectra of QDs (1.0 × 10⁻¹ mol · L⁻¹).

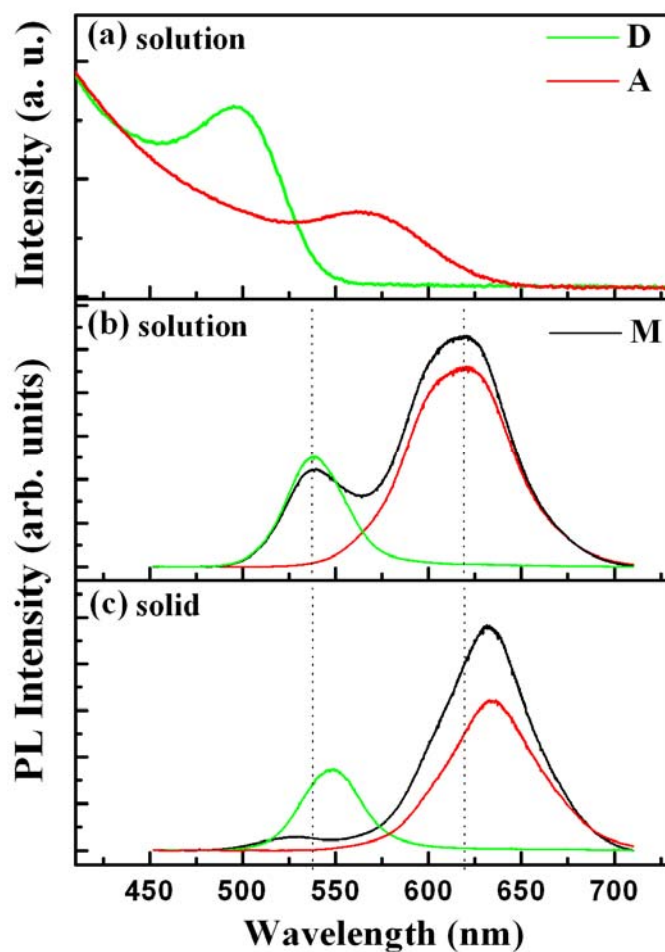


FIG. 7.2. (a) Absorption spectra of pure small (donor) and pure large (acceptor) CdTe QDs in water. PL spectra of pure donors (D), pure acceptors (A), and mixed (M) CdTe QDs (b) in water, and (c) solid.

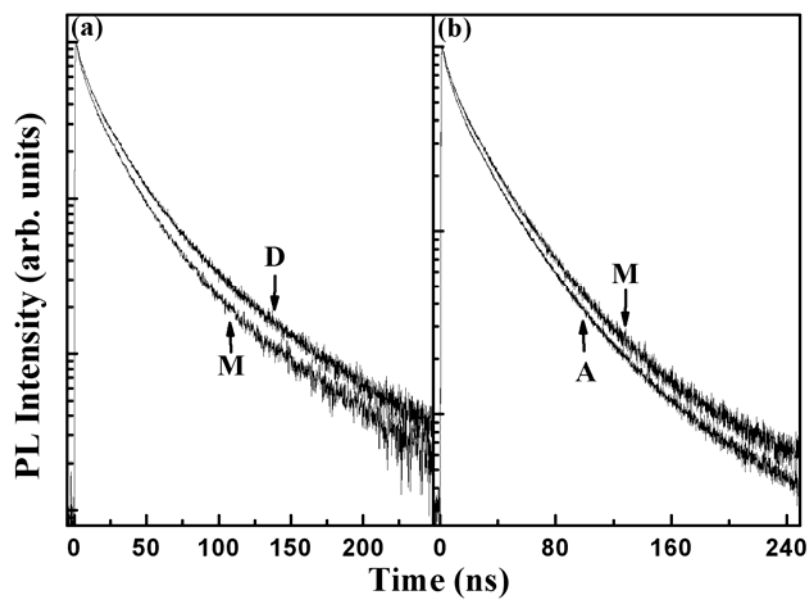


FIG. 7.3. TRPL spectra of (a) donors in pure and mixed solution probed at 537 nm, and (b) acceptors in pure and mixed solution probed at 618 nm.

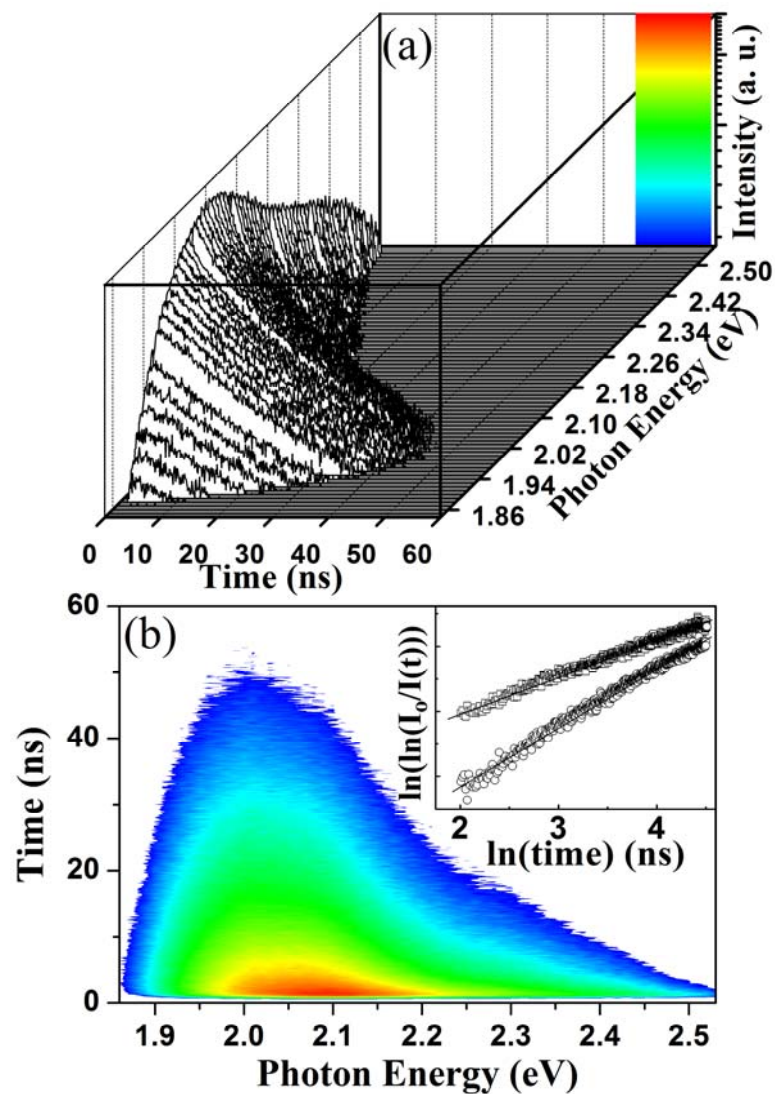


FIG. 7.4. (a) Dependence of TRPL measurements on probing energies of mixed CdTe QDs solid. (b) Time-resolved PL image of mixed CdTe QDs solid. Inset plots the TRPL data obtained at 2.27 eV (open squares) and 1.95 eV (open circles) on a double logarithmic scale.

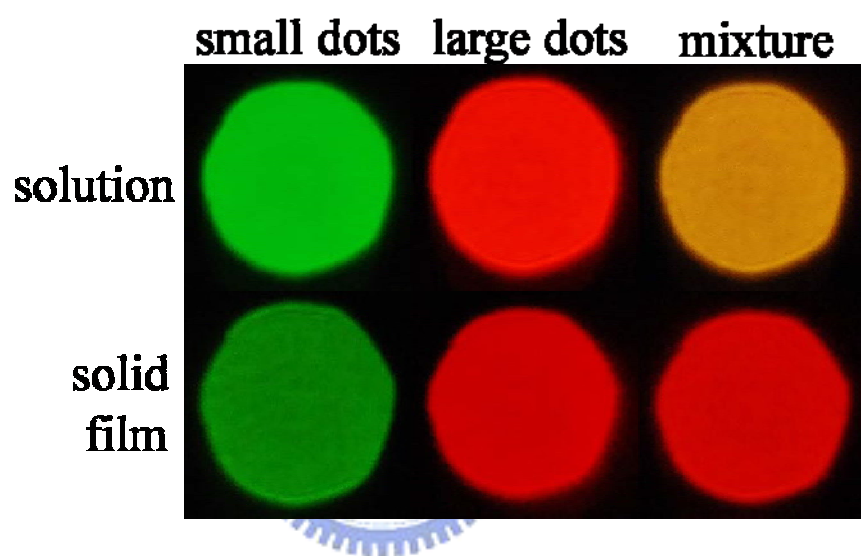


FIG. 7.5. True-color images of pure small, pure large and mixed QDs in solution and solid.

Chapter 8 Conclusions

This thesis studied the pressure-dependent physical properties of ZnCdSe, ZnMnTe and n-type ZnSe:Cl thin films and CdTe colloidal QDs. The decay dynamics of isoelectronic traps in ZnSeTe semiconductors were also discussed. Raman scattering and PL experiments were performed to investigate the high-pressure behavior of $\text{Zn}_{1-x}\text{Cd}_x\text{Se}$. Low-temperature Raman measurements indicate that ZnCdSe exhibits an intermediate phonon mode. The pressure-driven RRS effect was observed in samples with a high Cd concentration ($x \geq 0.18$). Both the Stokes and anti-Stokes sides of the LO phonons disappear as the crystal phase changes from the semiconductor to the metal. The pressure at the onset of the semiconductor-to-metal phase transition declined as the Cd content increased.

To examine the vibrational and crystalline characteristics of $\text{Zn}_{1-x}\text{Mn}_x\text{Te}$, the RRS effect was induced under external pressure. The disappearance of the LO phonon, which accompanies a semiconductor-to-metal phase transition in ZnTe occurs at about 15.7 ± 0.2 GPa. As the Mn content increases from 0 to 0.26, the metallic phase transition pressure falls from 15.7 to 10.3 GPa. Based on the pressure-dependent LO and TO phonon frequencies and Grüneisen parameters (γ_i), an application of external pressure reduces the iconicity of the $\text{Zn}_{1-x}\text{Mn}_x\text{Te}$ compound semiconductors.

The vibrational, electronic, and crystalline properties of n-type ZnSe:Cl layers were also studied. The spectra are well-modeled by taking into account the phononlike coupled mode of the electron plasmons and the LO phonon. The Raman scattering efficiency and the dielectric function were calculated for the spectral lineshape fittings. The carrier concentrations obtained from the Hall and optical Raman measurements are mutually consistent. As the carrier concentration increases from 8.2×10^{15} to $1.8 \times 10^{18} \text{ cm}^{-3}$, the metallic phase transition

pressure declines from 13.6 to 12.5 GPa, suggesting that n-type doping tends to reduce structural stability. Moreover, high-pressure Raman measurements revealed the degradation of n-type behavior in ZnSe under compression, which is attributable to the emergence of deep donor-like states.

The decay dynamics of isoelectronic $\text{ZnSe}_{1-x}\text{Te}_x$ semiconductors were studied using time-resolved photoluminescence. The Kohlrausch law closely fits the decay curves. As the Te concentration is increased, the stretching exponent β initially decreases and then monotonically increases. This result, consistent with the increase in PL lifetime and linewidth, represents strong evidence of the transfer of excitons from shallow to deep Te trap states. On the Te-rich side, since the Se localized states lie above the conduction-band edge and the Te localized states hybridize with the valence-band states, the decay profiles of $\text{ZnSe}_{1-x}\text{Te}_x$ exhibit short lifetimes and an increase in the stretching index β .

Finally, the electronic energy transfer between CdTe QDs was elucidated using time-resolved PL. As the concentration of CdTe QDs increases, a redshift in the PL peak energy is accompanied by a decrease in linewidth, because of the energy transfer from small to large QDs. The mixed CdTe QDs solid exhibits more efficient energy transfer than that in solution, because the inter-dot distance drastically declines as the mixture is dispersed in solid film. Additionally, a significant enhancement in PL intensity as well as in the stretching exponent β for large dots in mixed QDs reveals the suppression of nonradiative recombination.

Publication Lists

1. J. T. Ku, M. C. Kuo, J. L. Shen, K. C. Chiu, T. H. Yang, G. L. Luo, C. Y. Chang, **Y. C. Lin**, C. B. Fu, D. S. Chuu, C. H. Chia, and W. C. Chou, “Optical characterization of ZnSe epilayers and ZnCdSe/ZnSe quantum wells grown on Ge/Ge_{0.95}Si_{0.05}/Ge_{0.9}Si_{0.1}/Si virtual substrate”, *J. Appl. Phys.* **99**, 063506 (2006).
2. Y. J. Lai, **Y. C. Lin**, C. B. Fu, C. S. Yang, C. H. Chia, D. S. Chuu, W. K. Chen, M. C. Lee, W. C. Chou, M. C. Kuo, and J. S. Wang, “Growth mode transfer of self-assembled CdSe quantum dots grown by molecular beam epitaxy”, *J. Cryst. Grow.* **282**, 338 (2006).
3. M. C. Kuo, J. S. Hsu, J. L. Shen, K. C. Chiu, W. C. Fan, **Y. C. Lin**, C. H. Chia, W. C. Chou, M. Yasar, R. Mallory, A. Petrou, and H. Luo, “Photoluminescence studies of type-II diluted magnetic semiconductor ZnMnTe/ZnSe quantum dots”, *Appl. Phys. Lett.* **89**, 263111 (2006).
4. C. T. Yuan, **Y. C. Lin**, Y. N. Chen, Q. L. Chiu, W. C. Chou, D. S. Chuu, W. H. Chang, H. S. Lin, R. C. Ruaan, and C. M. Lin, “Studies on the electronic and vibrational states of colloidal CdSe/ZnS quantum dots under high pressures”, *Nanotechnology* **18**, 185402 (2007).
5. **Y. C. Lin**, C. H. Chiu, W. C. Fan, S. L. Yang, D. S. Chuu, and W. C. Chou, “Pressure-dependent Raman scattering and photoluminescence of Zn_{1-x}Cd_xSe epilayers”, *J. Appl. Phys.* **101**, 073507 (2007).
6. **Y. C. Lin**, C. H. Chiu, W. C. Fan, C. H. Chia, S. L. Yang, D. S. Chuu, M. C. Lee, W. K. Chen, W. H. Chang, and W. C. Chou, “Raman scattering of longitudinal optical phonon-plasmon coupling in Cl-doped ZnSe under high pressure”, *J. Appl. Phys.* **102**, 123510 (2007).
7. **Y. C. Lin**, W. C. Fan, C. H. Chiu, F. K. Ke, S. L. Yang, D. S. Chuu, M. C. Lee, W. K. Chen, W. H. Chang, W. C. Chou, J. S. Hsu, and J. L. Shen, “Pressure-induced metallization and resonant Raman scattering in Zn_{1-x}Mn_xTe”, *J. Appl. Phys.* **104**, 013503 (2008).
8. **Y. C. Lin**, W. C. Chou, W. C. Fan, J. T. Ku, F. K. Ke, W. J. Wang, S. L. Yang, W. K. Chen, W. H. Chang, and C. H. Chia, “Time-resolved photoluminescence of isoelectronic traps in ZnSe_{1-x}Te_x semiconductor alloys”, *Appl. Phys. Lett.* **93**, 241909 (2008).